Nanoscale Investigations of Biomaterials using Atomic Force Microscopy and Enhanced Raman Spectroscopy

Dissertation

zur Erlangung des akademischen Grades

doctor rerum naturalium

(Dr. rer. nat.)

FRIEDRICH-SCHILLER-
UNIVERSITÄT
JENA

vorgelegt dem Rat der Chemisch-Geowissenschaftlichen Fakultät der

Friedrich-Schiller-Universität Jena

von

Xiaobin YAO, M. Sc

geboren am 03.02.1988 in Fujian, China

Gutachter:

1. Prof. Dr. Volker Deckert, Nanospectroscopy, Institute of Physical Chemstiry, Friedrich Schiller University Jena
2. apl. Prof. Dr. Wolfgang Fritzsche, Nanobiophotonics, Leibniz Institute of Photonic Technology

Tag der Verteidigung: 27.10.2021

This work is dedicated to

my wife Tingfang LIU and my daughter Aixi YAO.

I thank them very much for their support during my thesis.

Table of Contents

Table of Contents IV
Abbreviations VII
List of Figures IX
List of Tables XII
Motivation and Abstract 1
1. Introduction 4
1.1 Super-resolution techniques 4
1.1.1 Beyond Abbe diffraction limit 4
1.1.2 Super-resolution optical techniques 5
1.1.3 Super-resolution non-optical techniques 7
1.2 Atomic force microscopy 8
1.3 Nanoscale-resolution Raman spectroscopy 10
1.3.1 Raman scattering 10
1.3.2 SERS spectroscopy 12
1.3.3 TERS spectroscopy 14
1.4 Nanoscale investigations of CaL and SARS-CoV-2 using AFM and enhanced Raman spectroscopy 16
2. Materials and instruments 18
2.1 Materials 18
2.2 Instruments 19
3. A simple method to suppress sample degradation in SERS spectroscopy 20
3.1 Experiments 20
3.2 Ag SERS substrates 22
3.3 Cr-supported Ag SERS substrates for liquid measurements 26
3.4 Iodide suppresses degradation of peptides in SERS measurements 28
3.4.1 Sample degradation in SERS measurements 28

3.4.2 Photocatalysis-induced sample degradation on Ag SERS substrates 29
3.4.3 Iodide suppresses sample degradation 32
3.5 SERS measurements with high reproducibilites 37
3.6 Chapter summary 39
4. Investigations of Candidalysin using time-lapse AFM and TERS spectroscopy 41
4.1 Candidalysin 41
4.2 Experiments 42
4.3 CaL-induced structural variation of artificial lipid membranes 44
4.3.1 Topographical basis of artificial lipid membranes 44
4.3.2 CaL-induced destruction of lipid membranes 46
4.4 Topographies of cells infected by dCaL 56
4.4.1 Topographies of dCaL-infected cells in liquid 56
4.4.2 Topographies of dCaL-infected cells in air 57
4.5 Raman investigations of CaL and lipids 58
4.5.1 Conventional Raman spectra of CaL and lipids 58
4.5.2 SERS spectra of CaL and lipids 63
4.5.3 TERS spectra of dCaL 65
4.6 Investigations of dCaL-infected cells using TERS spectroscopy 67
4.6.1 SERS measurements on dCaL-infected cells 67
4.6.2 TERS measurements on dCaL-infected cells 68
4.7 Chapter summary 69
5. Investigations of SARS-CoV-2 using AFM and TERS spectroscopy 71
5.1 SARS-CoV-2 71
5.2 Experiments 74
5.3 Topographic and mechanic information on SARS-CoV-2 77
5.3.1 Topographies of SARS-CoV-2 virions 77
5.3.2 Mechanic information on SARS-CoV-2 82
5.4 Raman spectra of SARS-CoV-2 92
5.4.1 Conventional Raman and SERS measurements 92
5.4.2 TERS measurements on SARS-CoV-2 94

5.5 Chapter summary 98
6. Summary 99
Zusammenfassung 101
References 103
Acknowledgements 112
Publications and Conference Presentations 114
Selbständigkeitserklärung 116

Abbreviations

ACE2	Angiotensin-converting enzyme 2
AFM	Atomic force microscope/microscopy
AMP	Antimicrobial peptide
BMPO	5-tert-Butoxycarbonyl-5-methyl-1-pyrroline-N-oxide
(d)CaL	(deuterated) Candidalysin
DNA	Deoxyribonucleic acid
DOPC	1,2-dioleoyl-sn-glycero-3-phosphocholine
(D)PBS	(Dulbecco's) phosphate buffered saline
DPPC	1,2-dipalmitoyl-sn-glycero-3-phosphocholine
ESR	Electron spin resonance
HIV	Human immunodeficiency virus
NA	Numerical aperture
NSOM	Near-field scanning optical microscope/microscopy
PC	Phosphocholine
PFA	Paraformaldehyde
RBD	Receptor-binding domain
RNA	Ribonucleic acid
RT-PCR	Reverse transcription-polymerase chain reaction

SARS-CoV-2	Severe acute respiratory syndrome coronavirus 2
SEM	Scanning electron microscope
SERS	Surface-enhanced Raman scattering
SLBs	Supported lipid bilayers
SPM	Scanning probe microscope/microscopy
STED	Stimulated emission depletion
STM	Scanning tunneling microscope/mircroscopy
STORM	Stochastic optical reconstruction microscope
TEM	Transmission electron microscope
TERS	Tip-enhanced Raman scattering
UV-Vis	Ultra-violet visible
VLP	Virus-like particle
XPS	X-ray photoelectron scattering
XRD	X-ray powder diffraction

List of Figures

Fig. 1 The schematic diagrams of different probes of NSOMs 6
Fig. 2 Optical principle of STED microscopy. 7
Fig. 3 Timeline of some representative nanoscale-resolution techniques. 8
Fig. 4 Scheme of the fundamental structure of an AFM. 9
Fig. 5 Jablonski diagram of Raman, IR, and fluorescence. 11
Fig. 6 Schematic diagram of a localized surface plasmon. 12
Fig. 7 Schematic diagram of a TERS setup using bottom illumination 15
Fig. 8 Difference of a Ag6 SERS substrate before and after rinsing with water. 23
Fig. 9 Conventional Raman and SERS spectra of adenine. 24
Fig. 10 Solvent effects of $MgSO_4$, Tris, and PBS solutions on Ag6 substrates.. 25
Fig. 11 SEM images of Ag25 TERS tips before (a) and after (b) rinsing with PBS. 26
Fig. 12 Solvent effects on Cr3Ag6 substrates. 27
Fig. 13 SERS spectra of dCaL measured in liquid at different powers. 28
Fig. 14 Three different effects deriving from LSPR of plasmonic nanoparticles (PNP) and their applications 29
Fig. 15 Photocatalytic mechanisms of Ag, Ag_2O and Ag_2O@Ag. 30
Fig. 16 ESR spectrum of a BMPO-radical adduct from a Cr3Ag6 substrate. 31
Fig. 17 SERS spectra of dCaL with and without dCaL treatment. 32
Fig. 18 XPS spectra of elements C, O, Ag and I from an iodide-treated Cr3Ag6 substrate. 33
Fig. 19 XRD spectra of iodide-treated SERS substrates. 34
Fig. 20 SERS spectra of dCaL with and without excess iodides on an iodide pre-treated SERS substrate. 35
Fig. 21 Possible mechanism of iodide-treatment on Ag SERS substrates. 36
Fig. 22 (a) Strong reproducibility of SERS measurements with iodide-treatment and (b) comparison of conventional Raman and SERS spectra of dCaL 38
Fig. 23 Conventional Raman and SERS spectra of Melittin. 39
Fig. 24 (a) Schematic diagram of the penetration of CaL upon cell membrane and (b) 3D structural model and amino acid sequence of CaL. 41
Fig. 25 Conventional optical microscope images of cells treated with (a) and without (b) dCaL....43
Fig. 26 Cell membrane model 45
Fig. 27 Schematic diagram of DOPC/DPPC bilayer membrane.. 46

Fig. 28 Membrane reorganization in a low coverage case induced by 0.2 μM CaL. 48
Fig. 29 Domain variations in the low coverage case induced by 0.2 μM CaL. 48
Fig. 30 Membrane reorganization in a high coverage case induced by 0.2 μM CaL. 49
Fig. 31 The DPPC Domain variation in the high coverage case induced by 0.2 μM CaL. 49
Fig. 32 'Freezing' of membranes with 0.6 μM CaL.. 51
Fig. 33 Domain variations at the concentration of 0.6 μM. 51
Fig. 34 Membrane alteration on a high coverage case induced by CaL at a concentration of 2.5 μM using time-lapse AFM.....52
Fig. 35 The variation of DPPC domains at a concentration of 2.5 μM. 53
Fig. 36 Dynamical variations of membrane destructions. 54
Fig. 37 The mode of action of AMPs. 55
Fig. 38 Proposed modes of action of CaL at different concentrations. 56
Fig. 39 AFM images of a dCaL-infected cell in liquid. 57
Fig. 40 AFM images of a dCaL-infected cell in air.....58
Fig. 41 Conventional Raman spectra of DOPC and DPPC. 59
Fig. 42 Conventional Raman spectra of CaL and dCaL. 60
Fig. 43 Conventional Raman spectra of CaL/dCaL and lipids. 61
Fig. 44 Conventional Raman spectra of DOPC/DPPC vesicles and mixtures. 62
Fig. 45 (a) Conventional Raman spectra of a DOPC-DPPC vesicle with and without dCaL. (b) Conventional Raman spectra of DOPC-DPPC vesicle and mixture with dCaL. 63
Fig. 46 Conventional Raman and SERS spectra of (a) CaL, (b) dCaL, (c) DPPC and (d) DOPC 64
Fig. 47 Selected TERS spectra of dCaL. (a) TERS spectra, (b) Contour image and speculation of spectral difference and (c) Assignments of spectra. 65
Fig. 48 SEM images of TERS tips- (a) Ag25 and (b) Cr3Ag25 tips after measurements of dCaL samples. 66
Fig. 49 SERS spectra of dCaL and dCaL-infected cells. 67
Fig. 50 Selected TERS spectra around a pore of a dried dCaL-infected cell. 68
Fig. 51 The assignment of selected TERS spectra on a dCaL-infected cell. 69
Fig. 52 COVID-19 cases with or without COVID-19-relevant symptoms and the proportion of deceased and hospitalised casesin Germany from Week10, 2020 to Week19, 2021. 71
Fig. 53 A schematic diagram of coronavirus 72
Fig. 54 Data processing of force measurements. 76
Fig. 55 AFM images of a SARS-CoV-2 virus sample in a scale of 5x5 μm^2 which were cultured in Vero76 cells. 77

Fig. 56 AFM images of a virus-like particle. (a) Topography image; (b) Phase image; (c) A profile on the virus; (d) 3D image. 78
Fig. 57 AFM images of 9 selected virus-like particles in different sizes and topographies. 79
Fig. 58 AFM images of different materials. 80
Fig. 59 AFM images of a cell medium sample. 81
Fig. 60 (a) Force-distance curve of AFM and (b) Topography, adhesion, and Young's modulus map of a virus-like particle. 82
Fig. 61 Topography images of a virus-like particle and PFA aggregates and profiles at two specified positions. 83
Fig. 62 Adhesion (a) and Young's modulus (b) maps of a PFA sample and their relative distributions 84
Fig. 63 Adhesion and Young's modulus maps of a virus-like particle and their relative distributions. 85
Fig. 64 (a) Comparison of a virus-like particle and different PFA aggregates and (b) The distribution of Young's (elastic) modulus as a function of adhesion of different targets. 86
Fig. 65 Force measurements of the same virion with 3 different setpoints. 87
Fig. 66 Distributions of Young's moduli versus adhesions of 3 virus-like particles which show that the mechanical properties of these particles under the experimental setting were close to each other. 88
Fig. 67 Comparison of 3 virus-like particles concerning their topographies, adhesion, and Young's modulus maps. 89
Fig. 68 Comparison of Young's modulus maps of different virus-like particles. 90
Fig. 69 (a) AFM-correlated conventional Raman spectra of a virus-like particle (VLP); (b) SERS spectra of a virus sample and band assignments on 7 labelled bands... 92
Fig. 70 SERS spectra of S protein and virus sample vi5587. 93
Fig. 71 SERS spectra of BSA and BSA-PFA complex. 93
Fig. 72 AFM topography and TERS spectra on (a) and off (b) VLP04303. 94
Fig. 73 Assignments of TERS spectra of VLP04303. 95
Fig. 74 TERS spectra and their assignments of a virus-like particle.. 96
Fig. 75 Topography images and TERS spectra of 3 different virus-like particles. 97
Fig. 76 Comparison of 2 different virus-like particles from 2 different tips. 97

List of Tables

Table 1 Comparison of cross-sections in various spectroscopies.....12
Table 2 Materials used in this work 18
Table 3 Instruments used in this work.....19
Table 4 The assignment of main Raman bands of DOPC and DPPC.....59
Table 5 The assignments of main Raman bands of CaL and dCaL.....60
Table 6 Seven known human coronaviruses.....72
Table 7 Overview of SARS-CoV-1, MERS, and SARS-CoV-2 73
Table 8 Ratios of hard core to soft part in Young's modulus maps of virus-like particles 91

Motivation and Abstract

Motivation

The human thirst for knowledge is to a great extent responsible for the development of techniques towards exploring the remote universe, as well as the nanoworld. The emergence of nano-imaging techniques enabled people to investigate the nanoscopic scale, which is commonly done with super-resolution techniques. Furthermore, optical microscopy is no longer the only technique, which can observe objects on the nanoscale. Atomic force microscopy (AFM), for example. can 'sense' nano-features of targets while tip-enhanced Raman scattering (TERS) spectroscopy can even 'display' nano-structural/chemical information of samples.

For a very long time, conventional far field optical microscopy was the only way to investigate the microscopic world, however, its resolution is restricted to around 200 nm following the classic theory of the optical diffraction limit. Luckily, benefiting from advanced engineering, new techniques successively broke this limit during the past 100 years. Utilizing electron beams with extremely short wavelength of electrons, electron microscopes easily realize nanometer resolution. By implementing super sharp probes, scanning probe microscopy (SPM) joins into the group of super-resolution techniques. The development of super-resolution techniques overcame the diffraction limit of conventional optical microscopes.

When super-resolution bio-related works are mentioned, far-field super-resolution fluorescent techniques often lead the way. No doubt, these techniques have made remarkable achievements, still the fluorophore labeling intrinsically limits the applicability of these fluorescent techniques. Additionally, microscopy cannot give infomration on the chemical composition of samples. In contrast, AFM and Raman spectroscopy have the inherent advantages of exploring nanoscale properties and acquiring chemical information without labeling, respectively. Since the emergence of Raman scattering, techniques combined with Raman scattering have attracted enormous attention. Based on characteristic molecular vibrations, chemical information can be analyzed and read-out from a Raman spectrum. In conventional Raman spectroscopy, the low scattering efficiency and the optical diffraction limit present obstacles, however, these are overcome by subsequently developed techniques. By making use of the surface plasmon resonance effect, enhanced Raman

spectroscopy, such as surface enhanced Raman scattering (SERS) spectroscopy, the low Raman scattering cross section is overcome. Combined with an SPM like AFM, AFM-TERS spectroscopy gains a high sensitivity as well as a high spatial resolution. Even though SERS and TERS spectroscopy are powerful techniques, currently, there is still much space for development. Sample degradation, for instance, is a common issue in enhanced Raman spectroscopy and no convincing method addressing sample degradation has been presented so far.

As a result of the rapid development of science, humanity has reached an unprecedented level of understanding the origin of life. In the meantime, health issues are also increasingly well-studied. For example, *Candida*, a type of fungus firstly described already 150 years ago, infects millions of people and claims hundreds of thousands of lives every year. Almost everyone will suffer from Candidiasis at least once in their life, as the pathogenesis of *Candida* family is not well known yet. Only recently, Candidalysin (CaL), the first recognized fungal peptide, has been found to play a key role in the invasion of *Candida albicans*. To understand the behavior of CaL may help people eliminate diseases caused by this fungus. Currently, the mode of action of CaL upon human cells is still unclear. Clearly, to study the behavior of CaL will contribute to further research and therapies of *Candida*-induced diseases.

Apart from fungi, viruses, as another kind of lethal pathogen, should not be ignored. The year 2020 was exceptional due to the global pandemic of a new coronavirus — severe acute respiratory syndrome coronavirus 2 (SARS-CoV-2). In the very beginning, none of us could have imagined that this virus would cause more than 76 million infections and claim more than 1,6 million lives worldwide within 12 months. SARS-CoV-2 has become one of the worst acute viruses in human history. Even worse, the situation does not show any sign of getting better after one year. The high false negative rate (up to 30%) of current detection techniques increases the risk and uncertainty. It is necessary and urgent to find other supplementary methods or even substitutes for the detection and analysis of this virus. How to defeat SARS-CoV-2 seems to be the only mutual global goal at the moment.

Obviously, super-resolution techniques seem promising in the research of pathogens. Both the unknown mode of action of CaL and the detection and analysis of SARS-CoV-2 catch our attention. In using AFM and enhanced Raman spectroscopy for the investigations of CaL and SARS-CoV-2 the methods will gain tremendous significance and at the same time the development of these super-resolution techniques will be improved.

Abstract

In this thesis, AFM and enhanced Raman spectroscopy were applied for investigating the mode of action of CaL and the detection of SARS-CoV-2. Last but not least, a simple method for suppressing sample degradation in enhanced Raman spectroscopy will be introduced.

Chapter 1 introduces some representative super-resolution techniques, including near-field scanning optical microscopy, far-field super-resolution fluorescent microscopy, and non-optical microscopy. Among these techniques, atomic force microscopy and Raman spectroscopy are highlighted. The principle of atomic force microscopy in topographical and mechanical research is explained in Chapter 1.2. Raman spectroscopy, including conventional Raman, SERS, and TERS are specified in Chapter 1.3. A short outline of this thesis is listed in Chapter 1.4. All instruments and experimental materials used in the experiments are discussed in Chapter 2. Investigations of water-resistant silver (Ag) SERS substrates are presented in Chapter 3. More importantly, a simple and very promising method, which suppresses sample degradation in enhanced Raman spectroscopy, will be firstly introduced in this chapter. This method furthermore improves the reliability and reproducibility of measurements using enhanced Raman spectroscopy. Chapter 4 is concerned with the applications of AFM and enhanced Raman spectroscopy in the investigations of the fungal peptide CaL. The mode of action of CaL, especially its pore formation, is investigated and discussed using AFM and Raman spectroscopy for the first time. The same AFM-TERS setup was also used to investigate SARS-CoV-2. Topographical, mechanical, and chemical information of SARS-CoV-2 virions are presented in Chapter 5. It is found that with the combination of topographical and mechanical information, AFM was able to recognize virions. TERS was preliminary applied to the analysis of the surface chemical compositions of virus-like particles. The AFM-TERS method is thought to be a promising supplementary approach for the detection of SARS-CoV-2.

1. Introduction

1.1 Super-resolution techniques

Nanoscale-level research is crucial in the investigation of life sciences like pathological analysis and drug development. Numerous techniques like microscopy and spectroscopy have been invented and improved to achieve single molecule imaging, molecular tracking, structural characterization, *etc*. The key goal of these techniques is a better spatial resolution. Microscopy is used to directly visualize tiny objects, while spectroscopy is applied to study the energy-matter interaction. Based on the difference of signal detection they can be further divided into optical and non-optical microscopy/spectroscopy. It is worthwhile to pursuit and to apply techniques with higher resolutions in scientific research.

1.1.1 Beyond Abbe diffraction limit

For quite some time now, humans have used optical microscopes to observe and explore the microscopic world. However, the limit of spatial resolution restricts research. In 1873, Ernst Abbe[1] proposed the famous Abbe diffraction limit (Eq.1) in which the spatial resolution of traditional optical techniques is found to be limited to almost half to one-third wavelength of the incident light.

$$d = 0.61\ \frac{\lambda}{NA} \qquad \text{Eq. 1}$$

Based on this equation, an easy way to improve the resolution (d) is to use a shorter wavelength (λ) of light but the range of visible light limits this. Another possibility is to increase the numerical aperture (NA) whilst the largest NA is only around 1.5. In other words, the highest lateral resolution of a traditional optical microscope is limited to around 200 nm. The resolution of traditional optical techniques was indeed hampered by this limit for a long period. Edward Synge[2] firstly introduced the approach of a special optical setup in 1928 which shed the light on how to overcome the diffraction limit. The basic idea Synge presented was to manufacture a tiny apperture as a light source. Even though the approach was suggested, it took until 1982 to be experimentally implemented by Dieter Pohl for the first time[3]. There was a 50-year gap in this field caused by technical difficulties. In fact, this is the first approach towards near-field optics.

In subsequent developments, researchers were aware of the different ways of

electromagnetic propagation, depending on the distance of objects, which are defined as near and far field[4]. Gernerally, near field is a region where the electromagnetic field is non-propagating and limited to a few hundred nanometers from the object surface. This part of an electromagnetic wave is also called evanescent wave, which is the key factor to break diffraction limit in near-field techniques. In contrast, far field dominates a larger distance which is the part detected by traditional microscopes. Roughly, near and far field can be distinguished based on whether evanescent waves play a major role. Accordingly, optics can be divided into near-field and far-field optics. Based on these terms, it is understood that the Abbe diffraction limit only applies to far-field traditional optics and is broken by near-field techniques like Synge's approach.

1.1.2 Super-resolution optical techniques

1.1.2.1 Near-field scanning optical microscopy

Nowadays, a number of near-field optical techniques have been invented and developed. The lateral resolution of these near-field techniques quickly surpassed the scale within 50 nm[5, 6] and even within 10 nm[7, 8]. One of the representative techniques is near-field scanning optical microscopy (NSOM), which, in fact, is classified as one kind of scanning probe microscopy (SPM)[9, 10].

As shown in Fig. 1, near-field scanning optical microscopes are mainly comprised of a hollow or solid probe in the dimension of tens of nanometers, which is also called 'apertured' and 'apertureless' mode, respectively. A probe, like an antenna, converts near-field energy into far field and vice versa. Thus, this phenomenon is also referred to as 'antenna effect'[11, 12]. In further development, colloidal particles are attached to the apex of the probe or a metal tip is used in order to utilize its plasmon resonance effect[13]. Benefiting from the excellent spatial resolution, NSOM is promising in nanoscale imaging and single-molecule spectroscopy.

Furthermore, as a type of SPM, NSOM can be flexibly combined with other instruments, e.g. fluorescence[7] and Raman spectroscopes[14]. Höppener *et al.*[15] realized the imaging of membrane proteins in physiological conditions using a fluorescence-correlated NSOM. Their approach successfully showed that near-field fluorescence provides a better spatial resolution than a normal confocal fluorescent microscope for imaging membrane proteins and to analyze the inter-protein distances. Another example, one of the first TERS setups was manufactured based on NSOM in 2000[14], which is not only an imaging instrument but nowadays also accomplishes the

component analysis of samples. Presently, more TERS setups are combined with other SPMs like scanning tunneling microscope (STM) or AFM[16]. More detailed explanations about TERS spectroscopy will be introduced in Chapter 1.3.3.

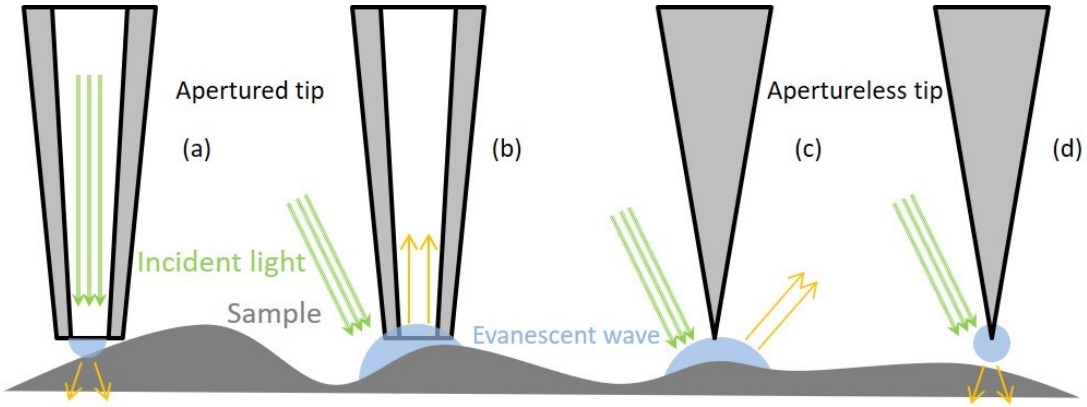

Fig. 1 The schematic diagrams of different probes of NSOMs (not to scale, only the probes and evanescent wave are illustrated). (a, d) An evanescent wave, which is used to illuminate samples, is produced at the apex of the aperture tip. (b) An apertured probe is used to collect the evanescent wave formed on the surface of the sample. (c) An apertureless tip scatters the evanescent wave away from the sample surface.

In NSOM the resolution mainly depends on the dimension of its probes. Generally, a resolution of 50 nm can be obtained. Therefore, NSOM brings optical research into the nanoscale and apparently promotes the development of near-field optics. The method benefits from its probes but at the same time is limited by them. The manufacturing of a good probe is the key step in this field. Typically, apertured probes have the drawback of low light intensity, at the same time it is very difficult to fabricate a very sharp apertured tip.

1.1.2.2 Far-field super-resolution fluorescence microscopy

During the direct transition of electrons from their electronically excited states to ground states, photons are emitted which is called fluorescence[17]. As a non-destructive technique, fluorescence microscopy is widely used in life sciences-related research like live cell imaging. In an early stage, even though a confocal microscope improves the axial resolution the lateral resolution is still limited by the diffraction limit[18]. The introduction of far-field super-resolution techniques shifted fluorescence microscopy genuinely to the nanoscale-resolution level[19].

A frequently used super-resolution technique is stimulated emission depletion (STED) microscopy. It selectively deactivates the light of fluorophores, which cleverly decreases the size of illumination and further improves the resolution to tens of

nanometers or even better[20]. Remolding the size of the light source is a very smart way to overcome the Abbe diffraction limit. Fig. 2 gives the basic principles of STED. Compared to a conventional microscope, a STED microscope is constructed with two laser beams. The second beam is a STED light with a doughnut shape in which the central part has zero intensity. When the first beam is superimposed by the STED beam, the peripheral light from a fluorophore will be deactivated and only the central part will yield the signal. Thereby, STED narrows the light spot beyond the diffraction limit. A lateral resolution of 20 nm has been reported[21]. Be that as it may, the biggest issue of fluorescence is fluorophore labeling, as fluorophores will affect the chemical/physical properties of targets.

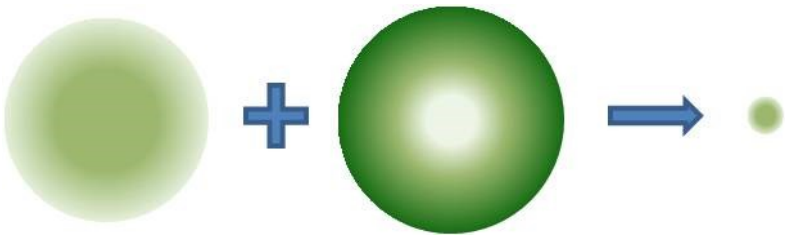

Fig. 2 Optical principle of STED microscopy. The STED light (middle) narrows the light spot (left) by interrupting electron transitions.

1.1.3 Super-resolution non-optical techniques

Next to optical techniques, there are also many non-optical techniques like scanning probe microscopy and electron microscopy, which provide superior resolutions in measurements by taking advantages of mechanics or electronics. Electron microscopy, for example, is a technique, which collects electrons that scatter, reflect, or transmit from the sample. Scanning electron microscopes (SEM) and transmission electron microscopes (TEM) are two common instruments in electron microscopy. Benefiting from the extremely short wavelength, electron microscopes have a much better resolution than conventional optical microscopes. A resolution of sub-50 pm has been realized with an electron microscope[22]. Electron microscopy is broadly used in life sciences imaging the surfaces of samples from macromolecules to cells and tissues. During the outbreak of SARS-CoV-2, electron microscopy has played a very important role in corresponding research. With a TEM the structure of the coronavirus with its spike proteins was clearly imaged[23]. The authors presented the spike in post-fusion state, which has a width of 7 nm and a length of 23 nm and therefore is very difficult to image using AFM. Furthermore, research using a cryogenic electron microscope resolved the 3D structure of the spike protein of SARS-CoV-2 in prefusion state with a resolution of 3.5 angstroms (Å)[24]. Electron microscopy, indeed, shows an excellent

resolution of the analysis of superfine structures. However, the necessary ultra-high vacuum (UHV) environment in an electron microscope limits its application on living samples. Additionally, carbonation of samples caused by electron beams often affects the measurements. In contrast, SPM is more versatile and flexible.

Generally, techniques which provide a resolution higher than the Abbe diffraction limit can be categorized as super-resolution. A simplified timeline about the above-mentioned super-resolution microscopes/spectroscopes is presented in Fig. *3* In this thesis, the focus lies on the application of AFM and AFM-TERS spectroscopy. As they go beyond the scope of this work, other super-resolution technologies will not be introduced.

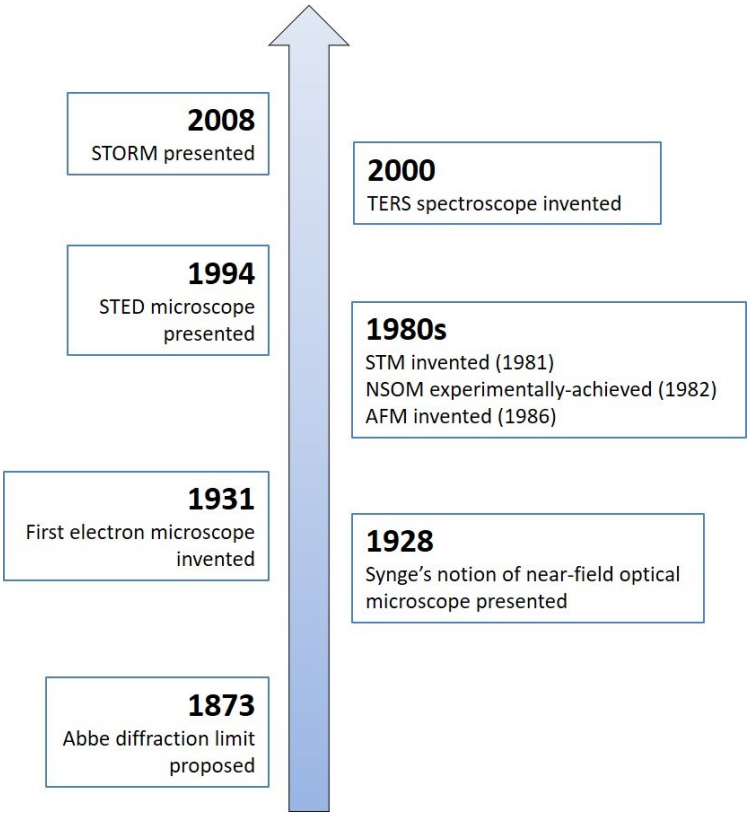

Fig. 3 Timeline of some representative nanoscale-resolution techniques.

1.2 Atomic force microscopy

The first SPM to be invented was STM in 1981[25], which was followed by the introduction of NSOM in 1982 and AFM in 1986[26], respectively. SPM realizes nanoscale measurements on the surface of samples with the aid of a physical probe. The spatial resolution of an SPM instrument is mainly determined by the apex size of the probe/tip. Compared with super-resolution fluorescence, SPM is a non-invasive and label-free technique for the characterization of surfaces and interfaces. The

topographical, optical, electrical, and mechanical information of samples can be investigated and acquired using SPM with a spatial resolution up to tens of nanometers.

As one type of SPM, AFM images samples by making use of the interaction between tip and sample. The imaging process involves complex interactions, like mechanical contact force, electrostatic force, and Van der Waals force. However, these go beyond the topic of this work and will not be discussed in detail here. Fig. 4 shows a simplified working principle of an AFM. When a tip scans the surface of a sample, the interaction between the tip and sample can be 'felt' by the bending of the cantilever, which is detected by a photodiode (i.e., the sensor). Those electrical signals will be recorded and further re-converted into images. This way, the topographical and mechanical information of samples can be obtained. Based on the specific operation, the imaging modes can be divided into tapping mode, contact mode, and non-contact mode, whereof the first two modes are the most common. In tapping mode, a cantilever is oscillated with a fixed amplitude near its resonance frequency. When the tip approaches the surface interactions from samples lead to a frequency shift of the cantilever resonance, this automatically also changes the detected amplitude. The feedback loop regulates the tip to a specified amplitude by approaching or retracting, respectively, the tip to the surface or vice versa. In contrast, contact mode sets a constant force on the cantilever. During the imaging process, the tip will directly touch and be moved on the surface of the sample. Compared to tapping mode, contact mode can provide a better imaging contrast while it increases the risks of sample damage and/or tip contamination.

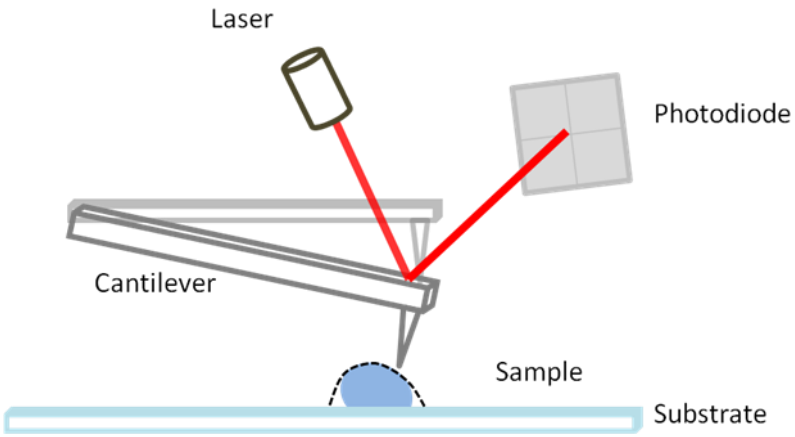

Fig. 4 Scheme of the fundamental structure of an AFM (Not to scale).

Compared to other SPMs, the greatest advantage of AFM is that there are no special requirements concerning sample preparation and substrates. With an AFM setup samples can be measured in both air and liquid conditions, which means the original

biophysical natures of samples can be kept. Furthermore, tips and substrates can be made out of any kind of material, however, coverslips and other glass slides are used, normally. Moreover, a transparent substrate also makes the combination of AFM with other instruments easier and more flexible. Surely, SPM is powerful, nevertheless, its own limits cannot be ignored. The spatial resolution of SPM is mostly determined by the dimension of the tips. For example, a tip with a 10 nm radius could provide a lateral resolution up to 20 nm. Fig. 4 also illustrates the imaging of AFM. When the sample has some corners, which cannot be touched by the apex of the tip, the topographical image we see is the dashed line, rather than the genuine morphology. In other words, an AFM topographical image is a convolution image of tip and the sample morphology. Also, it is very easy to obtain imaging artifacts in SPM due to tip abrasion and contamination. Thus, choosing a suitable tip and scan settings is very important for successful SPM imaging. In this work, lots of AFM experiments were made to investigate the interaction of the fungal peptide CaL with artificial lipid membranes using tapping mode.

With a skillful combination of different techniques, the application of SPM is lifted to a higher level. For example, TERS spectroscopy is a combination of AFM and Raman spectroscopy, which can simultaneously acquire images and chemical compositions of targets at the nanoscale.

1.3 Nanoscale-resolution Raman spectroscopy

1.3.1 Raman scattering

When a beam of light passes a matter, the light can be scattered/absorbed by the matter, whereby energies of the incident photons will be conserved, either by scattering with the same wavelength or by releasing energy shifted photons and generate heat. In the scattering processes, most photons will be elastically scattered, also called Raleigh scattering, while some will be inelastically scattered, also known as Raman scattering[27]. In Raman scattering, the effects of losing and gaining energies of photons are defined as stokes and anti-stokes scattering, respectively.

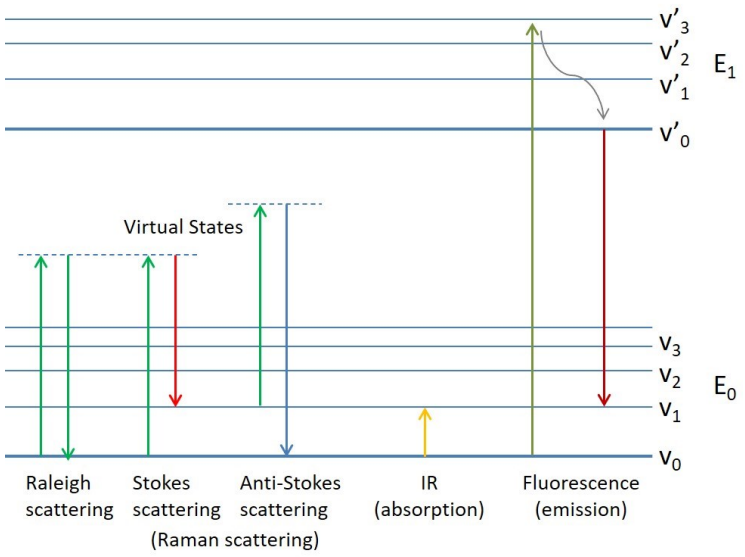

Fig. 5 Jablonski diagram of Raman, IR, and fluorescence. Colors are only for guidance. E_0: electronic ground state; E_1: electronically excited state; v and v': vibrational level.

In Fig. 5, the differences of Raman, Infrared (IR), and fluorescence spectroscopy are presented using a Jablonski diagram. During a scattering process, a molecule is excited by a photon from an electronic ground state to a virtual state which is equal to the extra energy of the photon and does not correspond to a defined quantum state of the molecule. After around 10^{-12}-10^{-10} s, this excited molecule will emit a photon and go back to a lower vibrational energy level ($v_{virtual} \rightarrow v_1$). The technique to detect this scattering process is called Raman spectroscopy. Because this scattering is generally caused by molecular vibrations or rotations, Raman spectroscopy is a vibrational spectroscopy. The variations of energies are correlated with special rotation or vibrations of chemical bonds. As spectral bands can always be assigned to specific chemical bonds, a Raman spectrum is often regarded as a molecular fingerprint. IR is an absorption spectroscopy, which involves the absorption of a photon and then the transition to a higher rotational/vibrational level ($v_0 \rightarrow v_1$) of the excited molecule. To some extent, IR can be used as complementary technique for Raman, as IR is detecting the dipole moments of molecules, while Raman detects the polarizabilities of electron clouds. Fluorescence spectroscopy belongs to the group of emission spectroscopy, which detects the emission of excited photons from the first electronic excited state (E_1) to the electronic ground state (E_0). However, the cross section of Raman scattering is only ~10^{-29} cm^2 sr^{-1} $molecule^{-1}$, which means Raman scattering is hard to detect. Conventional Raman spectroscopy is limited by its low sensitivity, additionally, the resolution of this optical far-field microscopy is bound by the Abbe diffraction limit. In contrast (see Table 1), the high cross section (~10^{-19} cm^2 sr^{-1} $molecule^{-1}$) of fluorescence

often interferes with the detection of the Raman effect [28]. Luckily, enhanced Raman spectroscopies like SERS spectroscopy overcome this issue.

Table 1 Comparison of cross-sections in various spectroscopies (adapted from Ref.[28])

Type	Physical process	Cross-section ($cm^2sr^{-1}molecule^{-1}$)
Raman	Scattering	10^{-29}
Rayleigh scattering	Scattering	10^{-26}
IR	Absorption	10^{-21}
Fluorescence	Emission	10^{-19}
SERS spectroscopy	Scattering	10^{-16}

1.3.2 SERS spectroscopy

In the 1970s, SERS was found to increase the Raman intensity of molecules by several orders of magnitude, which mainly results from the electromagnetic field enhancement caused by the surface plasmon[29, 30]. The surface plasmon corresponds to the collective oscillation of free electrons in metal particles (see Fig. 6) which is non-propagating and confined [31]. When a suitable wavelength matches the maximum absorption of electron oscillations, the resonant effect, called surface plasmon resonance (SPR)[32], can be achieved. SPR produced on nanostructures is also called localized SPR (LSPR)[33-35]. With the help of LSPR the Raman intensities of those molecules located in the near field region of SERS substrates will be dramatically enhanced up to 10^{10}-10^{12} times [36].

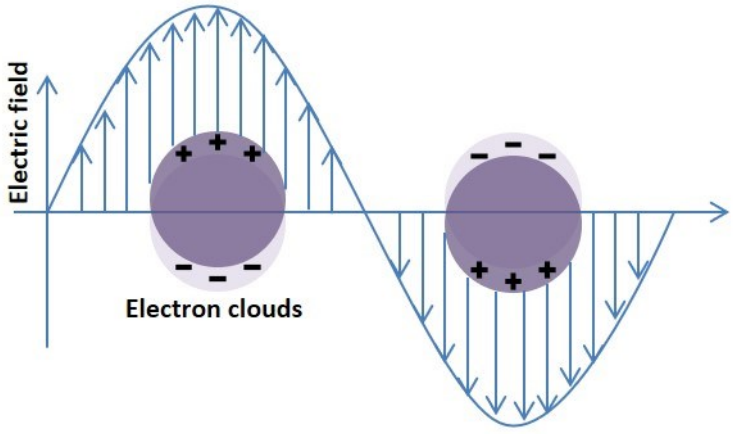

Fig. 6 Schematic diagram of a localized surface plasmon.

The cause for the enhancement of the local electromagnetic field can generally be divided into two parts. First, the electromagnetic field around metals is induced and enhanced by the incident light (ω_0). The enhancement factor $EF_{incident}$ is equal to the

square of the ratio of the incident light-induced electromagnetic field ($E_{LSPR}(\omega_0)$) and the electromagnetic field ($E(\omega_0)$) of the incident light. Second, the Raman-scattered light (ω) from molecules further increases the enhancement of the local electromagnetic field. The enhancement factor $EF_{scattering}$ is equal to the square of the ratio of scattered light-induced electromagnetic field ($E_{LSPR}(\omega)$) and the electromagnetic field ($E(\omega)$) of the scattered light. The total enhancement factor (EF) to the electromagnetic field is a superposition of the two parts. In a low frequency scattering, the frequencies of the incident (ω_0) and scattered (ω) light are almost the same. In other words, $E_{LSPR}(\omega_0)$ and $E(\omega_0)$ are closing to $E_{LSPR}(\omega)$ and $E(\omega)$, respectively. Thus, the enhancement factor of a SERS scattering can be approximately expressed in Eq. 2 as the fourth power of the relative field enhancement. From the equation it is obvious that even a weak electromagnetic enhancement of LSPR can contribute to the final enhancement of Raman intensity. Apart from the electromagnetic field enhancement, chemical enhancement of samples is another contributor to SERS, which depends on the interaction of nanoparticles and absorbed samples. Chemical enhancement (~10^2) contributes much less, though, than electromagnetic enhancement (~10^{10}-10^{12})[37].

$$EF = EF_{incident}EF_{scattering} = \left(\frac{\mathrm{E_{LSPR}}\left(\omega_0\right)}{\mathrm{E}\left(\omega_0\right)}\right)^2\left(\frac{\mathrm{E_{LSPR}}\left(\omega\right)}{\mathrm{E}\left(\omega\right)}\right)^2 = \left(\frac{\mathrm{E_{LSPR}}\left(\omega_0\right)}{\mathrm{E}\left(\omega_0\right)}\right)^4 \qquad \text{Eq. 2}$$

It has been confirmed that a lot of metals, which have a broad response to a large scale of wavelength from UV to IR[38], have the SPR effect. Nowadays, the most commonly used metals are gold (Au)[39] and silver (Ag)[40, 41]. Ag nanoparticles can provide a higher enhancement factor than Au while they oxidize easily and, thus, lose their SPR effects. Nanoparticles in different structures are designed which are also found to have various electromagnetic distributions on the surface[42]. It is also found that, generally, clusters have higher enhancements than single particles[43]. In this thesis, SERS substrates assembled with spherical Ag particles on coverslips using physical vapor deposition (PVD) were used in the experiments.

There are some disadvantages to SERS spectroscopy, which should be noted. Firstly, the local heating effect increases the risk of sample degradation and the possible fusion of nanoparticles. Temperatures at the laser spot will be boosted up several tens of degrees or even higher[44, 45]. Thus, the thermal effect must be considered in SERS experiments. Typical features of sample degradation of organic compounds are two very broad and strong peaks at 1350 cm^{-1} and 1570 cm^{-1}, which originate from

carbonaceous material[46]. Commonly, lower laser power is suggested to avoid or reduce sample degradation. Secondly, the scale of LSPR is highly confined which means only signals of chemical bonds located within the enhanced electromagnetic field can be amplified and detected. Additionally, the interactions between nanoparticles and samples will affect the vibration/rotation of samples and then affect the spectra. SERS substrates also often show selectivity on different samples[47]. Compared to a conventional Raman spectrum of a sample it is often found that there is a difference in its SERS spectrum, where some bands disappear while others are newly formed. Therefore, a conventional Raman spectrum as reference is crucial in enhanced Raman measurements.

1.3.3 TERS spectroscopy

Even though SERS spectroscopy improves the detection sensitivity of Raman spectroscopy up to a single molecule, as a lens-based optical microscope it is still restricted by the Abbe diffraction limit. In contrast to SERS spectroscopy, TERS spectroscopy has its extra advantage of nanoscale spatial resolution[38, 48]. Benefiting from the combination with SPM, TERS spectroscopy, which was firstly mentioned in 2000[14, 49, 50], can simultaneously acquire topographic and chemical information of samples within nanoscale resolution.

To some extent, TERS spectroscopy can be regarded as a kind of SERS-based spectroscopy. It takes advantage of LSPR of plasmon particles to obtain a high sensitivity, but it goes further beyond the Abbe diffraction limit with the electromagnetic field localized on nanoparticles. In TERS spectroscopy, the tip of the scanning probe microscope becomes the carrier of the plasmonic nanoparticles. Under illumination with suitable light, LSPR will be induced by these plasmonic particles. The scale of the electromagnetic field on a TERS tip corresponds to the resolution of the TERS measurement[51-53] and the dominant electromagnetic field is basically localized on the final particle of the tip. Thus, the spatial resolution of TERS spectroscopy is largely comparable to the size of the final particle. In fact, the spatial resolution has been confirmed to be better than the dimension of the particle. Generally, a 20 nm spatial resolution can be obtained from a current TERS setup[54]. Amazingly, the extremely high spatial resolution of 0.5 nm under ultra-high vacuum condition has been documented[55]. Under ambient conditions, it is possible to distinguish nucleobases of DNA and RNA[56, 57].

Apart from the role as carriers of plasmon nanoparticles, SPM is also very important in controlling the tip-sample distance. As the electromagnetic filed is localized on the very surface of the nanoparticles, the distance of tip-sample will highly affect enhancement factors and the signal to noise ratio (SNR) of signals or even measurements. Three different SPMs including STM, AFM, and shear force microscopy have become established in TERS setups[16]. These SPMs can control the tip-sample distance well within a few nanometers. The abrasion of the TERS tip in measurements of contact mode TERS should be also considered. Plasmonic nanoparticles will be removed easily due to the direct contact of tip and sample. An extra coating layer on these particles can protect the tip; however, this approach will sacrifice the intensity of the electromagnetic field and decrease the SNR of TERS spectra[58, 59].

To achieve a well-controlled TERS measurement, the optical part is just as crucial as the SPM part. First, a suitable laser wavelength should be chosen. For biological samples auto-fluorescence is a common influence on Raman measurements. This phenomenon should be avoided by the choice of a suitable laser wavelength. Second, the laser must be well aligned to the tip. For silicon-based tips, the silicon signal at 520 cm^{-1} is usually used as reference[54]. Third, it has been verified that the polarization of the laser will affect the enhancement of the electromagnetic field. Normally, a Gaussian beam is used as light source. Nevertheless, not all components of the light wave contribute to the LSPR. It is proposed that a radially polarized (z-axis) light provides a better efficiency for TERS measurements[60]. Compared to a Gaussian beam with the same output energy, such a polarized light can provide better SNR ratio and at the same time decrease the risk of sample degradation.

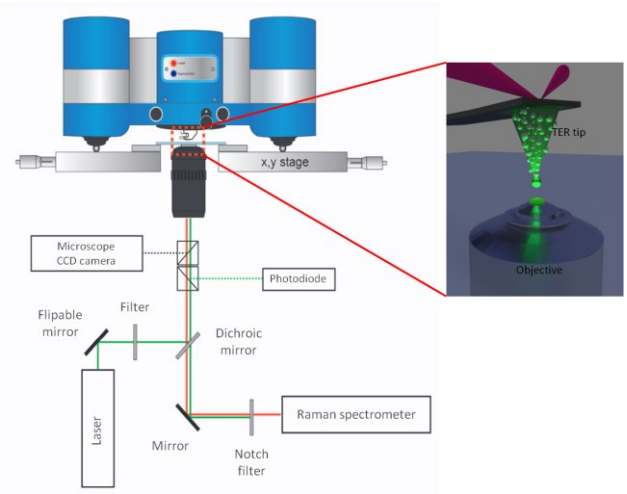

Fig. 7 Schematic diagram of a TERS setup using bottom illumination (not to scale, adapted from Ref. [61] The TERS tip inset is courteously provided by Dr. Christiane Höppener).

An SPM can be flexibly assembled with the corresponding Raman spectrometer with different configurations, such as bottom illumination, side illumination, and top illumination[62]. In a bottom-illuminated configuration the transparency of substrates and samples is clearly essential. In contrast, side- and top- illumination configurations are commonly used for measurements of opaque samples. The AFM-TERS setup used in this work is a bottom illumination configuration (see Fig. 7). In such a configuration an AFM head is located on a microscope stage while a laser beam enters from the bottom into the microscope and illuminates the tip. For visible light, coverslips and mica are used. Mica can provide an atomic-flat surface, which is often used in measurements of small targets like nucleobases. Additionally, freshly cleaved mica is negatively charged which can be used to immobilize samples with positive charges[63]. For an IR laser, coverslips are replaced by CaF_2 glasses to avoid IR absorption. Hence, a quartz substrate is preferred in a UV-TERS measurement.

As fewer chemical bonds will be in the direct the proximity of the localized electromagnetic field in TERS measurements, fewer bands will be detected. The blinking phenomena in enhanced Raman spectroscopy further hinders the assignments of spectra[64, 65]. Thus, a conventional Raman measurement is always suggested to increase the reliability of TERS spectra. Concerning the similar effect between SERS and TERS, a SERS spectrum is proposed as the second reference among conventional Raman and TERS spectra.

1.4 Nanoscale investigations of CaL and SARS-CoV-2 using AFM and enhanced Raman spectroscopy

All aforementioned techniques have broad applications in the investigations of biomaterials. However, there is no omnipotent technique applicable to every field. Every technique has its own advantages and disadvantages and is thus chosen or combined based on the requirements of experiments. NSOM and SPM can realize nanoscale imaging while they are limited by their low detection depths. Far-field super resolution fluorescent microscopy has no barrier on sample depths, but the fluorophores will greatly affect the dynamical natures of labeled targets. Additionally, detection sensitivity, quantum yield, and fluorescence lifetime all should be paid attention to. Interestingly, AFM could well be applied to thermodynamical and mechanical research without labelling. Electron microscopy provides an unprecedented spatial resolution. However, it has a very strict requirement on

experimental and/or sample conditions. Therefore, to choose suitable instruments and techniques is the key to realize the experiments.

Enhanced Raman spectroscopy is flexible and versatile in nanoscale research, but it also has its limits. Ag particles have weak adhesions to coverslips and tips. When Ag SERS/TERS measurements are conducted with liquid, the quick loss of Ag particles clearly weakens the acquired Raman signals, shortens the lifetime of plasmonics or even leads to unsuccessful measurements. Chromium is used to increase the water resistance of SERS substrates and TERS tips[66], which will be presented in Chapter 3. Sample degradation is another issue restrcting the measurements of SERS/TERS measurements. Studies show that local heating is one of the reasons[67-69]. In the following work, a different hypothesis based on hot carriers induced by plasmonics is considered another reason for sample degradation. More importantly, based on this hypothesis a simple method is presented to overcome the sample degradation.

To the influence of fluorophore labels to the exact behavior of CaL, fluorescent techniques were excluded in the investigations of CaL. A time-lapse AFM experiment was conducted to investigate the mode of action of CaL on an artificial lipid membrane model, which is presented in Chapter 4. To further explore the chemical information of CaL, Raman spectroscopy especially enhanced Raman spectroscopy was applied. TERS spectroscopy was used to detect the locations of deuterated CaL (dCaL) on the surface of dCaL-infected cells.

In chapter 5, an AFM-Raman strategy is described that was used for the detection of SARS-CoV-2. Topographical information acquired by AFM was used to recognize virus-like particles from other materials in viral samples. Mechanical measurements using AFM were found to further help the differentiation of virions from virus-like vesicles. Preliminary TERS measurements were conducted on the analysis of the surface compositional information of virus-like particles. This AFM-TERS strategy is expected to improve the accuracy of viral detection.

This thesis presents an innovative method for overcoming sample degradation on Ag SERS substrates. AFM and Raman strategies were applied in the investigations of CaL and SARS-CoV-2. These experiments pave the way and give hints about the application of AFM-Raman and AFM-TERS spectroscopy for other researchers. All studies show that AFM-TERS spectroscopy is becoming an increasingly important technique for bio-related investigations.

2. Materials and instruments

2.1 Materials

Materials used in this work are listed, except for auxiliary materials like glue and tape, in the following table. SERS substrates and TERS tips were both manufactured by silver evaporation onto glass slides or commercial AFM tips, respectively.

Table 2 Materials used in this work

Material	Brand	Specifications
5-tert-Butoxycarbonyl-5-methyl-1-pyrroline-N-oxide (BMPO)	Enzo Life Sciences	50 mM
1,2-dioleoyl-sn-glycero-3-phosphocholine (DOPC)	Avanti Polar lipids	25 mg/mL
1,2-dipalmitoyl-sn-glycero-3-phosphocholine (DPPC)		
Candidalysin (CaL)	Peptide Synthetics	1.4 mM
Deuterated Candidalysin (dCaL)		
Methanol	Roth	
Chloroform	Roth	
Hydroperoxide (H_2O_2)	Roth	30%
Nitric acid (HNO_3)	Roth	65%
Calcium carbonate ($CaCO_3$)	VWR	
Potassium iodide (KI)	SigmaAldrich	
Potassium bromide (KBr)	SigmaAldrich	
Potassium chloride (KCl)	SigmaAldrich	
Magnesium sulfate ($MgSO_4$)	-	
Phosphate buffered solution (PBS)	SigmaAldrich	
Tris(hydroxymethyl)aminomethane (Tris)	SigmaAldrich	
Ultra-pure water	Thermo	18MΩ • cm
AFM tip	Nano World	PNP-TR
	NT-MDT	NSG-10
	Budget Sensors	TAP-190 Al
	Bruker	MLCT
SERS substrate	Homemade	
TERS tip	Homemade	
Glass slide	Schott	18x18 mm^2
WillCo-Dish (glass bottom)	WillCo Wells	Ø 12 mm

2.2 Instruments

Main instruments involved in this work are listed in the following table.

Table 3 Instruments used in this work

Instrument	Brand	Model
AFM	JPK	NanoWizard® 1, 2, 3 and Ultraspeed
Electron spin resonance spectroscopy (ESR)	Bruker	Elexsys E580
Raman spectroscopy	Horiba/ S&I Instrument	-
SEM	Zeiss	-
UV-Vis spectrophotometer	Varian	Cary 5000
X-ray photoelectron spectroscopy (XPS)	Scienta Omicron	-
X-ray power diffraction (XRD)	Panalytical	X'pert Pro MPD

3. A simple method to suppress sample degradation in SERS spectroscopy

Benefiting from the high sensitivity and easy manipulation, SERS spectroscopy is widely used in different fields like pollutant analysis, food safety, sensors, forensics, *etc.*[38, 70-73] Two common materials are used in SERS measurements including colloidal nanoparticles and supported SERS substrates[38, 74-76].Colloidal nanoparticles are easy to prepare using chemical reductions, for example, citrate-reduced Ag colloids[77], however, its chemical impurities interfere with the measurements. In contrast, made by physical methods, supported SERS substrates are chemical-free[78]. In our group coverslip-supported Ag substrates made by physical vapor deposition (PVD) are commonly used. The absorption wavelength of particles is tunable by adjusting particle size and thickness. With a suitable annealing control, the size of particles is controlled at around 50 nm and the corresponding maximum absorption of this substrate is adjusted to around 500-600 nm. However, there are three common drawbacks to these substrates. First, the lifetime of the substrate is rapidly shortened in liquid. Ag nanoparticles will easily be rinsed away or react with salts in solutions. This limits the application of these substrates in liquid measurements. Second, samples, especially bio-samples, are found to be highly degraded on these SERS substrates. Finally, the low reproducibility and reliability makes the analysis of complex samples extremely difficult, which also exists in colloid-based SERS measurements. Regarding the similarity of SERS and TERS, these issues could also exist on AFM-TERS tips. Therefore, it is essential to overcome sample photodegradations, which will also be beneficiant in accomplishing a reliable and reproducible SERS measurement.

3.1 Experiments

SERS substrate preparation

SERS substrates were manufactured by PVD of Ag onto 18x18 mm^2 coverslips. 6 nm thick Ag films were evaporated onto coverslips and subsequently annealed at 290 °C. In this way, Ag films will transform into densely distributed Ag particles, which can be used for further Raman measurements (such a SERS substrate is abbreviated as Ag6). Due to the quick removal of pure Ag particles in liquids, a 3 nm chromium (Cr) layer was deposited on the glass slides using a sputtering method from a Cr target prior to the Ag evaporation to improve the Ag adhesion in solvents. Such a SERS substrate is abbreviated as Cr3Ag6 indicating the evaporated/sputtered thickness of the repective

metals. As a result, SERS substrates compatible for liquid measurements were obtained. It is important to mention that all preparation steps were either done in vacuum or under inert gas atmosphere (argon).

AFM imaging

The topographies of SER substrates were measured with the AFM Nanowizard Ultraspeed by JPK. The AFM tip Tap190 Al-G by NanoAndMore was used in measurements. The pixel of images was set at 256x256 and AFM images were processed by the JPKSPM Data Processing software[79] and Gwyddion[80].

UV-Vis absorption

Ag6 and Cr3Ag6 substrates were treated with 50 µL 1 M $MgSO_4$, 1 M Tris and 0.1X PBS for 20 min, respectively. After that, the substrates were rinsed 3 times with dH_2O of the same volume to remove the salt residues. The absorbances of these substrates were measured by a Cary5000 UV-Vis spectrometer. According to our previous results, the wavelength of the maximum absorption of Ag6 substrates is around 500-600 nm. Thus, the scanning range was set at 400-800 nm. The average time was 0.1 s and the data interval was 0.5 nm.

XPS

One Cr3Ag6 substrate was immersed in 1 mM KI solution for 30 min, which was then rinsed with dH_2O and used for XPS measurements. XPS was performed using a multiprobe system (Scienta Omicron) with a monochromatic X-ray source (Al Kα) and an electron analyzer (Argus CU) with a 0.6 eV spectral energy resolution. The spectra were fitted with a Gaussian Lorentzian line shape (C 1s, I 3d, S 2p) or a Lorentzian Asymmetric line shape (Ag 3d) after Shirley (C 1s, I 3d, Ag 3d) or linear (S 2p) background subtraction[81]. The spectra were calibrated using a C 1s peak (C-C peak, 284.8 eV).

ESR

ESR data were obtained by a Bruker Elexsys E580 spectrometer with an SHQE cavity and a liquid nitrogen temperature control unit. The spectra were measured at 80 K in X-band in CW mode with a modulation amplitude of 1 G at 100 kHz with a microwave power of 4.743 mW (15 dB) with 100 scans. A ~4x18 mm^2 slice of the Cr3Ag6 SERS substrate (~4 ng Ag) was placed in a 5 mm ESR tube, covered with 300 µL 50 mM BMPO (5-tertbutoxycarbonyl-5-methyl-1-pyrroline-N-oxide) solution. The sample was irradiated at 510 nm (bandwidth 80 nm) inside the cavity using a 200 W Hg (Xe) arc

lamp with a filter wheel, shutter, and multicore fiber (all LOT Oriel) at room temperature for 10 min. Afterwards 50 µL glycerin were added and the sample was cooled to 80 K. All spectra are referenced on 9.336 GHz and processed with EasySpin (5.2.28)[82] in Matlab (R2020a).

Raman

Both Raman and SERS measurements were acquired with a 532 nm laser. The detailed power and exposure time were varied depending on different experiments, this will be mentioned in each section separately. Data were treated by Origin (8.0 and pro 2020b).

XRD

Cr3Ag6 substrates were immersed in 1 mM KI solution for 30 min, which was rinsed with dH_2O and dried for following XRD measurements. The samples were measured with grazing incidence GIXRD. The incoming X-ray beam has an angle of for example 1.0° (omega-angle), which is fixed during the measurement. The detector-angle Theta was moved from 10° to 70° with 0.05°-steps. Due to the small omega-angle the beam penetrates the thin Ag-layer over a large area, thus more X-rays can be reflected from the film compared to the standard Bragg-Brentano-geometry, where the X-ray-beam-angle and the detector-angle are moved.

The GIXRD measurements were performed with a parallel X-ray beam to prevent peak-shifting. The divergent beam from the X-ray tube is sent through a parallel mirror to parallelize the beam. The parallel mirror was equipped with a receiving slit 1/8° and a 10mm mask, which results in high peak-intensities and narrow peak widths. Only nearly parallel reflected X-rays pass a parallel plate collimator with 0.18° opening in front of the detector. The PIXCEL-detector operates in Receiving Slit mode with the maximum of 255 channels.

3.2 Ag SERS substrates

In experiments, Ag6 SERS substrates were found to be sensitive to water and other solvents, as Ag particles will be easily rinsed away by water (Fig. 8). After rinsing with water, the color of the substrates faded. The average number of Ag particles in 1 μm^2 decreased from 408 to 352. The size of Ag particles changed from ~39 nm diameter before rinsing to ~44 nm after rinsing (averages from 3 different and random 1x1 μm^2 positions). In the UV-vis spectra, the absorbance of the rinsed substrate showed a blue-shift, however, still located at around 550 nm. Another clear topographical change was

not found. The interaction between H_2O and Ag particles after a short rinsing period can almost be ignored. It is assumed that only some small Ag particles were rinsed away. However, the chemical reaction between Ag and salts in solution changes the compositions of substrates and may affect measurements using SERS substrates.

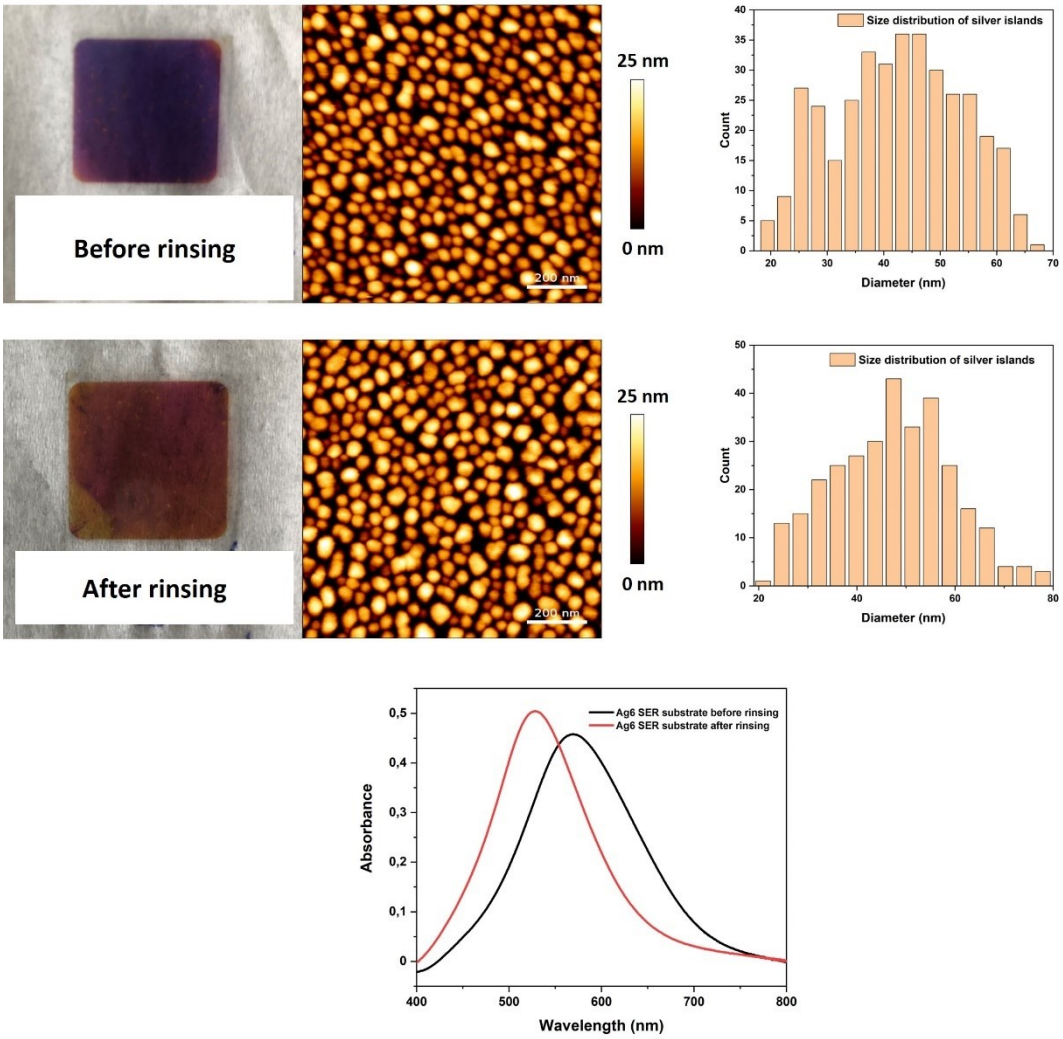

Fig. 8 Difference of a Ag6 SERS substrate before and after rinsing with water. After water rinsing, the color of the substrate faded and the UV-Vis spectra show a clear blue-shift of this substrate.

The SERS substrate interaction with salt solutions is more complex. Effects resulting from the rinsing effect of solutions and the corresponding chemical reactions between Ag and chemicals can be observed. 3 different solutions — 1 M $MgSO_4$, 1 M Tris, and 0.1X PBS solutions were used in the test. The SERS spectra of adenine acquired from substrates treated with these 3 solutions are presented (Fig. 9). 100 µM adenine was measured at ~100 µW laser power with an acquisition time of 10 s. It is impossible to acquire the Raman signal of adenine in conventional Raman with such a low concentration at this laser power. However, in SERS measurements, all of 3 chemical-

treated substrates were successful in acquiring the signal of adenine. Thus, the question arises whether these solutions destruct the substrates or not?

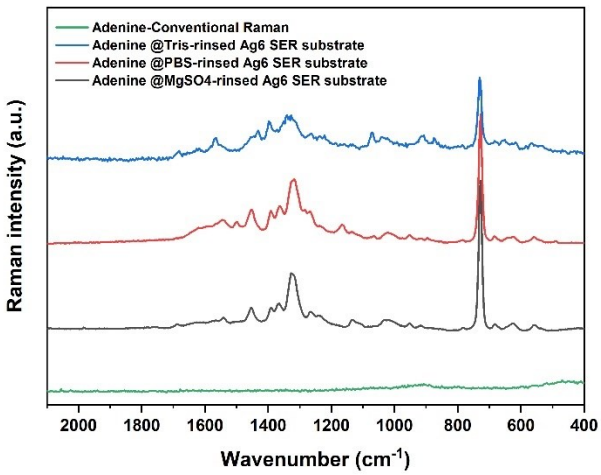

Fig. 9 Conventional Raman and SERS spectra of adenine. All 3 different chemical-treated substrates gave the spectra of 100 µM Adenine which could not be detected by conventional Raman spectroscopy.

Three substrates were incubated with 50 µL of these solutions for 20 min, respectively. Before they were measured, they were rinsed quickly with water to remove the surface salt residues. The color change of the substrates was observed (Fig. 10). Two effects contribute to this process. First, particles were rinsed by solutions, which are similar to the water-rinsed substrate (~42 nm diameter and 356 particles in $MgSO_4$-rinsed substrate and ~46 nm diameter and 332 particles in Tris-rinsed substrate). Second, these solutions reacted with Ag particles and the newly formed structures have different absorption wavelengths. Among these solutions, PBS is the most aggressive solution towards this substrate, because most of Ag particles were lost. The remaining Ag nanoparticles partly coaleced. The corresponding UV-vis spectra showed blue shifts. The maximum absorption of the PBS-rinsed substrate even shifted into the UV. These solutions show their solvent effects in this sequence: PBS>Tris>$MgSO_4$>water. Apparently, such solvent effects will weaken the enhancement amplitudes of SERS substrates. However, the strong enhancement of LSPR and the high density of Ag particles compensate the loss caused by these solutions. Thus, most of measurements can still be finished and these effects are negligible.

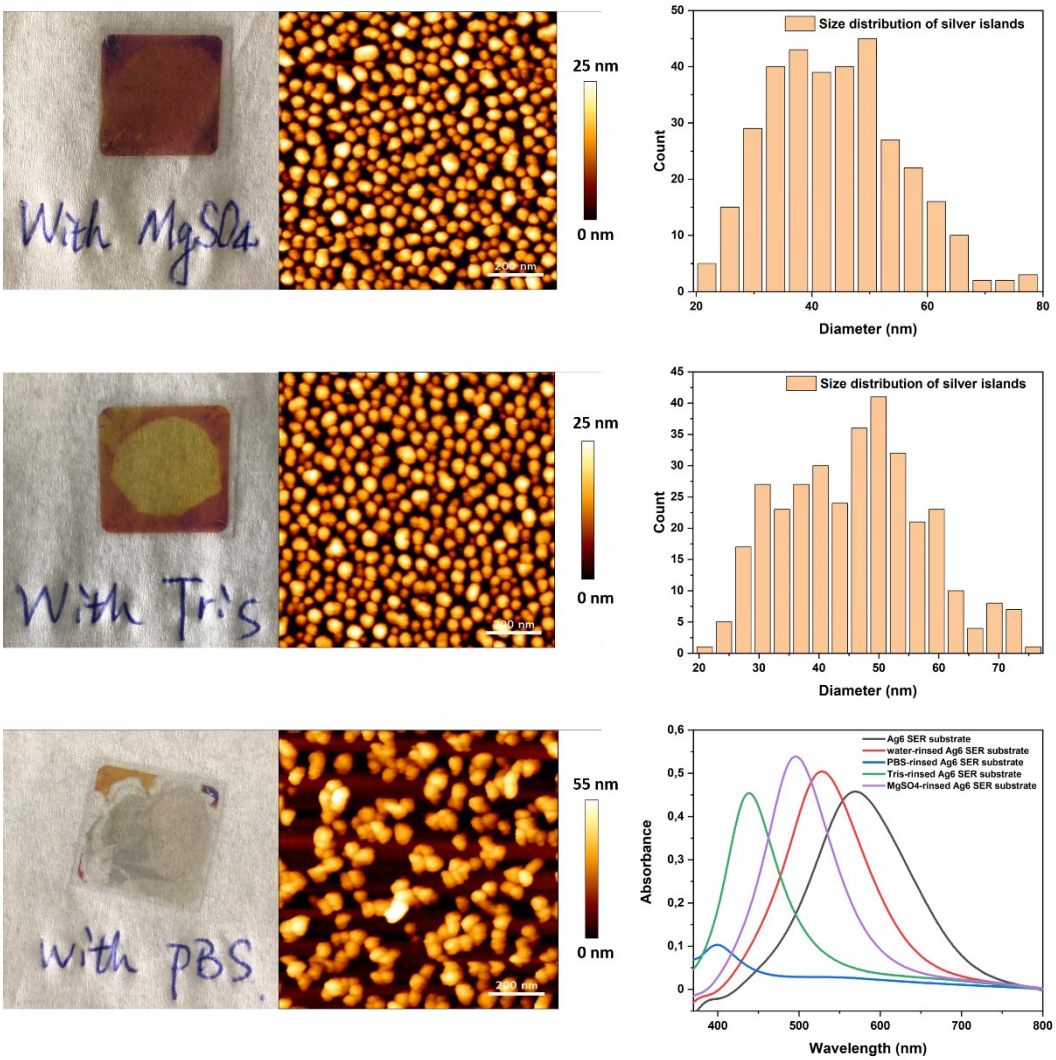

Fig. 10 Solvent effects of $MgSO_4$, Tris, and PBS solutions on Ag6 substrates. All three solutions clearly destructed these substrates which are well shown in the UV-Vis spectra.

Similarly, these solvent effects also apply to TERS tips which are prepared with the same recipe as the fabrication of SERS substrates. Fig. 11 shows the SEM images of a TERS tip, which was immersed in 1X DPBS for 1 h. Particles on the tip aggregate, showing a high level of similarity to the case of the PBS-rinsed Ag6 substrate. Tips before and after rinsing show a clear topographic variation. Ag particles were rinsed or crosslinked by solutions. Thus, the enhancement effect will be changed dramatically. This is supposed to be the main reason why AFM-TERS spectroscopy is rather limited in liquid measurements. There are two ways to avoid/minimize this issue: measuring dried samples or manufacturing liquid-resistant substrates/tips. However, as dried bio-samples are not always applicable, liquid-resistant substrates and tips are preferable.

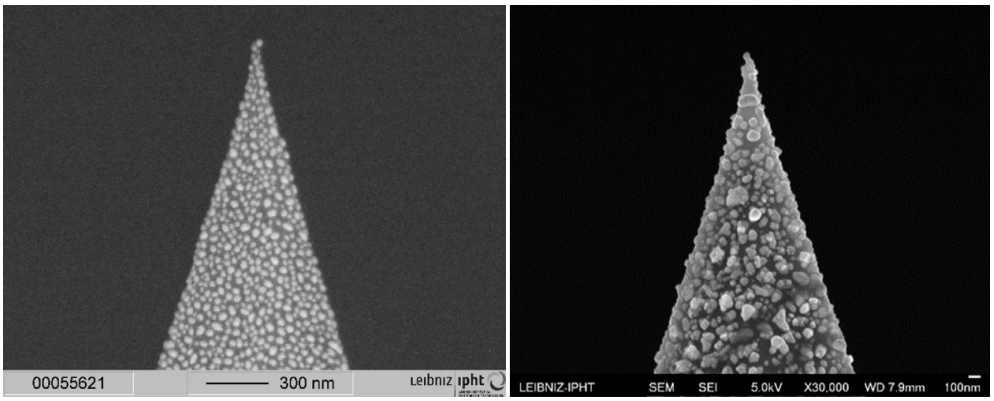

(a) (b)

Fig. 11 SEM images of Ag25 TERS tips before (a) and after (b) rinsing with PBS.

3.3 Cr-supported Ag SERS substrates for liquid measurements

Some metals, like chromium and titanium, have been found to increase the adhesion of noble metals and silica [83, 84]. Here Cr was chosen as an adhesion layer between Ag particles and the glass coverslips.

A 3 nm thick Cr film was deposited on the surface of a coverslip and then further coated with a 6 nm thick Ag film. After annealing Ag particles of ~47 nm diameters will form on the surface (averaged from 3 different random 1x1 μm^2 regions, total of 773 particles), which is the Cr3Ag6 SERS substrate (Fig. 12a). The properties of this substrate were investigated. The Cr layer (Fig. 12c) is light grey and has no absorption in the scale of visible light. However, it seems it affects the crystallization of Ag particles during the annealing process (Fig. 12b). Ag particles are much bigger compared to Ag6 substrates, and the distribution of particles is not so homogeneous. In Fig. 12b shows that the Cr3Ag6 substrate has a similar absorption wavelength to the Ag6 substrate. The solvent resistance of these substrates was subsequently tested by rinsing them with PBS and Tris. From the UV-Vis spectra a much smaller blue-shift on solution-rinsed Cr3Ag6 substrates than on Ag6 substrates (Fig. 12c) was observed. This confirms that the Cr layer does improve the adhesion of Ag particless. In the following analysis, Cr3Ag6 were used in all measurements.

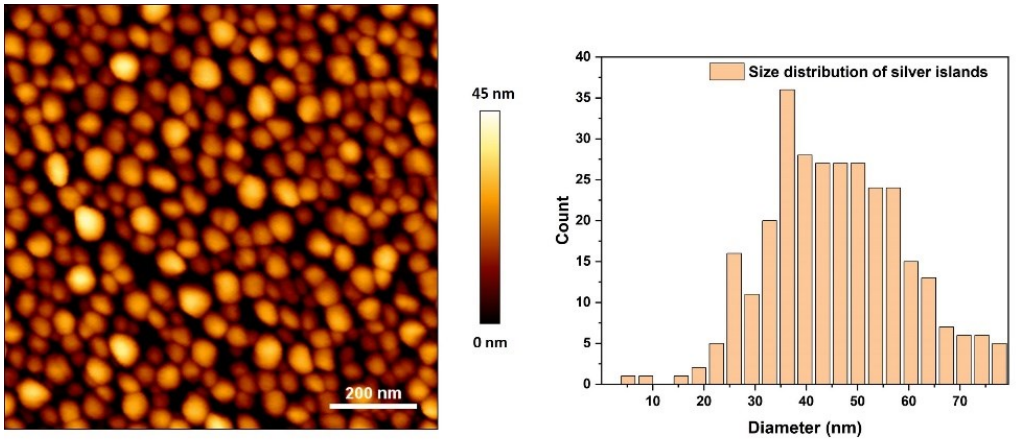

(a)

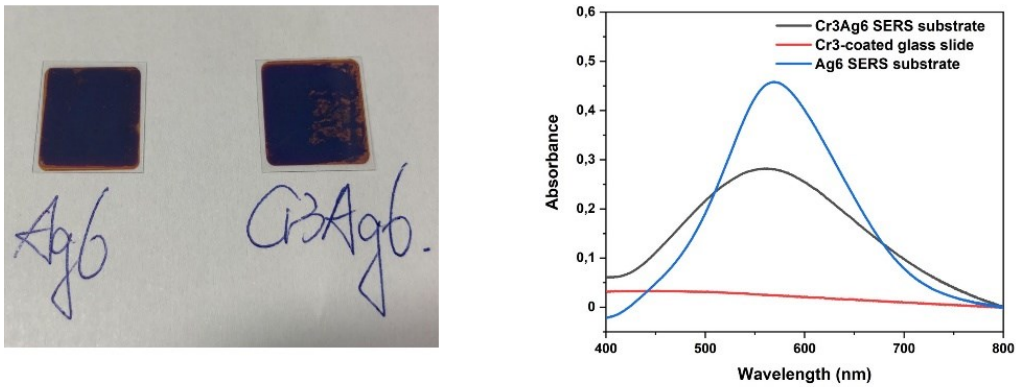

(b)

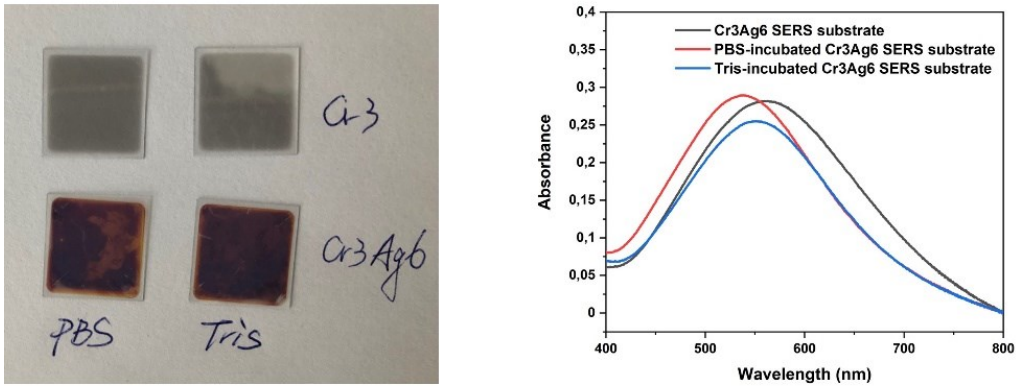

(c)

Fig. 12 Solvent effects on Cr3Ag6 substrates. (a) Topographical image of a Cr3Ag6 SERS substrate; (b) UV-Vis spectra of Cr3, Ag6 and Cr3Ag6 substrates; (c) UV-Vis spectra comparison of Cr3Ag6 substrates before and after the rinsing of PBS and Tris. The Cr layer showed no absorption at the range of 400-800 nm and it improves the adhesion of silver partilces on the substrates.

3.4 Iodide suppresses degradation of peptides in SERS measurements

3.4.1 Sample degradation in SERS measurements

The SERS spectra of 140 µM dCaL in liquid for an exposure time of 1 s (300 accumulations) and different powers from 0.8 µW to 1 mW are presented in Fig. 13. With increasing power, two broad carbonaceous peaks at ~1350 cm^{-1} and ~1570 cm^{-1} appear, which are the characteristic for sample degradation. From this figure it is obvious that sample degradation can happen at almost any power. Lower powers may reduce the risk of sample degradation at the cost of the SNR.

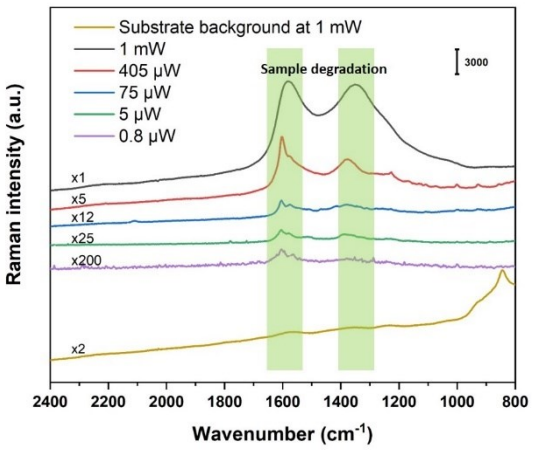

Fig. 13 SERS spectra of dCaL measured in liquid at different powers. The two bands at 1350 and 1570 cm^{-1} present the effect of sample degradation on the substrate.

Sample degradation, which is usually assumed to be the result of local overheating caused by LSPR, is a common phenomenon in enhanced Raman measurements[85, 86]. Some researchers mention that the local temperature can increase by tens of degrees or even higher[44, 45, 87]. The thermal effect induced by LSPR can change the structure of the sample by destroying hydrogen bonds and other covalent bonds, e.g. thermal denaturation can change the structures of proteins like quaternary and tertiary structures[88]. Another common example where heating plays a major role: 95 °C is a common temperature used to open the double helix of DNA in a polymerase chain reaction (PCR)[89]. It is remarkable how physical and/or chemical ways can cause sample degradation to such an extent in a short exposure time of a few seconds like in the cases depicted in Fig. 13. Consequently, overcoming sample degradation becomes a very important and urgent topic.

3.4.2 Photocatalysis-induced sample degradation on Ag SERS substrates

Apart from the thermal effect and the enhanced EM field, hot carriers could be also excited upon the plasmonic nanoparticles used, followed by the transfer and interaction with the adsorbates around these particles. This process is called photocatalysis (see Fig. 14). The above-mentioned effects are employed in different fields, including photothermal therapy[90], Raman spectroscopy[38], and photocatalysis[91, 92], respectively. In an enhanced Raman measurement, thermal effects and hot carriers-driven photocatalysis are side effects and should be avoided. However, compared to the photothermal effect, photocatalysis does not get enough attention, for two main reasons. First, the lifetime of these hot carries is extremely short; it is in the scale of fs-µs. Second, photoreactions can only be triggered when these hot carriers have orbital/energy overlap with the absorbates. Without a suitable condition, the energy of these carries will dissipate e.g. by self-recombination (Fig. 15a). Hence, the photocatalytic effect is limited.

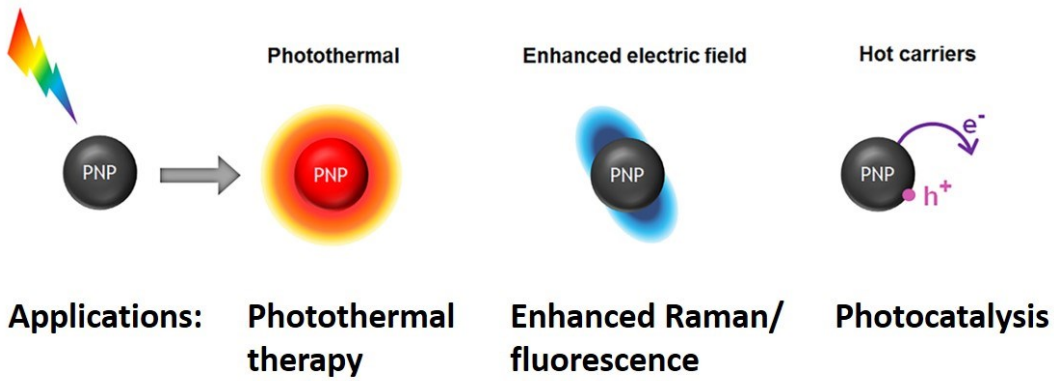

Fig. 14 Three different effects deriving from LSPR of plasmonic nanoparticles (PNP) and their applications(Adapted from Ref. [86]).

As surface active material a Ag_2O layer is present on the Ag particle surface. Ag_2O is semiconductor with a narrow bandgap (~1.2-1.3 eV)[93, 94] and a good NIR-visible photocatalyst. It can be excited by a 1000 nm NIR light. Ag_2O is generally photosensitive and unstable[95]. The photogenerated electrons and holes will prefer to interact with Ag_2O itself, generating Ag and O_2, respectively (Fig. 15b). Thus, the photocatalytic effect of an independent Ag_2O is often ignored. Interestingly, when Ag_2O forms upon Ag nanoparticles, they will merge into a stable heterojunction (abreviated as Ag_2O@Ag)[93]. A charge separation extends the lifetime of hot carriers on such a structure. Theoretically, Ag_2O nanoparticles help the charge transfer of hot electrons from Ag, where these electrons will further interact with O_2 forming into

peroxide radicals ($^{\bullet}O_2^-$). Accordingly, the photogenerated holes will be available for interaction with water, forming into hydroxyl radicals ($OH^{\bullet}$). These reactive species induced by the photocatalysis have been verified to cause the photodegradation of samples (Fig. 15c)[96]. In other words, it is highly likely that the photocatalytic effect of Ag_2O/Ag structures on SERS substrates contributes to sample degradation. To verify this, ESR experiments were used to detect the dominant reactive species.

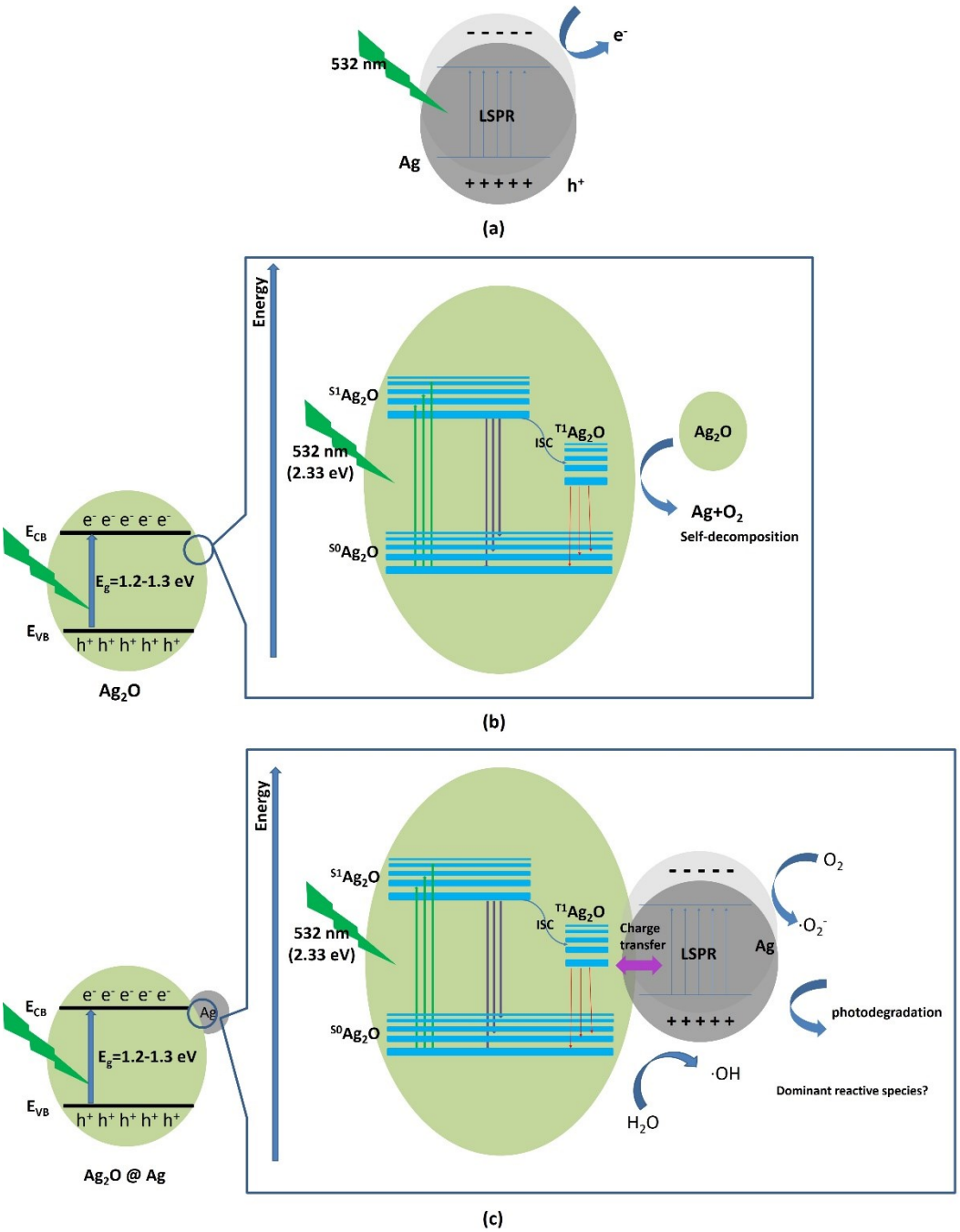

Fig. 15 Photocatalytic mechanisms of Ag, Ag_2O and Ag_2O@Ag. (a) Hot carriers induced by LSPR. (b) Self-decomposition of Ag_2O. (C) Photodegradation induced on a stable Ag_2O/Ag heterostrucutre. The dominant reactive species involved into the degradation process should be analysed.

ESR is a powerful instrument to detect unpaired free electrons[97]. Every kind of radical has its characteristic ESR spectrum. In a photocatalytic process, $^{\bullet}O_2^-$, $OH^{\bullet}$ and h^+ are the most common and original reactive species which are powerful enough to degrade samples. Concerning the low density and short lifetime of reactive species, a spin trap 5-tert-Butoxycarbonyl-5-methyl-1-pyrroline-N-oxide (BMPO), which can catch radicals and form more stable adducts, was introduced in the measurements. BMPO-radical adducts have a half-lifetime reaching up to 23 min. To suppress the strong absorption of water in ESR, measurements were conducted at a low temperature (77 K-90 K) using liquid nitrogen.

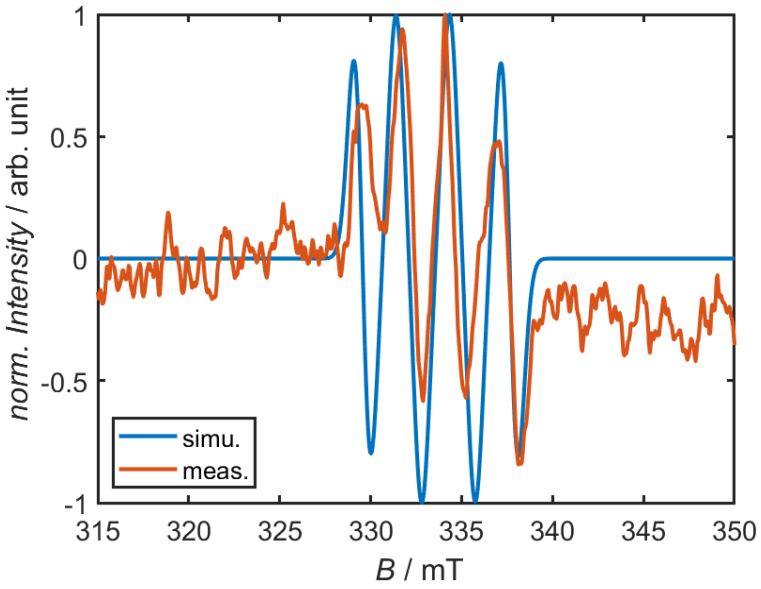

Fig. 16 ESR spectrum of a BMPO-radical adduct from a Cr3Ag6 substrate.

To ensure that the observed radical is caused by the SERS substrate, the experiment was repeated without the SERS substrate, in which a different spectrum with much lower intensity was observed. As both spectra were recorded under identical conditions, the spectrum of the SERS triggered product is the deviating spectrum of these two experiments (see Fig. 16). The resulting ESR spectrum shows four lines, which could be simulated for a S = 1/2 system with hyperfine interactions to one nitrogen and one hydrogen nuclear spin, which is typical for BMPO trapped radicals. The simulated spectrum (g = 2, A_N = 82 MHz, A_H = 62 MHz, l_{wpp} = 0.95 mT) confirms that a radical is trapped by BMPO. Unfortunately, the observed hyperfine coupling constants are larger than the reported values for trapped peroxide or hydroxyl radicals, which are in the range from 26 MHz to 38 MHz at room temperature[98]. Thus, it is speculated that this BMPO adduct may be a direct reaction product of electrons or holes with BMPO itself. As for the quite weak signal and the different hyperfine constants it is not possible to identify the primary radical formed by the SERS substrate. Nevertheless, these radicals originate from the irradiation of the SERS substrate. When

the irradiation was external and the supernatant solution with BMPO was measured afterwards, the same spectrum but with lower intensity was observed. The decreasing signal intensity might be caused by the limited stability of the formed trapped radicals and the extreme low density of silver particles on the detected substrate. All experiments without BMPO as spin trap were ESR silent and no radicals could be observed. In a laser radiated sample (532 nm), the same radicals were also detected. Thus, radicals exist during SERS measurements and consequently could be responsible for sample degradation.

3.4.3 Iodide suppresses sample degradation

Both thermal effect and photocatalysis are adverse effects for any SERS experiment. Accordingly, the suppression of potentially occurring photocatalysis due to Ag_2O@Ag may be helpful to address the issue of sample degradation. Two strategies can be implemented to suppress photocatalysis. One way would be to change the light wavelength. Once the photon energy is lower than the band gap of a photocatalyst, its photocatalytic activity will be inhibited. However, considering the NIR activity of Ag_2O, this strategy is not suitable as the required plasmon enhancement could not be used anymore. Another approach is to introduce radical scavengers, which are often used to quench radicals from photocatalysis[99]. They can be commonly divided into organic and inorganic groups. Taking the influence of organic matters on Raman measurements into account, inorganic scavengers are preferred.

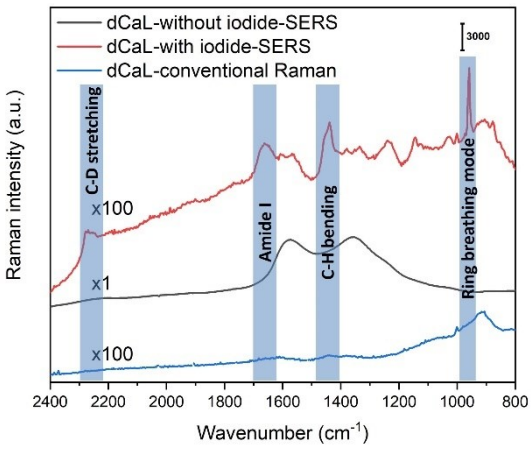

Fig. 17 SERS spectra of dCaL with and without iodide treatment. After the injection of iodide, sample degradation was suppressed. The blue clolumns show the characterized bands of dCaL.

As what we have known, this is the first time that iodide is found to adequately suppress sample degradation in SERS measurements (Fig. 17). In this experiment, a fungal peptide dCaL was chosen as the model sample (For more detailed about dCaL,

please check Chapter 4). Adding iodide into dCaL solution with the respective final concentration of 5 mM and 140 µM, SERS spectrum of dCaL was acquired with 1 mW laser power and 1 s exposure time (300 accumulations). More importantly, the features of sample degradation completely disappear when compared to the control spectrum without iodide treatment. The four characteristic bands of dCaL at around 2285 cm^{-1}, 1660 cm^{-1}, 1440 cm^{-1} and 960 cm^{-1} are all obtained. These bands are assigned to C-D stretching, amide I, C-H bending, and deuterated ring breathing mode, respectively. These results suggest that iodide can effectively suppress sample degradation. As iodide would not change the temperature of the system, compared to a local thermal-induced degradation, the hypothetical degradation mechanism induced by photocatalysis is more reasonable.

Based on the results two properties of iodide are responsible for sample degradation suppression. First, iodide can interact with Ag_2O; once iodide solution is added to an Ag SERS substrate iodide will quickly interact with Ag_2O, which is then altered into AgI. This was analyzed and confirmed in XPS and XRD measurements. In Fig. 18, the two XPS peaks of iodine at 630.4 eV and 619.0 eV confirm the existence of iodide on the surface of the Ag SERS substrate. The complex fitting peaks in oxygen and carbon show multiple origins of these elements. For example, oxygen can originate from Ag_2O, silica, or even organic pollutants.

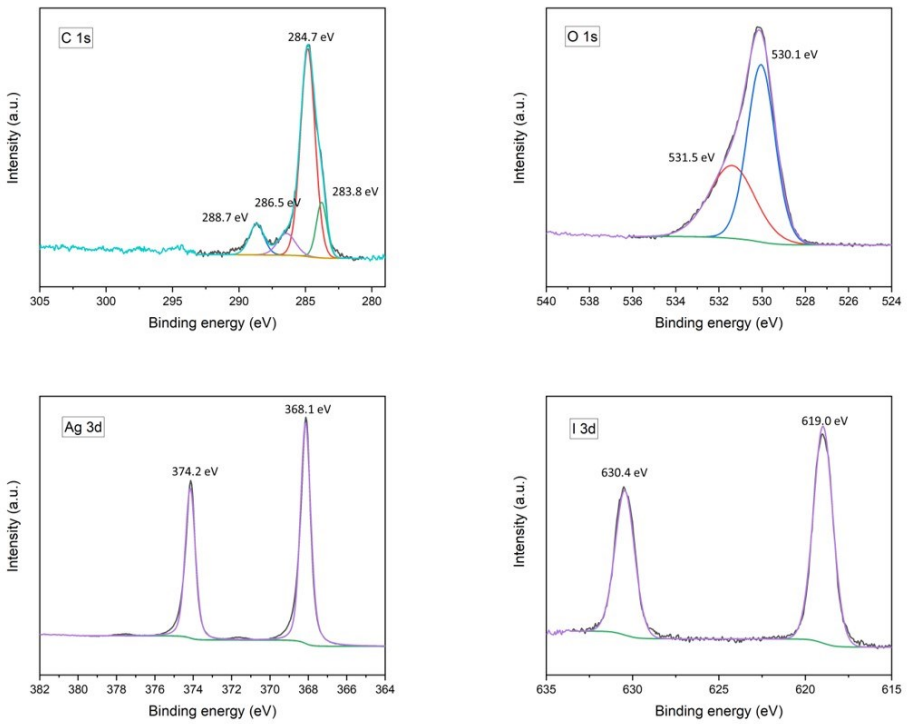

Fig. 18 XPS spectra of elements C, O, Ag and I from an iodide-treated Cr3Ag6 substrate.

In Fig. 19 the XRD spectrum shows that AgI is in a hexagonal crystal phase, whereas Ag particles are in cubic phases. This indicates that iodide actually reacts with Ag_2O forming into AgI. Interestingly, Ag_2O is undetectable in XRD, which suggests that it is in amorphous phase. AgI (2.56 eV)[100] has a much broader bandgap than Ag_2O (1.2-1.3 eV), which cannot be excited by a 532 nm laser (2.33 eV). Thus, the photocatalytic process from Ag_2O should be stopped by the replacement with AgI.

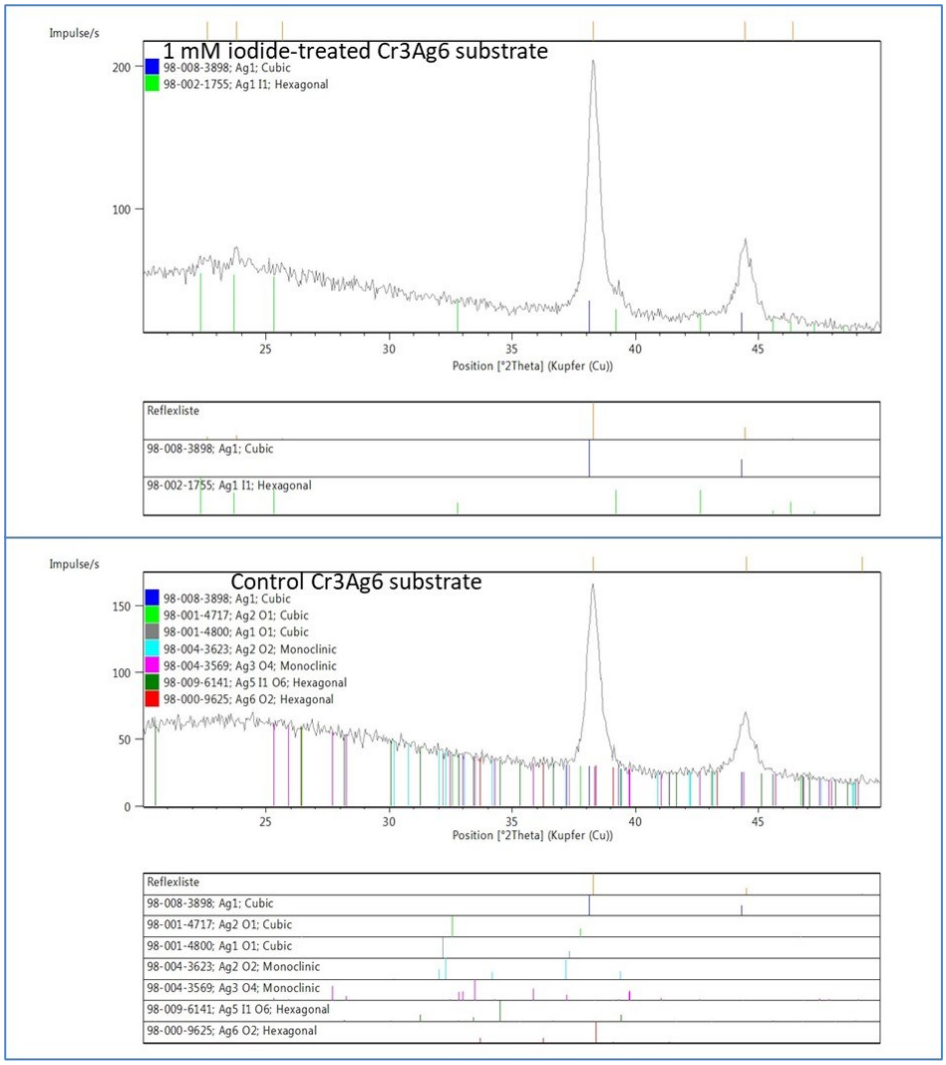

Fig. 19 XRD spectra of iodide-treated SERS substrates. Ag is in a cubic phase while AgI is in a hexagonal phase and Ag_2O is undetectable.

Nevertheless, the photocatalysis from plasmonic Ag nanoparticles still exists when the heterojunction of Ag_2O@Ag is converted into AgI@Ag. Even though the efficiency decreases, AgI itself may still help the charge transfer from Ag. Thus, besides the replacement of Ag_2O, it is suggested that excess iodide ions also function as radical scavengers, which is why it is often used as a food antioxidant[101]. From Akel's work[102], it is calculated that the potential (vs. NHE at pH7) of the conduction band and the

valence band of Ag_2O are ~+0.3 V and ~+ 1.5-1.6 V, respectively, which is not enough to oxidize OH^- to $OH^\bullet$ (+2.31 V)[103]. In contrast, the potential of I^-/IO_3^- is 1.09V vs NHE at pH0[104]. With the increasing of pH value, this potential will decrease. In other words, at pH7, the potential will be smaller than 1.09 V and holes from Ag_2O@Ag could easily oxidize iodide to iodate.

$$I^- + 6h^+ + 6OH^- \rightarrow IO_3^- + 3H_2O$$

By this process, the sample degradation induced by holes is suppressed. Moreover, Ag_2O is a p-type semiconductor in which holes are the dominant reactive species[105]. Thus, the donation from electrons could be ignored.

The contribution of these two iodide properties was further experimentally checked. Fig. 20 is the SERS spectra of dCaL acquired from an iodide pre-treated SERS substrate under 1 mW laser and 1 s exposure time (300 accumulations) with and without excess iodide solution. In this experiment, 2 µL 140 µM dCaL solution was firstly added on the iodide pre-treated substrate. The spectrum showed that without excess iodide no apparent signal from dCaL was acquired. Both the characteristic bands from C-D and deuterated ring disappeared. After the adding of 0.5 µL 50 mM iodide solution (final concentration of iodide, 10 mM) into the dCaL sample (final concentration of dCaL, 110 µM), the genuine spectrum of dCaL appeared. This verifies the theory that excess iodide plays an important role in the suppression of sample degradation. Additionally, the same spectra could be obtained no matter iodide is injected on the substrate or samples are injected first. Considering the reaction time between iodide and Ag nanoparticle, free iodide should dominate the suppression of sample degradation.

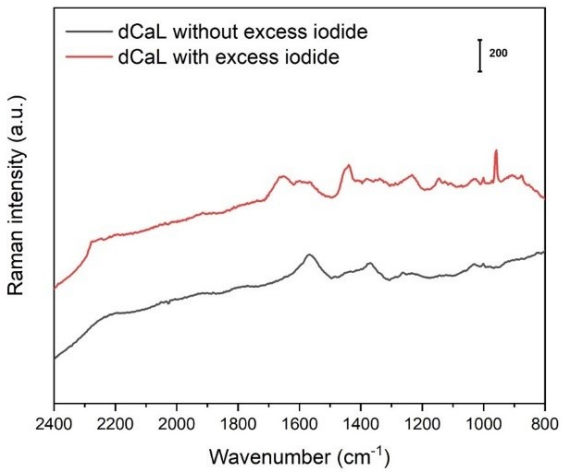

Fig. 20 SERS spectra of dCaL with and without excess iodides on an iodide pre-treated SERS substrate. Without the help of excess iodides, the spectrum of dCaL could not be obtained.

Above-mentioned experiments in Chapter 3.4.3 try to give a subsidiary explanation for the sample degradation in SERS measurements. First, when Ag contacts with Ag_2O or AgI forming a heterojunction (Ag_2O@Ag or AgI@Ag), typically, the local physical property will change. According to the observed sample degradation it is supposed that a barrier, which has a rectifying nature, forms onto this. Such a barrier will support the charge transfer between the two materials. Concerning Ag_2O is a p-type semiconductor, it is speculated that holes dominate the sample degradation on SERS substrates. Second, Ag_2O@Ag is a plasmon-assisted photocatalyst, which differs from a traditional photocatalyst. Ag_2O and Ag simultaneously act as photocatalyst and promote charge separation. It is essential to explore the LSPR effect on Ag nanoparticles in Ag_2O@Ag.

Fig. 21 explains a possible mechanism of iodide treatment. After the replacement of Ag_2O by AgI, the original photocatalysis in Ag_2O@Ag is weakened. Currently, the donation of AgI like charge separation in this structure is still under investigations. However, there is no doubt that the excess iodides further interact with the reactive species and dominate the suppression of sample degradation. Moreover, iodide will also make the surface charge negative which may help positively charged molecules to move closer to plasmonic Ag nanoparticles and, thereby, improve the reproducibility of SERS measurements. Currently, more investigations of the exact performance of Ag_2O@Ag are in progress.

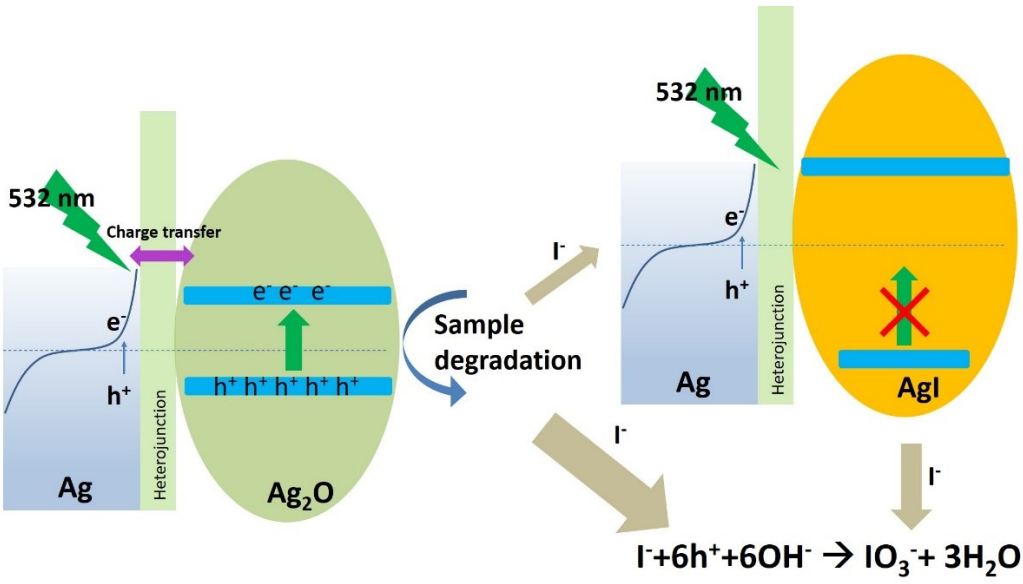

Fig. 21 Possible mechanism of iodide-treatment on Ag SERS substrates. The replacement of Ag_2O into AgI will weaken the original photocatalysis from Ag_2O while it is speculated that free iodide acts more in the suppression of sample degradation.

3.5 SERS measurements with high reproducibilites

In order to assign an enhanced Raman spectrum its corresponding conventional Raman spectrum is very important. There are already many works[38] mentioning that some bands disappear or shift, while others are newly formed in enhanced Raman spectra. While many of these effects can be attributed to specific sample surface interactions (surface bonds, surface diffusion, single or “few” molecule effects) these variations can often be a nuisance if a straightforward sample analysis is required. Conventional Raman spectroscopy is this respect, is reliable and has longer history of experimental investigations than enhanced Raman spectroscopy. Many chemical bands have been adequately assigned and are agreed upon by researchers. Therefore, for a new sample, it would be better to carry out conventional Raman measurements before moving on to SERS and TERS measurements.

In addition to the suppression of sample degradation, iodide also improves the reproducibility of SERS measurements. In fact, one of the reasons for low reproducibility of Ag SERS substrates is sample degradation. This is also asserted by Ren’s group who used iodide-treated colloidal Ag for measurements of proteins [106]. The fragments of degraded samples, especially intermediate products, will result in different Raman spectra. Iodide suppresses sample degradation and converts the surface charge of the substrate to negative. Thus, positively charged samples can easily approach the surface of Ag particles, whereby signals from more chemical bonds can be acquired.

Fig. 22a shows the comparison of SERS spectra of 120 µM dCaL with 8 mM iodide acquired from 1 accumulation to 300 accumulations (averaged) with 1 s exposure time at 1 mW laser power. These spectra reveal an extremely high similarity to each other, which means that this method provides a high reproducibility. Without an iodide treatment such a large accumulation is almost impossible in SERS measurements. The number of accumulations depends on the experimental requirements. In this dCaL-related experiment it is found that 100 accumulations provide a sufficient SNR. Moreover, the iodide method could be used to detect a concentration of dCaL down to 1.4 µM.

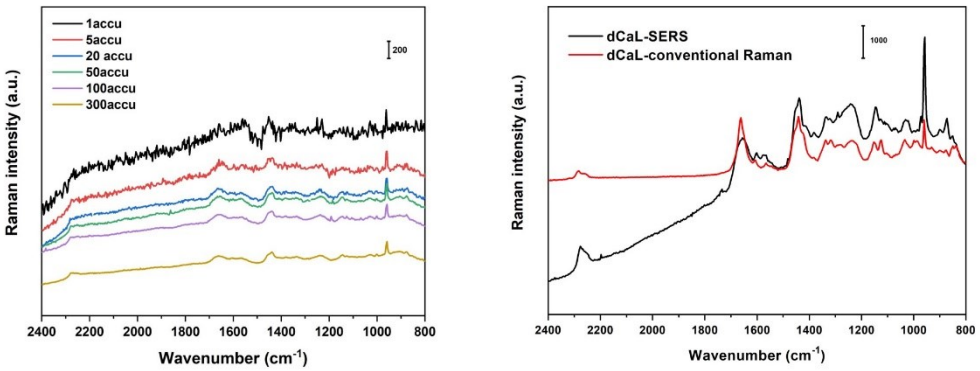

Fig. 22 (a) Strong reproducibility of SERS measurements with iodide-treatment and (b) comparison of conventional Raman and SERS spectra of dCaL

Fig. 22b is a comparison of conventional Raman and SERS spectra of dCaL. The conventional Raman spectrum was acquired from 10 µL 1.4 mM dCaL dried onto a glass slide with a background correction under 14.8 mW laser power and 10 s exposure time (10 accumulations), while the SER spectrum was acquired from 120 µM dCaL with 8 mM iodide under 25 µW laser power and 1 s exposure time (300 accumulations). No background subtraction was performed for the SERS spectrum. It is clearly shown that most of the bands obtained by conventional Raman and SERS spectra match each other adequately. Some bands disappear in the SERS spectrum, but the minor differences do not affect the assignment. There is a stronger photoluminescent background in the SERS spectrum compared to the conventional Raman spectrum. This is a side-effect which may be introduced by iodide-crosslinked Ag particles. In several tests the same spectrum of dCaL was obtained. As a result, this method could help to improve the reproducibility of SERS. To check the adaptability, a peptide extracted from bee venom called Melittin was also investigated (see Fig. 23). The conventional Raman spectrum of Melittin was acquired from 1.4 mM Melittin under 10 mW laser power and 1 s exposure time (100 accumulations) while the SERS spectrum was acquired from 140 µM Melittin with 5 mM KI treatment under 1 mW laser and 1 s exposure time (100 accumulations). These two spectra also show a high similarity, which confirms the reliability of iodide treatment and this SERS substrate. As the spectrum of Melittin is clearly different from dCaL, it is confirmed that this is a genuine spectrum from the corresponding sample. Furthermore, the different spectra of Melittin and Candidalysin confirm the iodide method is reliable. Currently, this method is only used for biosamples. A detailed research of its selectivity is still in progress.

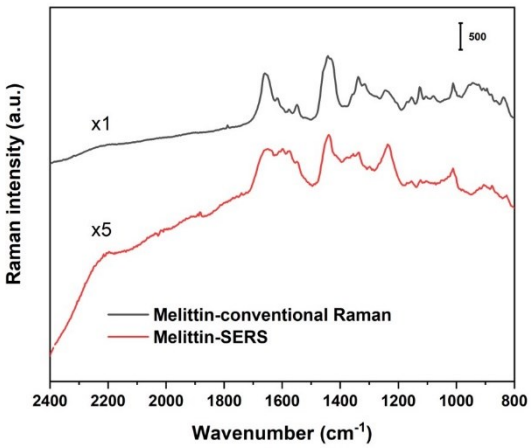

Fig. 23 Conventional Raman and SERS spectra of Melittin. The high similarity of the spectra verifies the generality of the iodide method.

3.6 Chapter summary

In this chapter, concerning the application of glass-supported SERS substrates, two issues including the short lifetime in liquid and sample degradation of SERS measurements were addressed.

First, Ag SERS substrates are found to be easily destructed by salt solutions, which will decrease the enhancement and shorten the lifetime of SERS substrates. With the comparison of four solutions — dH_2O, $MgSO_4$, Tris and PBS — it is confirmed that the chemical reaction between Ag and solutes in solution will apparently destruct the structures of SERS substrates. In SERS measurements of biosamples, buffers with aggressive chemicals like PBS should be avoided. It can be suggested that this is the main reason of AFM-TERS spectroscopy's limit in liquid measurements. A Cr coating method has proven to be helpful to increase adhesion of Ag nanoparticles to substrates.

The second and more serious issue in SERS measurements is sample degradation, which is accompanied by the challenge of low reproducibility. Apart from the thermal effect induced by LSPR, it is suggested that a strong photocatalysis originating from Ag_2O@Ag structures also contributes to sample degradation. For the first time, iodide is found to suppress sample degradation by the replacement of Ag_2O and the reaction with reactive species, whereof the latter is predominant. Additionally, iodide apparently improves the reproducibility of SERS measurements. As these are very early experiments on only two different samples, more detailed investigations have to be

carried out. With regard to the blinking effect in SERS spectra, conventional Raman measurements are always suggested in order to facilitate the spectrum assignment of a new material. To weigh the difference between the thermal effect and photocatalysis induced by LSPR, a simulation of the local temperatures of SERS substrates will be conducted. The verificiation of the hypothesized mechanism of iodide is also in progress.

Briefly, Cr coating is verified to validly extend the durability of Ag SERS substrates in liquid measurements. Moreover, sample degradation of Ag SERS substrates is found to be suppressed by iodide. These experiments improve the bioapplications of enhanced Raman spectroscopy.

4. Investigations of Candidalysin using time-lapse AFM and TERS spectroscopy

4.1 Candidalysin

Candida albicans is responsible for a number of mucosal infections. Fungal infections are a serious issue, being responsible for more deaths worldwide than malaria and tuberculosis[107, 108]. Statistically, the number of life-threatening infections with *Candida* spp. is over 400,000 per year. The mortality rate of candidiasis reaches up to 46-75%[109]. Even though being one of the most frequent nosocomial fungi, Candida infections are difficult to cure and cause high morbidity and mortality. To this day, valid and efficient therapies are not available. Currently, the overall virulence factor of *Candida albicans* is basically understood. As an opportunistic human fungus, *Candida albicans* is commonly found on skin and mouth as a harmless commensal yeast state. Once a patient is immunocompromised, these fungi will get the opportunity to switch from the yeast state to a pathogenic hypha state, which invades cells, blood vessel, and other organs and then causes harmful diseases (Fig. 24a).

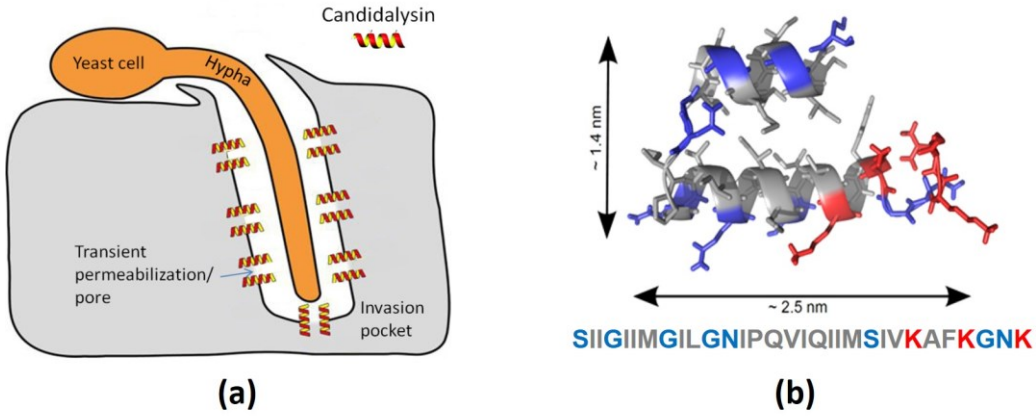

Fig. 24 (a) Schematic diagram of the penetration of CaL upon cell membrane and (b) 3D structural model and amino acid sequence of CaL (courteously provided by Prof. Dr. Thomas Gutsmann).

Recently, Candidalysin (CaL), a small helical peptide with 31 amino acids, was separated from *Candida albicans* and recognized by our collaborators as a key peptide toxin during the penetration of the fungus[110]. Fig. 24b shows its structural 3D model. The discovery of CaL provides a better understanding of the infection process and further cell response, which has proven to be critical for mucosal and systemic infections and is a key driver of host cell activation, neutrophil recruitment, and Type

17 immunity[111]. Evidence shows that, concomitant to its virulence, CaL also acts as an immunomodulatory molecule, which initiates a protective response[112, 113]. Therefore, the detailed effect of CaL on human cells, especially on cell membranes, is worth investigating.

At present, most investigations are pursued from the angle of clinical therapy, pathology, and microbiology. However, one of the most important modes of action of the fungal infection — the effect of CaL on the human lipid membrane — is still unclear from a biochemical perspective. Moyes *et al.*[110] proposed that CaL has a mode of action similar to antimicrobial peptides which mainly induce pore formations on the cell's lipid membrane. In this chapter, the first findings on the interaction of CaL with the lipid membrane at the nanoscale using AFM are presented. The chemical information of CaL is investigated in advance using Raman spectroscopy. It is expected that this work will help researchers understand the behavior of CaL in association with lipid membranes and will further promote the development of better prevention and therapy for candidiasis.

4.2 Experiments

Preparation of mica-supported artificial lipid bilayer membrane

An artificial lipid membrane composed of 1,2-dioleoyl-sn-glycero-3-phosphocholine (DOPC) and 1,2-dipalmitoyl-sn-glycero-3-phosphocholine (DPPC) was prepared. DOPC and DPPC were mixed in a ratio of 1:1 to achieve a final concentration of 3 mM. The mixture was dissolved in chloroform:methanol (3:1, v:v) solution. To prepare supported lipid bilayers (SLBs), 100 µL DOPC/DPPC mixture were firstly dried in a small glass vessel with Ar and then redissolved in 600 µL buffer (150 mM KCl, 20 mM Tris and 25 mM $MgCl_2$, pH=7.4). This solution was then heated up to ~70 °C and agitated 5 cycles (1 min agitation and 20 s re-heating per time). To get unilamellar liposomes, the solution was then sonicated for 30 min. Subsequently, 200 µL lipid solution was incubated on a freshly cleaved mica disc for 30 min and then rinsed with equal volumes of buffer for 3 times. Lipid bilayers then formed on the mica surface. To keep the membranes intact, SLB samples always have to be kept in buffer. (This protocol is provided by Dr. Lorena Redondo-Morata, France.)

Cell culturing and treatments with dCaL

All of the cell samples were provided by the group of our project collaborator Prof. Dr. Bernhard Hube from the Hans-Knöll-Institute (HKI), Jena. TR146 cells were used and seeded onto WillCo dishes, which are made with round glass bases in the center and

can be used for Raman measurements. The number of cells was around ~1-3x10^5 cells per well with 1 mL solution. The passage number (a biological term refers to cell culture) of cells changed with every batch, but the conditions met the requirements. The cells were cultured on dishes for two days and then washed with DMEM/F12-FBS solution. Subsequently, the cells were incubated with 6 µM dCaL for 3 h in a CO_2 incubator at 37 °C and 5 % CO_2. After that, they were washed with pure water 2 times and fixed using 1 mL of 4 % Histofix under 37 °C for 30 min. Finally, the cells were rinsed with pure water 2 times and kept with 1 mL of water in each well. Such samples can normally be stored in the fridge at 4 °C for 1 month without degradation. Control cells were prepared following the same protocol but without the infection step of deuterated CaL (dCaL). Fig. 25 shows the morphological difference between control cells and dCaL-infected cells. The control cells remained intact, whereas dCaL-treated samples were broken.

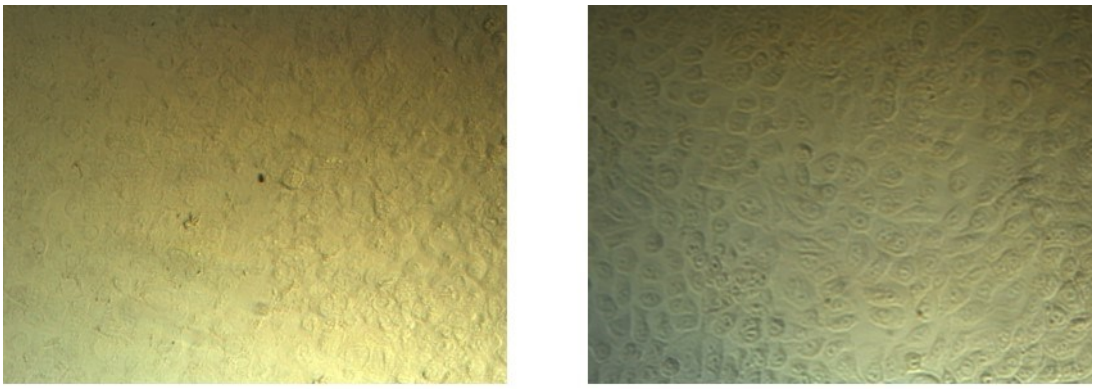

Fig. 25 Conventional optical microscope images of cells treated with (a) and without (b) dCaL

AFM measurements

i. Time-Lapse AFM

For AFM imaging the PNP-TR AFM tips were used. These are 2-cantilever AFM tips on which the short cantilever was chosen. The imaging mode was set to tapping mode and the images were acquired at 512x512 pixels. Before injecting CaL, an equilibrium scan was performed in each experiment, which varied from 30 min to 1 h. According to the different experiments, 0.2-2.5 µM CaL were injected into solutions containing SLBs. AFM was started as soon as CaL was added, and it was stopped only when there were no more visible topographical changes on the SLBs.

ii. Cell imaging

For the imaging of cell samples contact mode was used, in which forces were set below 0.2 nN to avoid tip damage on cell samples. The AFM tips in this step were CSG30 (for cells in liquid) and NSG10 (for cells in air).

Conventional Raman, SERS and, TERS measurements

The preparation of SERS substrates was already mentioned in Chapter 3. Except for a 25 nm Ag coating, the manufacturing of TERS tips follows the same steps as those of SERS substrates. For Raman measurements, coverslips were cleaned with piranha solutions (HNO_3:H_2O_2, v:v=3:1). Both conventional Raman and SERS spectra of lipids (DOPC/DPPC) and CaL/dCaL were acquired. A 532 nm laser was used as light source. The conventional Raman data were acquired with a laser power of 10-15 mW while in SERS and TERS measurements the laser power was lowered to 100-1000 µW. Conventional Raman spectra were obtained with an exposure time of 10 s with 10 accumulations, while SERS spectra were acquired with an exposure time of 1 s and 60-300 accumulations. TERS spectra were acquired with 1-3 s and 1 accumulation. 500 µM lipids and 6-140 µM CaL/dCaL were measured. 1-50 mM KI were used to suppress sample degradation in enhanced Raman spectroscopy measurements.

Data analysis

AFM images were evaluated by JPKSPM Data Processing software and Gwyddion, including data leveling, horizontal scar correction, area calculation, etc. Raman data were processed with Origin (8.0 and Pro 2020b). Due to low sample concentrations, some conventional Raman data were background-corrected which will be indicated in corresponding descriptions of the experiments. There were no background corrections done for enhanced Raman spectra and spikes were removed.

4.3 CaL-induced structural variation of artificial lipid membranes

4.3.1 Topographical basis of artificial lipid membranes

In the human body, the cell membrane forms the barrier protecting the cell from the extracellular medium, carrying the tasks of substance exchange, signal transmission, and protection of cells from environmental influences and other intruders. Cell membranes mainly consist of lipid bilayers, sugars, and proteins (Fig. 26), whereof the lipids build the skeleton of the cell membrane. The proportion of lipids in cell membranes reaches ~40%. The lipid membrane consists of a group of lipids: phospholipids, glycolipids, and cholesterol, of which phospholipids are the most abundant[114]. Artificial lipid bilayers are often used to mimic the structure and function of the cell lipid membranes. In this work, two common phospholipids, DOPC and DPPC, were used.

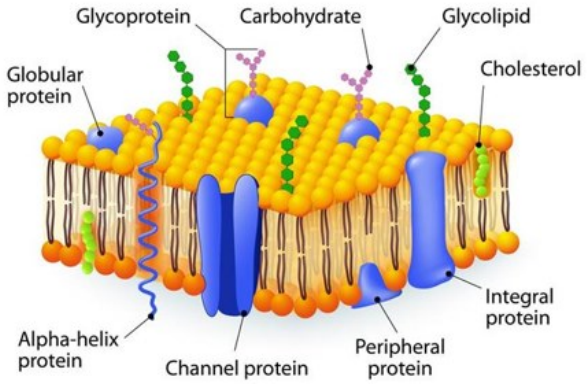

Fig. 26 Cell membrane model (adapted from biologywise.com)

DOPC and DPPC have a very similar structural formula, which is basically composed of a phosphocholine head and two hydrocarbon chains (Fig. 27a). Once they form lipid bilayers in solutions, the hydrophilic phosphocholine (PC) head positions itself towards the environment while the hydrophobic hydrocarbon chain will point towards the middle of the membrane (Fig. 27b). The main difference of DOPC and DPPC is the double bond of hydrocarbon chains. DOPC has two double bonds on each chain while the hydrocarbon chains of DPPC are saturated. Affected by the number of double bonds and the length of the hydrocarbon tails, these lipids have different transition temperatures. The phase transition temperature of DOPC is only -17 °C while DPPC's is 41°C. Thus, under ambient conditions, DOPC is in a liquid-crystalline (abbreviated to 'liquid' in the following descriptions) phase while DPPC is in a gel phase. In an AFM image, the greatest difference between them is marked by their heights. Fig. 27c is an AFM image of DOPC/DPPC membranes on which DOPC, DPPC, and mica can be distinguished. The heights of bilayer DOPC and DPPC are ~4.5 nm and ~6 nm, respectively (Fig. 27d). Their height difference is, thus, ~1.5 nm. By measuring the topographical information of membranes, the mode of action of CaL on lipid membranes can be revealed.

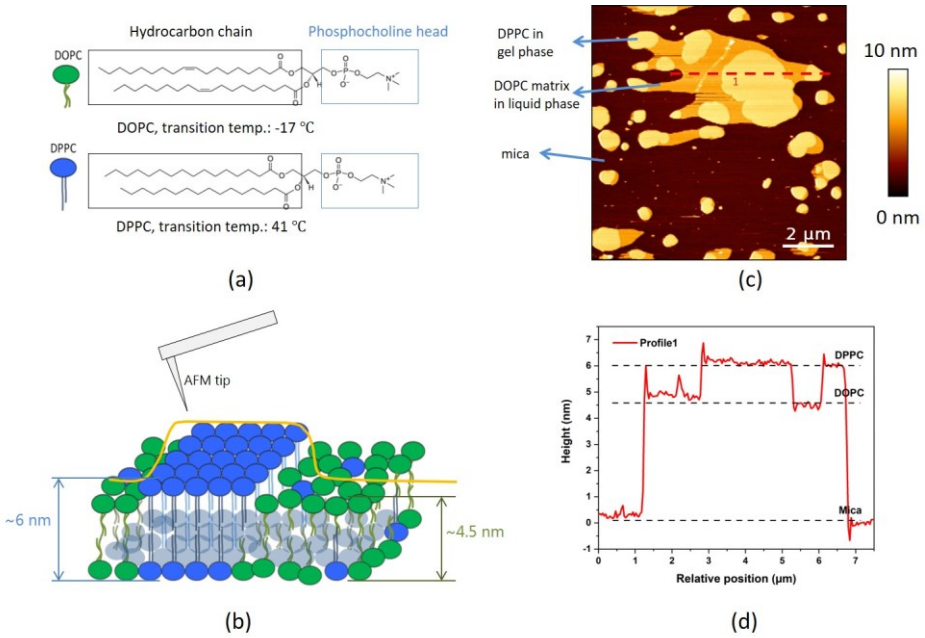

Fig. 27 Schematic diagram of DOPC/DPPC bilayer membrane. (a) The structural formula of DOPC and DPPC. (b) The sketch of DOPC/DPPC bilayer membrane. (c) Topography image of lipid membrane. (d) The profile of line 1 which shows the height difference of DOPC and DPPC.

4.3.2 CaL-induced destruction of lipid membranes

In Moye's publication[110], it is assumed that CaLs interact with lipid membranes by inducing pores like antimicrobial peptides (AMPs) (which can induce 1-4 nm pores on lipid membranes)[115, 116]. Bee venom Melittin is an AMP with a size (26 amino acids) and structure (α helix and amphiphilic) similar to CaL that has been investigated for more than 40 years and was, thus, chosen as reference[117]. Referring to experiments with Melittin[118], 3 different concentrations 0.2 µM, 0.6 µM and 2.5 µM were selected. Time-lapse AFM measurements were conducted to observe the dynamical change of DOPC/DPPC membranes induced by CaL. Mixtures of DOPC and DPPC membranes show phase separations (i.e., DOPC-dominated domains and DPPC-dominated domains). With respect to potential tip interference, there are a few scans to make sure membranes are in a quasi-equilibrium status prior to the injection of CaL. Continuous imaging was used to record the topographic changes of the membranes as a function of time. Fig. 28, Fig. 30, Fig. 32, and Fig. 34 show AFM images of different concentrations of CaLs using time-lapse AFM. Different CaL-induced variations were observed for different concentrations.

i. Membrane reorganization induced by 0.2 µM CaL.

Fig. 28 shows the time-lapse AFM images of DOPC and DPPC domains induced by 0.2 µM CaL in a low coverage of SLBs (in this chapter, based on the exposure area of mica, the case is called low or high coverage). In this case, the 'expansion' of DPPC and the

'reduction' of DOPC are depicted. In other words, CaL caused the structural destruction of lipid membranes. From the proportion variations of DOPC and DPPC (Fig. 29), we know the area of DPPC increased ~2.0 % while the one of DOPC decreased ~5.6 % during the 2-hour measurement (~0.89 %/h and 2.5 %/h, respectively). CaL is a positively charged peptide. With the help of electrostatic interactions and Van der Waals forces, the hydrophilic and hydrophobic parts of CaLs will interact with the PC head and hydrocarbon chains of lipids individually. In such a low coverage case, it seems that CaLs prefer to operate on the edges of lipid domains where lipid molecules will be dissolved by CaLs, causing the 'reduction' of DOPC domains. On intact membranes, such as cell membranes, this edge phenomenon normally cannot be observed, which is also confirmed in the case of high coverage at the same concentration. From this result, we assume that CaLs interact with DOPC but not with DPPC at such a low concentration. The denser structure of DPPC to DOPC may be responsible for this.

In a high coverage case (0.2 μM CaL, see Fig. 30), the whole scanning area was occupied by lipid domains. It is difficult to evaluate the variation of DOPC domains because the edge of DOPC domains could not be observed. However, the 'expansion' of DPPC domains were observed. In the end of the measurement, the area of DPPC domains increased around 8 % (2.9 %/h) (see Fig. 31). In the first 3000 s, the area of DPPC domains increased 7.1 %/h. After that, the variation of DPPC slowed down to around 0.98 %/h. The variation in the first stage shows a great change while in the second stage the change is close to the low coverage case in Fig. 28. Clearly, CaL promoted or even participated in the expansion of DPPC domains which subsequently reached another stable equilibrium. According to our assumptions in the low coverage case, CaLs preferably interact with DOPC first. There is no edge in this case. Thus, CaLs may embed themselves into DOPC domains and 'kick-out' some molecules from their original positions, thereby inducing a reorganization of domains. The embedding of CaLs breaks the phase equilibrium of the whole lipid domains and varies the original partition coefficient. As a result of the new equilibrium induced by CaL, the area of DPPC domains showed a quick expansion in the beginning of the injection of CaL. However, it is difficult to assess the detailed reasons of domain expansions — whether they are from free molecules in the solution or from DPPC molecules within DOPC domains.

For this concentration, it is hypothesized that CaLs prefer to interact with DOPC domains first rather than with DPPC. However, CaLs will promote the expansion of DPPC domains in a short period and subsequently reach a new equilibrium.

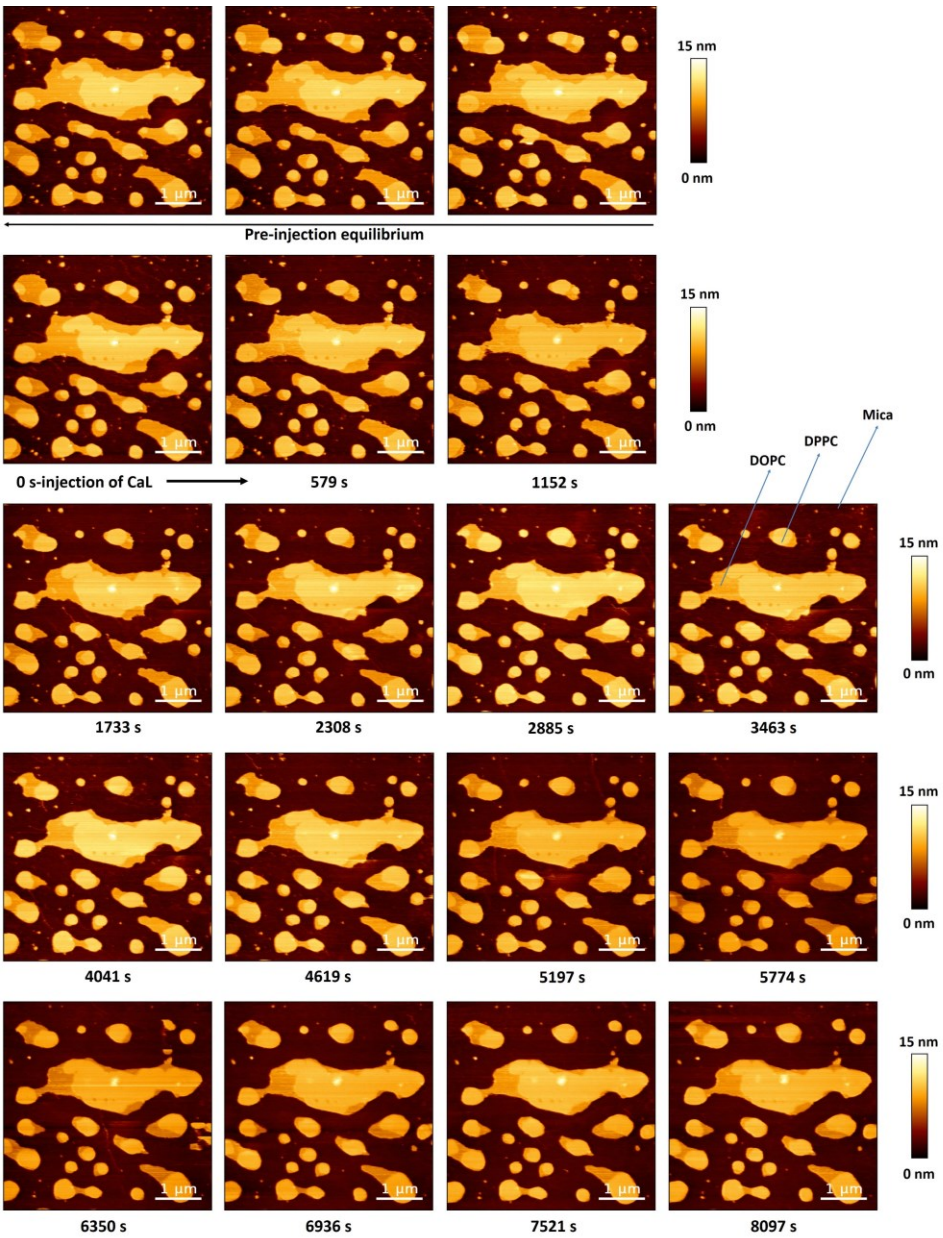

Fig. 28 Membrane reorganization in a low coverage case induced by 0.2 μM CaL. DOPC domains were clearly 'reduced' during the measurement.

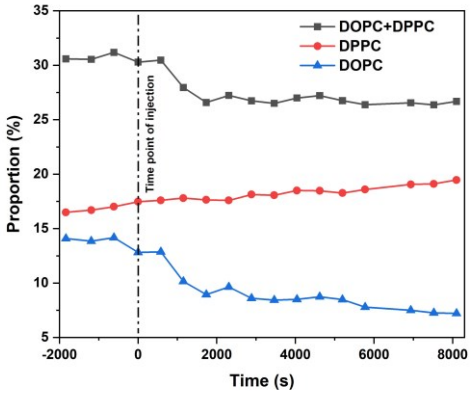

Fig. 29 Domain variations in the low coverage case induced by 0.2 μM CaL.

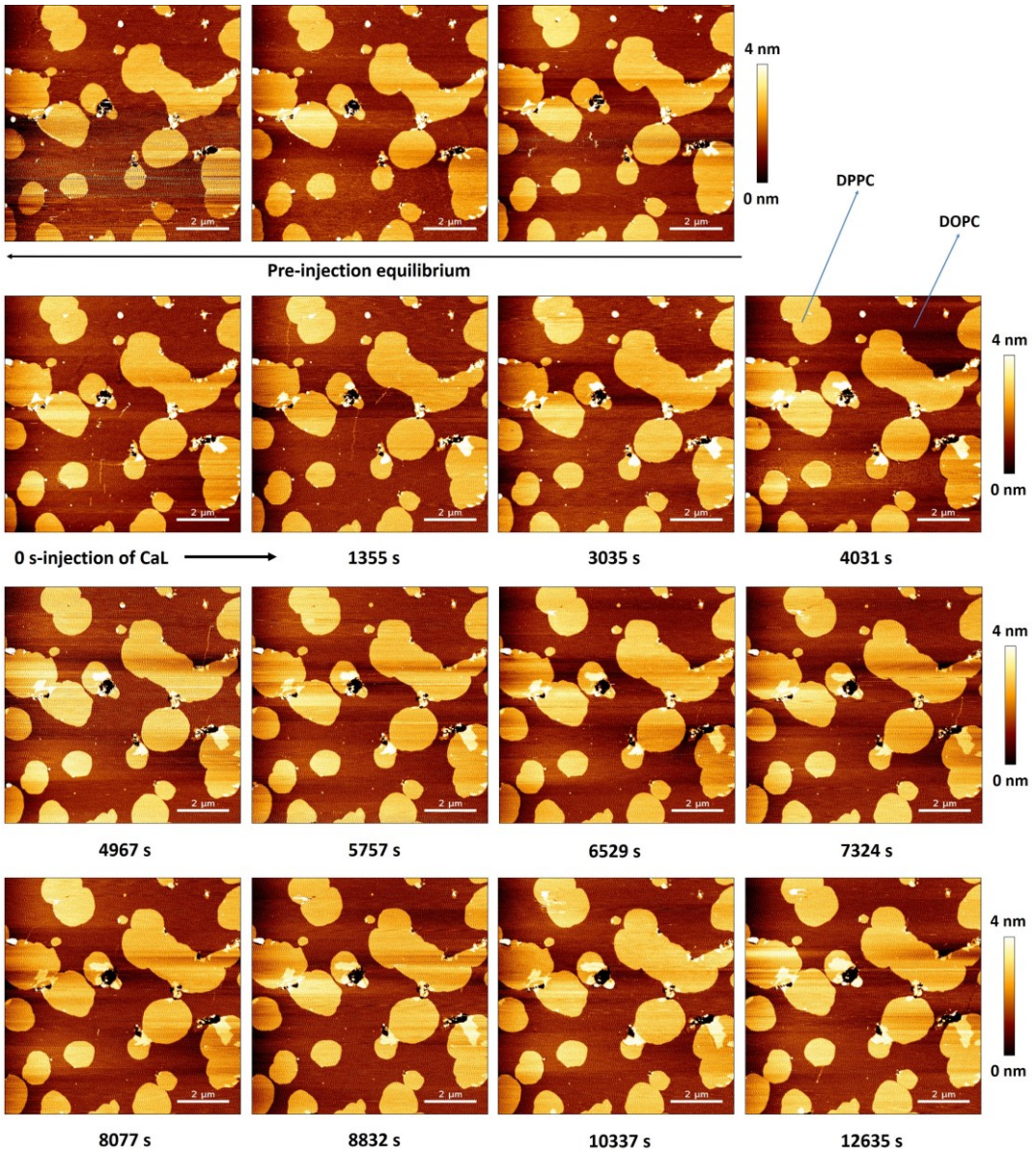

Fig. 30 Membrane reorganization in a high coverage case induced by 0.2 µM CaL. DPPC domains showed obvious expansions.

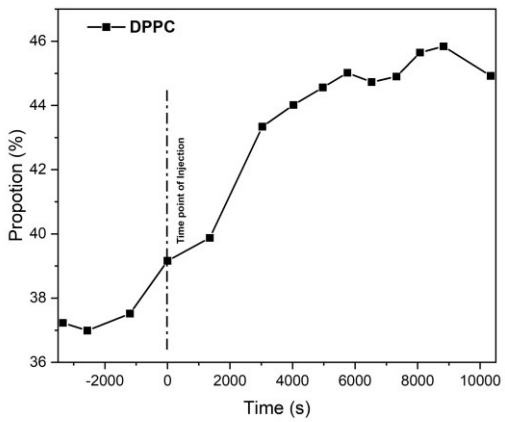

Fig. 31 The DPPC Domain variation in the high coverage case induced by 0.2 µM CaL.

ii. 'Freezing' of membranes with 0.6 µM CaL.

In contrast to the case of 0.2 µM, 0.6 µM CaL caused a different effect on DOPC/DPPC membranes. After the injection of CaL there was much less variation on DOPC and DPPC when compared to the 0.2 µM CaL cases. Fig. 32 presents the images acquired from a high coverage lipid sample during the measurement. Unlike the results at a concentration of 0.2 µM DPPC domains had no clear expansion within ~1.5 hours. It looked like the membranes were 'frozen'.

Fig. 33 shows the proportion of the variation of domains. In the whole process of the measurement, the proportions of DOPC and DPPC domains increased ~5 % and ~0.2 %, respectively. However, the corresponding variation rate is only 2.8 %/h and 0.11 %/h. If CaLs interact with lipids like the low coverage case at 0.2 µM suggests, DOPC domains should be 'reduced'. If CaLs interact like the high coverage case proposes, DPPC should quickly 'expand' in the beginning of the CaL injection. However, the results here are contradictory for the two cases at 0.2 µM CaL. Thus, CaLs choose a different way to interact with lipid membranes.

For this concentration of 0.6 µM, it is hypothesized that most CaLs prefer to assemble themselves into aggregates prior to interacting with membranes. At some concentration region, CaLs may prefer to combine with other CaLs instead of interacting with lipid domains directly. Therefore, no clear changes showed on those DOPC and DPPC domains. The expansion speed of DPPC domains was only ~10% of the low coverage case at 0.2 µM CaL, which indirectly supports such a possibility and our explanation. It can be imagined that once the concentration of CaL is increased, the interaction of CaL aggregates with lipid membranes becomes visible. Indeed, this assumption is confirmed in the following experiment with a higher concentration (2.5 µM).

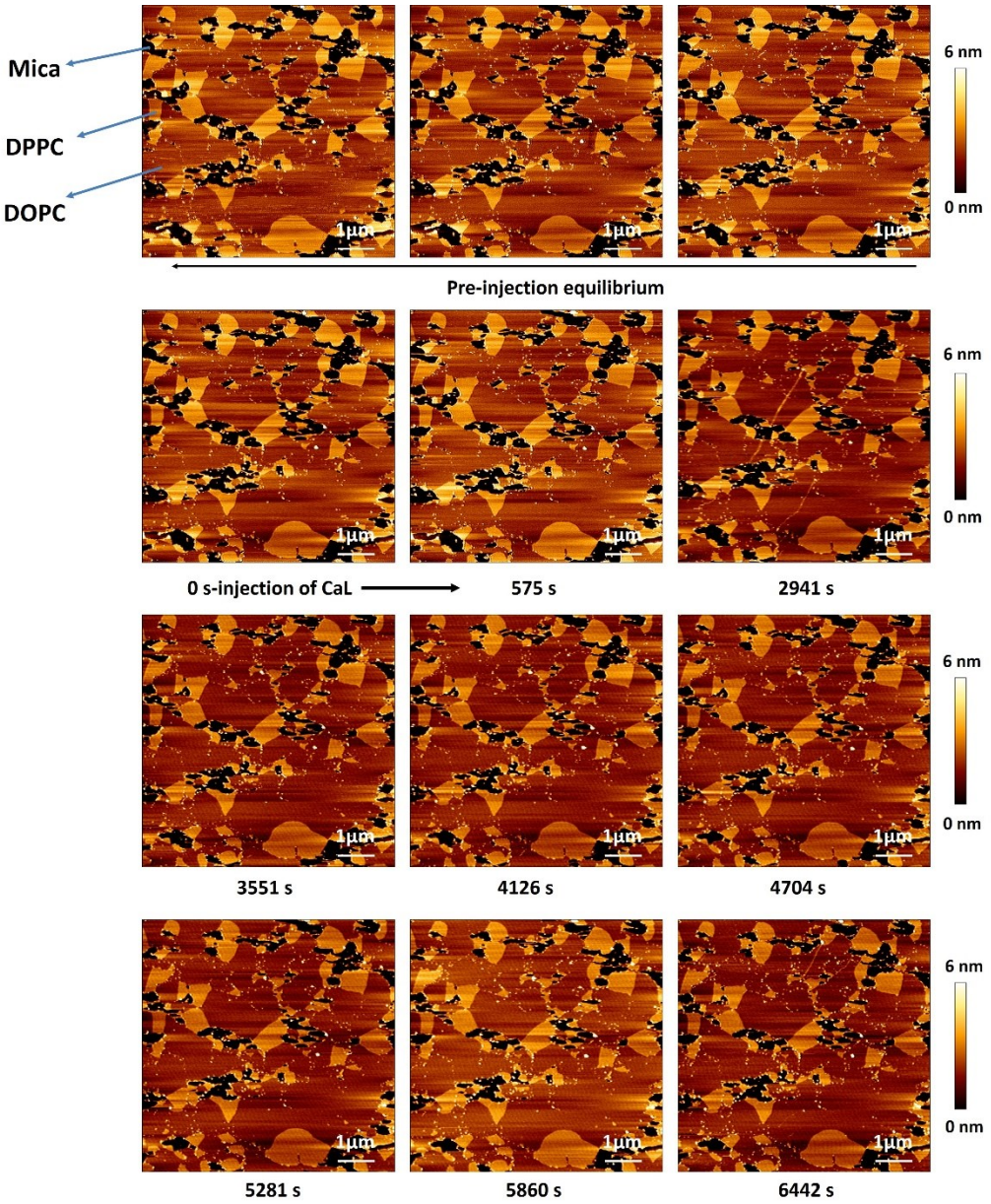

Fig. 32 'Freezing' of membranes with 0.6 μM CaL. Neither DOPC nor DPPC domains showed clear variations.

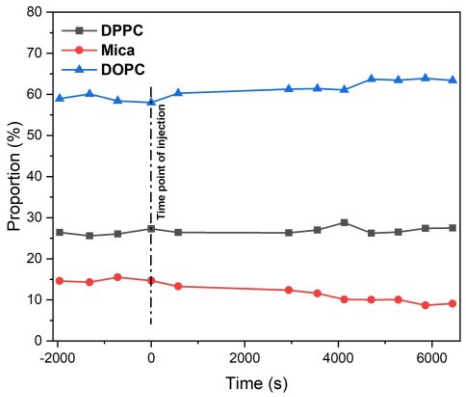

Fig. 33 Domain variations at the concentration of 0.6 μM.

iii. Pore formation upon membranes induced by 2.5 µM CaL.

Fig. 34 is a high coverage case at the same concentration of 2.5 µM CaL. After the injection of CaL, the DPPC domains expanded and finally merged. Meanwhile, a membrane destruction phenomenon was observed at 2210 s after the injection of CaL. The total areas of DPPC domains at each frame are almost the same (Fig. 35).

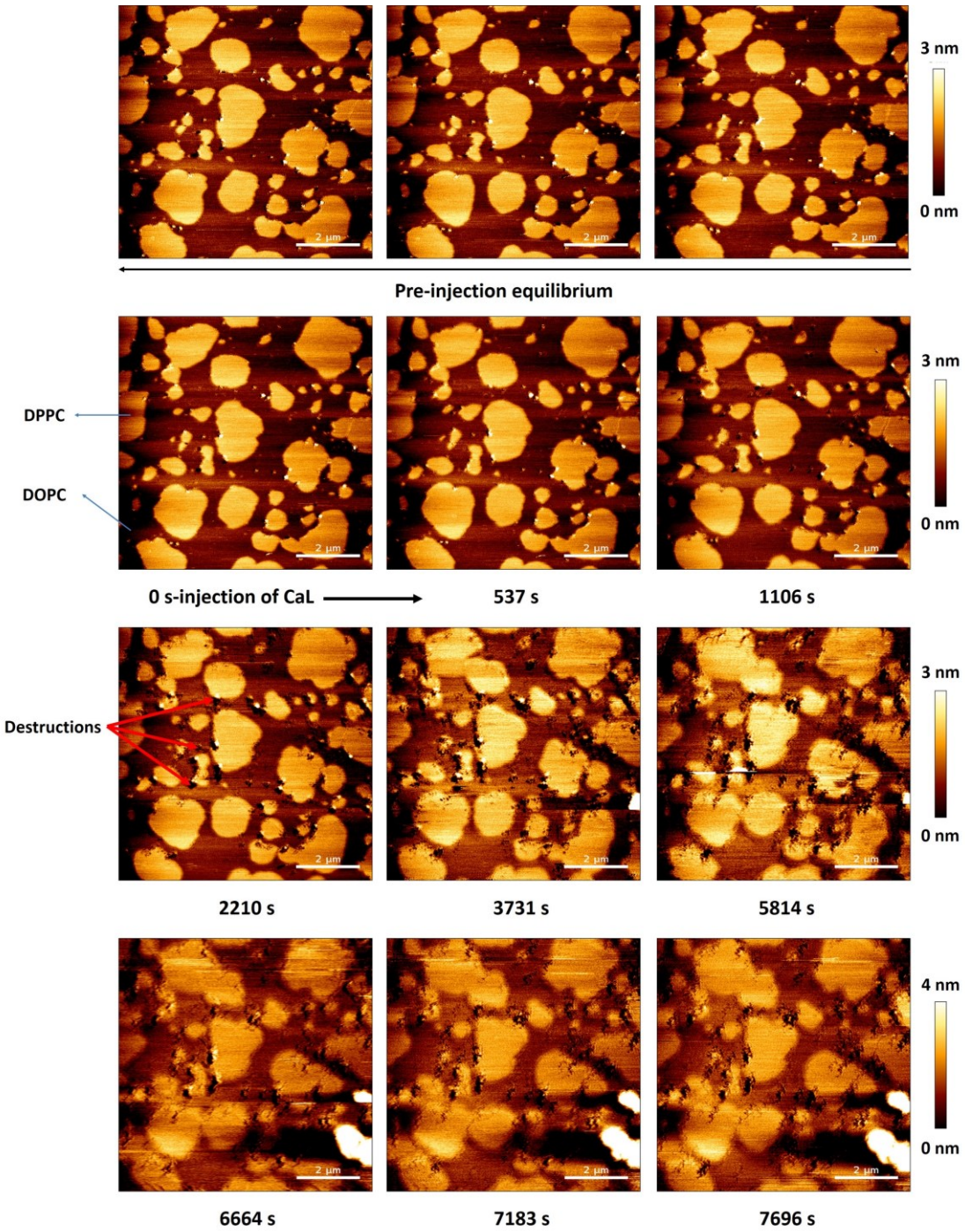

Fig. 34 Membrane alteration on a high coverage case induced by CaL at a concentration of 2.5 µM using time-lapse AFM. Clear membrane destructions were observed on both DPPC and DOPC domains.

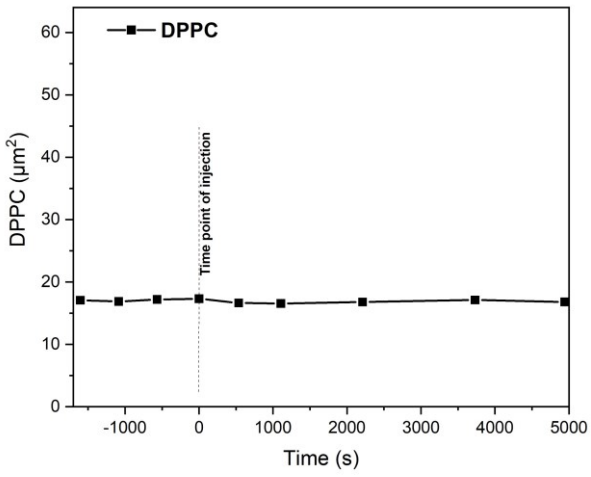

Fig. 35 The variation of DPPC domains at a concentration of 2.5 μM. No clear variation was observed on the DPPC domains in the measurement.

Destruction mostly occurred at the interface of DOPC and DPPC domains. These destructions (which are also called as pores) had different sizes varying from 10 nm to 400 nm, which is much larger than those induced by AMPs[116]. More importantly, this membrane destruction was dynamic. Three different profiles were generated on four frames (0 s-7696 s) to show the variation of membrane destruction on different domains (see Fig. 36).

i. Profile 1 shows the damage on the edge of a DPPC domain, which started to appear after the injection of dCaL. At 5814 s, cracks with ~2 nm depth and ~100-200 nm of width formed on the surface of this DPPC domain. As this value is smaller than the height of the DPPC monolayer, perhaps DPPC molecules are not taken away by CaLs. After that, the damage gradually disappeared over time. It is assumed that CaLs interacted with DPPC molecules and/or embedded into the DPPC domain and teared these cracks.
ii. Profile 2 is made on an intact DPPC domain. During the whole process, the heights of DOPC and DPPC domains were always kept at around 1.5 nm. It is assumed, comapred to DOPC domains, membrane destructions are unpreferrable on DPPC domains.
iii. Profile 3 gives the variation of pores at the interface of DOPC and DPPC domains. These damages mainly existed at the side of DOPC domains. As DOPC domains have a looser structure than DPPC domains, pores will form easier on the surface of DOPC domains. In the 4 selected time points the depths of pores shows clear changes. The depths at 0 s, 2210 s, 5814 s and 7696 s were 0 nm, 3 nm, 2.5-5 nm, and 3-3.5 nm, which corresponds to the heights of the DOPC

monolayer and bilayer, which are 2.3 nm and 4.5 nm, respectively. Thus, it is assumed that DOPC molecules are removed by CaLs layer by layer causing pores. The size variation of these pores indicates that these destructions were dynamic and can recover again.

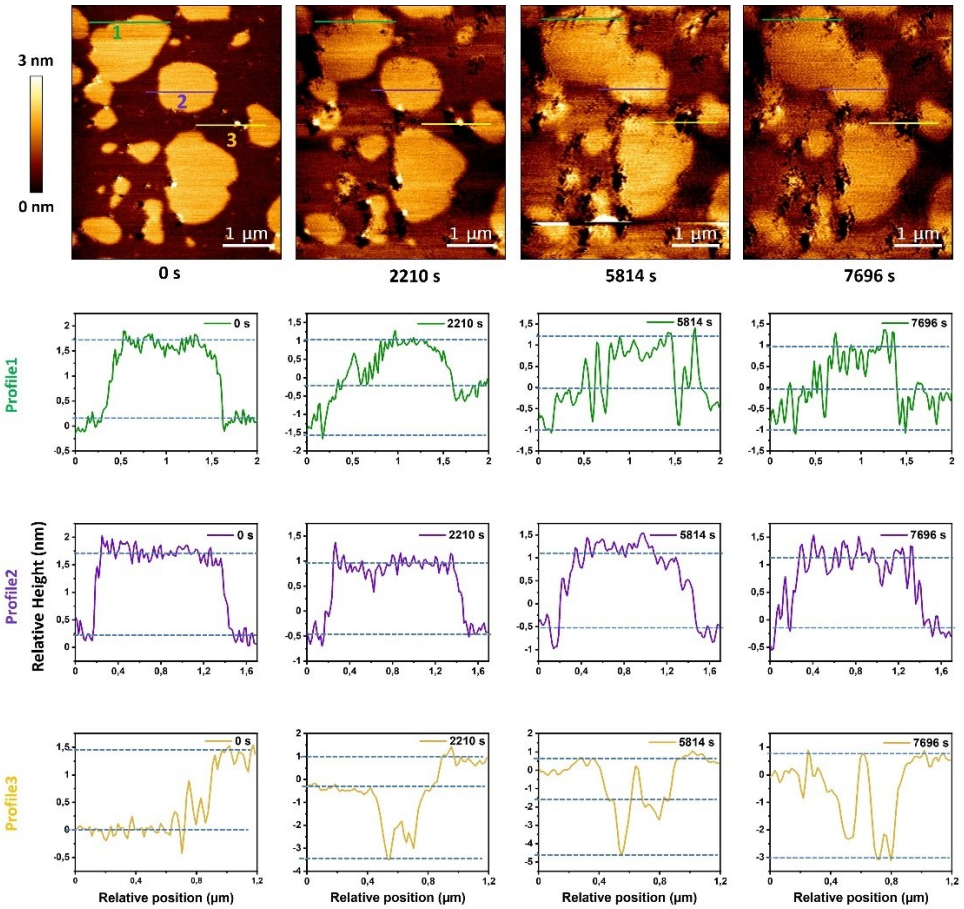

Fig. 36 Dynamical variations of membrane destructions. With time increasing, the pores got deeper first (0-5814 s) but then recovered again (5814-7696 s).

The mode of action of CaL

Concerning the similarities of structure and behavior, the mode of action of CaL is referred to AMPs which are better studied. In the following, some mechanisms describing the the pore formation induced by AMPs will be presented, including the barrel-stave model, toroidal model, carpet model, and detergent-like model[119] (see Fig. 37). In barrel-stave, AMPs embed themselves in lipids and induce pores. The toroidal model works similarly; however, the lipid head will further interact with peptides. Normally, this group of peptides is more hydrophilic than those choosing the barrel-stave model. The carpet model looks like an intermediate model in which peptides spread and aggregate on the surface of lipids and interact with lipids following barrel-stave, toroidal, or detergent-like model. Lastly, in the detergent-like model, pores are induced by the removal of lipids by peptides, which are released into solution again.

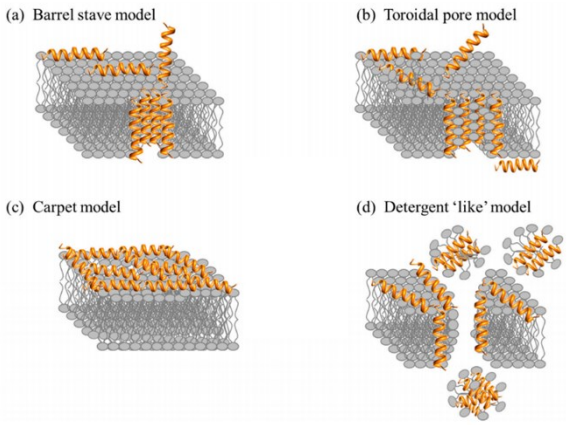

Fig. 37 The mode of action of AMPs. (a) Barrel stave model-AMPs embed into the lipid bilayer membrane. (b) Toroidal pore model-AMPs embed into lipid bilayer membrane with the help of lipid polar heads. (c) Carpet model-AMPs densely aggregate at the surface of lipid membrane. (d) Detergent 'like' model-AMPs bring lipids back into solutions. Adapted from Ref. [119].

Based on the above-presented results from 3 different concentrations of CaLs, the theory from Moye's work is confirmed. Here, possible modes of action of CaL with lipid membranes are proposed (see Fig. 38).

1. At a low concentration (see Fig. 38a), CaLs prefer to interact with lipid domains in liquid phases (like DOPC here) rather than domains in gel phases. During this process, domains in gel phases (like DPPC) may exhibit continuous expansion, which may be the joining of free molecules from domains in liquid phases and/or solutions through phase repartitions.
2. At an intermediate concentration (see Fig. 38b), CaLs prefer to assemble into aggregates first before interacting with lipids. In this case, the destruction of lipid membranes by CaLs should be at the minimum.
3. At a high enough concentration (see Fig. 38c), CaL aggregates will gradually destruct the structure of lipid membranes causing damage to the membrane, like pore formation, especially at the interface of liquid and gel phases (like the interface of DOPC and DPPC).

Among these, the carpet model should be one of the modes of action for the intermediate concentration of 0.6 µM. However, the pore formation is more complex. It may be a comprehensive process of other pore formation models. In the case of 2.5 µM CaLs, the pore depths on a DPPC domain were smaller than the height of the DPPC monolayer while the pore depths on DOPC domains reached the heights of the DOPC monolayer and bilayer. Subsequently, these pores gradually recovered and even disappeared. Thus, the interaction with DPPC is possibly following the barrel-stave or

toroidal model, while the interaction with DOPC should be follwing the detergent-like model. However, AFM results do not suffice to confirm these hypotheses. More investigations have been conducted in order to validate them. The best way to check the hypotheses is via '*in-situ*' analyses. Fluorescence is the method of choice for realizing *in situ* high-resolution imaging[120]. However, the fluorophore labelling will strongly affect the behavior of labelled peptides, which limits the application of fluorescence in this research. Consequently, Raman spectroscopy is more promising as it is label-free and, thus, the influence of extraneous labeling can be excluded.

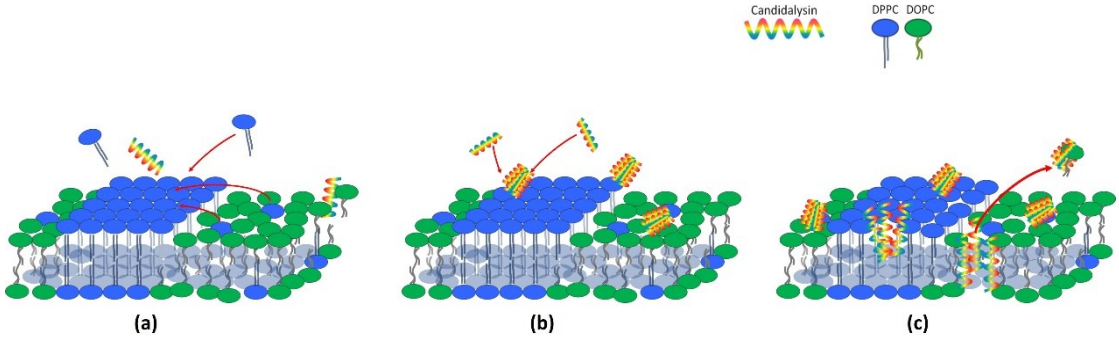

Fig. 38 Proposed modes of action of CaL at different concentrations. (a) Reorganization of DOPC and DPPC at a low concentration of CaL (0.2 µM); (b) Aggregations of peptides at an intermediate concentration of CaL (0.6 µM); (c) Membrane alteration at a high concentration of CaL (2.5 µM).

4.4 Topographies of cells infected by dCaL

4.4.1 Topographies of dCaL-infected cells in liquid

Compared to artificial lipid membranes, the structure of an actual cell membrane is denser, as it is further stabilized and protected by other components like sugars and proteins. Thus, a higher concentration of CaL has to be applied in the infection of cells to get a visible membrane destruction on cells. In other words, cell membranes have a higher resistance to the destruction of CaL than the simple artificial DOPC/DPPC membranes. AFM images of cells incubated with 10 µM dCaL were acquired using a very soft tip (CSG30) in contact mode. Fig. 39 shows AFM images of a cell in liquid, which has an integral cell structure with a size around 15x15 μm^2 and a height of 2.5 µm. However, no clear features of membrane damages on the surface of the cell were recognized. In a 1x1 μm^2 scale (the zoomed-in position in the yellow frame of Fig. 39) the surface was integral, which differs from the results in Fig. 34. A possible reason is that the pores were very small and thus below the detection limit of AFM. The diameter of the tip is 20 nm, which means it is difficult or even impossible to detect pores smaller than 20 nm.

In addition, a lot of corrugations/ridges were observed on the cell surface. These corrugations/ridges are called microplicae and are the typical structure of epithelial cells of oral mucosa[121]. Similar to to the mucus layer covering the cells *in vivo* [122, 123], microplicae covered with glycocalyx could be regarded as the second protection layer[124]. Microplicae are assumed to increase the mechanical intensity and the contact with adjacent cells while the negatively charged glycocalyx in the layer will intercept pathogens before they can interact with cell membranes. Moreover, microplicae are also rich in mucins which can provide further protections[125]. In Fig. 39, the detectable corrugations had heights up to 600-800 nm, which strongly affects the detection of the real topography of cell lipid membranes.

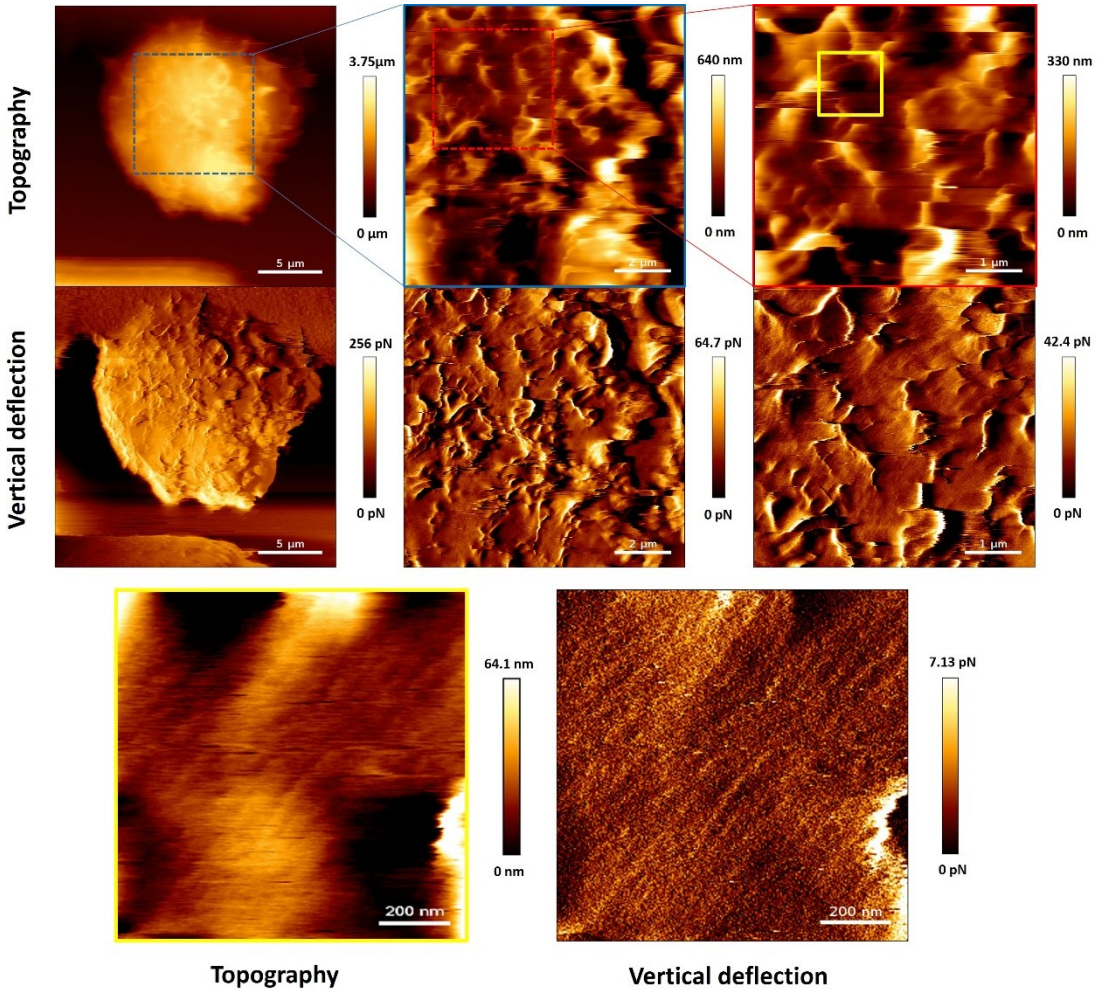

Fig. 39 AFM images of a dCaL-infected cell in liquid. No clear membrane destructions could be observed on the surface of this cell.

4.4.2 Topographies of dCaL-infected cells in air

In contrast to cells in liquid, cells dried in air are easier to image with AFM and normal tapping AFM tips (here NSG10) can be used. Such dried cells show different

topographies compared to cells in liquid. All microplicae features disappear as they lay down on the surface once cells are dried. In Fig. 40, the cell has a size of 20x20 μm^2 with a height of 500-600 nm. On this cell, the most apparent feature are large holes formed on the cell surface, propably caused by the collapse of cell membranes. Most of them have diameters of tens to hundreds of nanometers. The diameter of the largest one in the figure reached 1 µm. In this case, more inner cell compositions should be exposed on the cell's outside. The interference of the pericelluar coat should be weakened. It is speculated that dCaLs promote the formation of these holes, which means there would be a higher possibility of finding dCaLs around these holes.

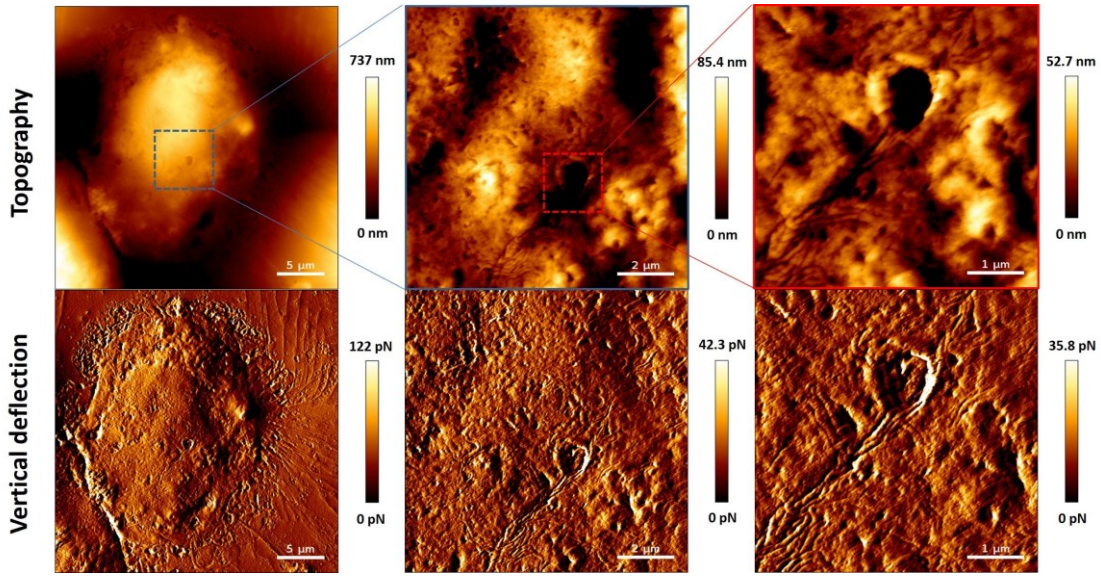

Fig. 40 AFM images of a dCaL-infected cell in air. Pores in different sizes could be observed.

4.5 Raman investigations of CaL and lipids

4.5.1 Conventional Raman spectra of CaL and lipids

Conventional Raman spectra of DOPC and DPPC

Except for the double bonds on hydrocarbon chains, DOPC has a similar structure to DPPC. 20 µL 3 mM DOPC and DPPC were dried onto glass slides for the convential Raman measurements, respectively. A 14.8 mW 532 nm laser was used as the power source. The exposure time was 10 s with 10 accumulations (The final spectrum was averaged). In this experiment, the Raman spectra for comparing the spectra of CaL and dCaL were all acquired from 2400-800 cm^{-1}. The main chemical bonds like C-N from choline heads, PO_2 from phosphate groups, C-C from skeletons, C=C from hydrocarbon chains, and C=O from esters are all identified in Fig. 41 and assigned in Table 4. The main differences between DOPC and DPPC are C=C double bonds at 1649 cm^{-1} and the corresponding skeletal C-C stretching affected by C=C bonds at 1124 cm^{-1}.

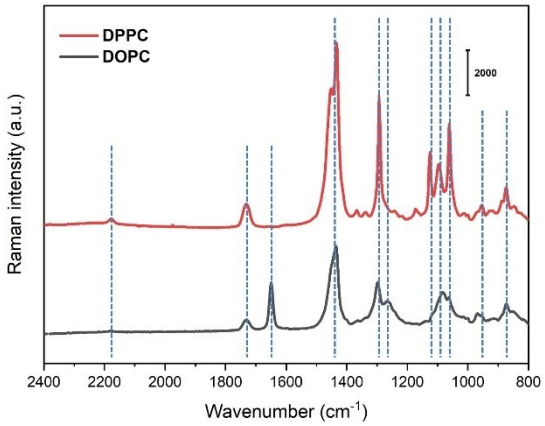

Fig. 41 Conventional Raman spectra of DOPC and DPPC. The main bands are labelled by dash lines which are assigned in Table 4.

Table 4 The assignment of main Raman bands of DOPC and DPPC[126, 127]

Bands (cm^{-1})	Assignment	Remarks
874	C-N stretching	Both
953	C-N stretching	Both
1062	C-C stretching	Both
1083-1096	PO_2 stretching	Both
1124	C-C stretching	Only DPPC
1265	cis C=C deformation	Only DOPC
1293-1296	CH_2 twisting	Both
1434	CH_2 bending	Both
1649	C=C stretching	Only DOPC
1730	ester C=O stretching	Both
2178	Overtone of PO_2	Only DPPC

Conventional Raman spectra of CaL and dCaL

Even though Raman spectra can distinguish molecules with different chemical bonds, it is hard to distinguish molecules with similar chemical compositions. In other words, Raman spectra cannot distinguish CaL from the background of cell membranes assembled with other peptides and proteins, sufficiently. Thus, a deuterium strategy (the phenylalanine of CaL is fully deuterated, d5-Phe) was introduced to improve the distinction of CaL from cells. In the following, this deuterated CaL is abbreviated as dCaL.

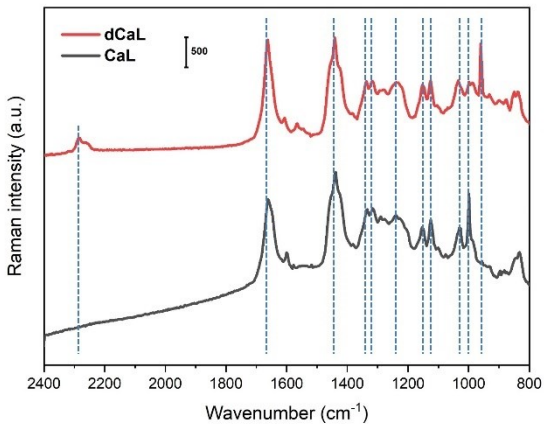

Fig. 42 Conventional Raman spectra of CaL and dCaL. The main bands are labelled with dash lines which are assigned in Table 5.

Table 5 The assignments of main Raman bands of CaL and dCaL[128-130]

Bands (cm^{-1})	Assignment	Remarks
960	d5-Phe ring breathing	dCaL
988	d5-Phe ring bending?	dCaL
1000	Phe ring breathing	CaL
1030	Phe ring bending	CaL
1124	C-C stretching	Both
1152	C-O stretching	Both
1238	Amide III	Both
1316	CH_2-CH_3 stretching	Both
1333-1337	CH_2-CH_3 wagging	Both
1438-1441	CH_2 bending	Both
1662	Amide I	Both
2260	C-D symmetrical stretching	dCaL
2285	C-D asymmetrical stretching	dCaL

In this thesis, the phenyl ring of phenylalanine on dCaL is fully deuterated. The C-D stretching appears in the Raman silent region (2800-1800 cm^{-1}) where most chemical bonds do not have signals (except for triple bonds). Additionally, the ring breathing mode of the deuterated phenyl ring is used as second reference to recognize dCaL. In this way, dCaL can be distinguished from cell membranes. Fig. 42 shows the Raman spectra of CaL and dCaL. 10 µL 1.4 mM CaL and dCaL were dried on glass slides, respectively. A 14.8 mW 532 nm laser was used as the power source. The spectra were

acquired with an exposure time of 10 s with 10 accumulations (The final spectrum was averaged). The similarity of their Raman spectra shows that the deuterated phenylalanine does not change the main conformation of CaL. As CaL is an only recently identified fungal peptide, this is the first Raman work on it. Most of the main Raman bands are assigned. Disregarding the slight band shifts, the biggest differences between CaL and dCaL are the deuterium-related bands at 2285 cm^{-1} and 960 cm^{-1} from C-D stretching (including the asymmetrical stretching at 2285 cm^{-1} and a weak symmetrical stretching at 2260 cm^{-1}) and ring breathing mode, respectively (see Table 5). The amide I band at 1662 cm^{-1} shows that CaL/dCaL is in helical structures and may with some turns (the proline of CaL may introduce a turn on structure.)[129, 131]. This result matches the calculated structure of CaL in Fig. 24b.

The spectra of lipids and CaL/dCaL are further compared (Fig. 43). CH_2 bending and C=C/amide I bands (labelled with yellow columns) are very close to each other. In contrast, PO_2 stretching, ring breathing, C=O stretching, CH_2 bending, and C-D stretching are more distinguishable.

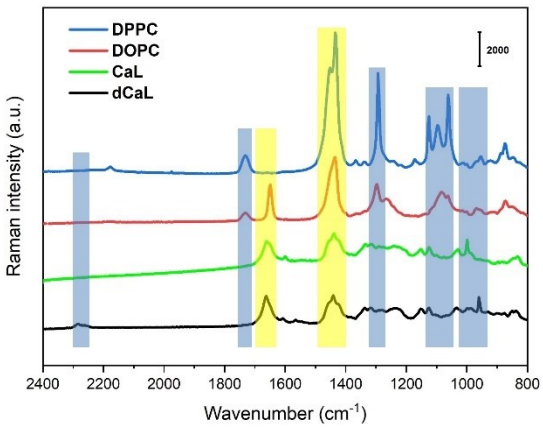

Fig. 43 Conventional Raman spectra of CaL/dCaL and lipids. CaL/dCaL have close band positions at 1440 cm^{-1} and 1660 cm^{-1} to DOPC/DPPC which are labeled by yellow colums. In contrast, other bands (labelled by blue colums) like C-D bands, ring breathing mode and C=O stretching show clear differences.

Conventional Raman spectra of dCaL/lipid mixtures and vesicles

Above-mentioned spectra were acquired from free molecules. Once lipids are assembled into bilayers or vesicles, it is supposed that signals from hydrocarbon chains of lipids will be weakened or even disappear.

In the range of this thesis, freshly prepared vesicles/SLBs were investigated and compared with the spectra of lipid mixtures (see Fig. 44). Following the protocol of preparing SLBs, 1 mM DOPC-DPPC vesicles were prepared and dropped onto a cleaned

coverslip for Raman measurement. The sample was measured immediately (without an incubation). Thus, most lipids should be still in vesicles (in liquid). In addition, vesicles are expected to provide similar and comparable Raman spectra to SLBs due to their similar bilayer structures. 3 mM DOPC-DPPC mixture (in organic solution) were dried for a control measurement. In this mixture, lipids are in the status of free molecules. 14 mW laser power and 10 s exposure time were applied during the Raman measurement. From the spectrum of lipid vesicles, the Raman spectrum of SLB could be predicted.

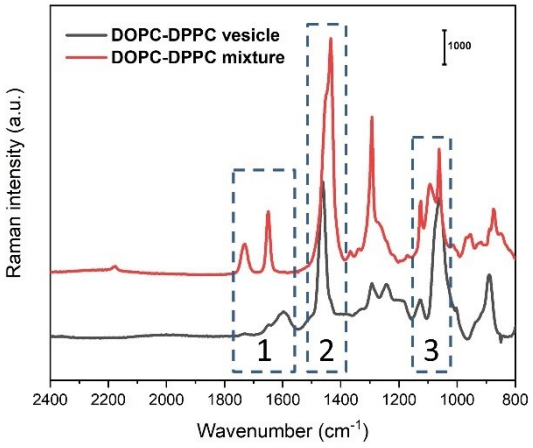

Fig. 44 Conventional Raman spectra of DOPC/DPPC vesicles and mixtures. In the mixtures, DOPC and DPPC were mixed freely without any extra processing. The Raman spectra of such mixtures show clear structure difference to the vesicles in the 3 labelled regions.

The spectrum of DOPC-DPPC vesicle differs from the one of the DOPC-DPPC mixture in region 1 (1800-1600 cm^{-1}), region 2 (1500-1400 cm^{-1}), and region 3 (1200-1000 cm^{-1}). Firstly, in region 1, signals from C=C stretching and C=O stretching were clearly weakened, and one new broad band appeared at around 1600 cm^{-1}. Secondly, in region 2, the CH_2 bending of DOPC-DOPPC shows a clear shift from 1434 cm^{-1} to 1461 cm^{-1}. Lastly, in region 3, PO_2 stretching disappeared and the two C-C skeletal stretchings exhibited significant changes in intensities. Apart from that, the C-N stretching from the choline head at around 870 cm^{-1} could be observed. The above-mentioned phenomena indicate that hydrocarbon parts of lipids are assembled into the bilayer structure.

Subsequently, dCaL in an equal volume (final concentration of dCaL, ~700 µM) was mixed with the DOPC-DPPC vesicles in advance. Likewise, no incubation was conducted on the substrate to minimize possible damage of vesicle or SLB structures. If dCaL actually destroys the structure of the vesicles, the spectrum of the sample will show a clear change (some signals from free lipids would appear). In fact, the spectrum

of vesicles with dCaL differs only minimally from the spectrum of lipid vesicles (see Fig. 45a). The differences in 4 labelled regions originate all from dCaL, like C-D stretching at 2285 cm^{-1}, amide I band at 1662 cm^{-1}, and ring breathing mode at 960 cm^{-1}. Moreover, because of the low Raman cross-section limit, 700 µM dCaL in liquid cannot be detected at the same setting. The bands of dCaL in the spectrum indicate that CaL accumulated on the surface of the vesicles. In other words, CaL actually interacts with lipids. To mimic the destruction of vesicles/SLBs induced by dCaL the spectrum of a mixture of lipids and dCaL was acquired (Fig. 45b). In such a case, the lipid signals are recovered. This spectrum also confirms that the C=C band of DOPC will mix with the amide I band of dCaL in Raman measurements and shows the importance of deuterium strategy.

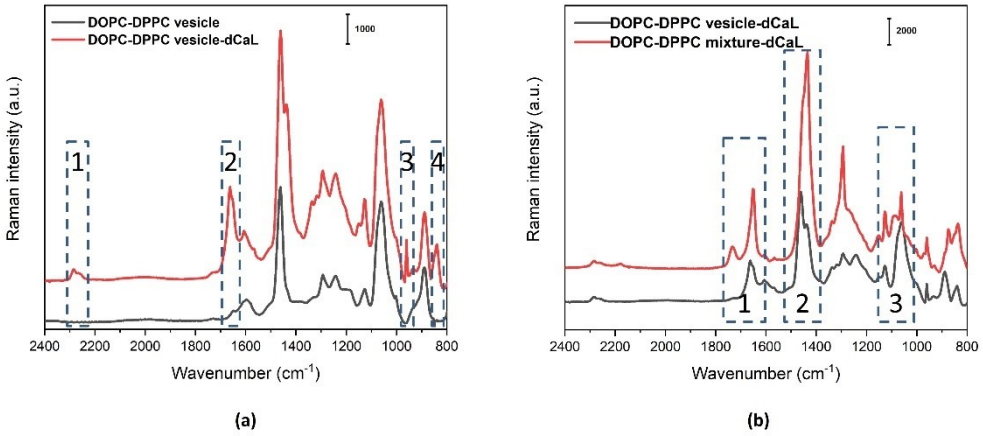

Fig. 45 (a) Conventional Raman spectra of a DOPC-DPPC vesicle with and without dCaL. 4 labelled regions show the existence of dCaL. (b) Conventional Raman spectra of DOPC-DPPC vesicle and mixture with dCaL. 3 labelled regions show the difference between lipid vesicle and mixture.

These results suggest that dCaL does not break the bilayer structure of the lipid membrane completely. A conventional method is not sufficient to detect the tiny regional destruction induced by CaL/dCaL. Nevertheless, the gathered conventional Raman spectra will serve as reference for the following enhanced Raman experiments.

4.5.2 SERS spectra of CaL and lipids

In conventional Raman experiments, the spectra of lipids and CaL/dCaL were obtained from their highly concentrated stock solutions in the millimole range. However, the *'in vivo'* concentration of CaL is estimated to be only a few tens of micromole[110], which cannot be detected by conventional Raman spectroscopy. Enhanced Raman spectroscopy, however, shows high sensitivity in detecting minute amounts of substances. In view of the spectral variation in enhanced Raman spectroscopy, the SERS spectra of these molecules were also investigated.

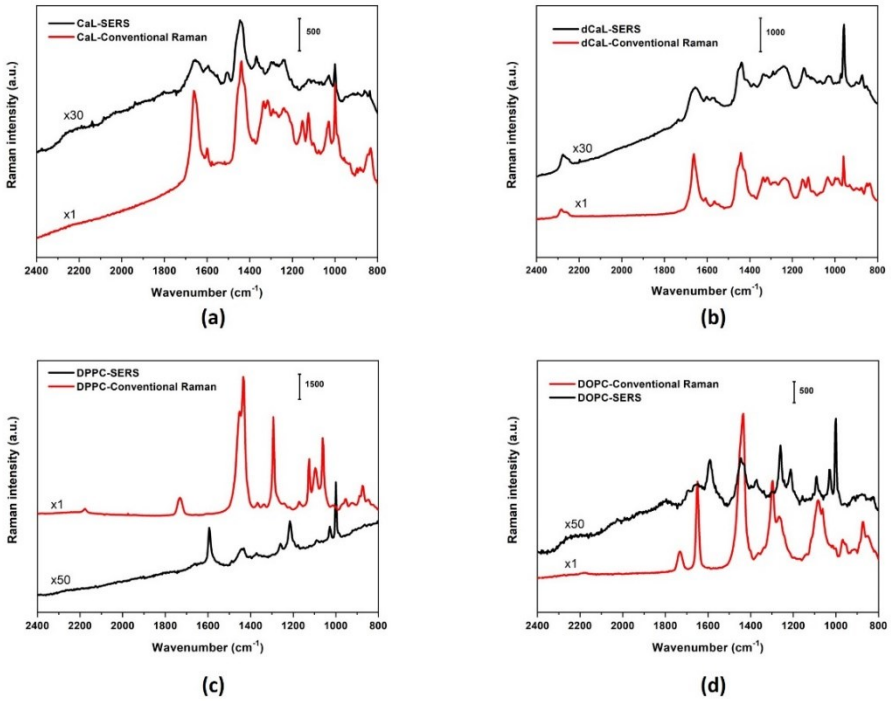

Fig. 46 Conventional Raman and SERS spectra of (a) CaL, (b) dCaL, (c) DPPC and (d) DOPC

SERS spectra of CaL/dCaL and lipids were acquired using the iodide-treated method introduced in Chapter 3. This method has a detection limit up to 1.4 µM dCaL which could meet the requirement of this research. Fig. 46 shows the comparison of SERS spectra of CaL/dCaL and lipids to their conventional Raman spectra from Fig. 41 and Fig. 42. 100 µM DOPC and 140 µM dCaL were mixed with 1 mM iodide solution in equal volumes, respectively and exposed to a 170 µW laser while 100 µM DPPC was mixed 1 mM iodide solution in equal volume and exposed to a 100 µW laser. In contrast, dCaL was mixed iodide solution to reach a final concentration of 110 µM and 10 mM, respectively and exposed to a 25 µW laser. All of SERS spectra were acquired at 1s exposure time with 300 accumulations (The final spectrum was averaged.) The SERS spectra of CaL and dCaL do not differ much from their conventional Raman spectra in which most characteristic bands could be detected like C-D stretching and ring breathing mode. In contrast, the SERS spectra of DOPC and especially DPPC clearly differ from their conventional Raman spectra. One of the reasons could be the interaction of lipids and Ag plasmons. Secondly, the possible contamination of the sample can also affect the measurement. In SERS measurements, vibrations of molecules cannot be enhanced unless the molecules are within a suitable proximity of the plasmons. Additionally, compared to the positive charges of CaL/dCaL, DOPC and DPPC are zwitterionic which may further affect the interaction. Thus, lipids show deviating SERS spectra compared to their conventional Raman spectra. The selectivity of iodide-treated Ag SERS substrates may also affect the measurements. So far, the

reasons why lipids show different SERS spectra are not fully understood. A new band is found at 1000 cm^{-1} in the lipid spectra of lipids, which is normally assigned to the ring breathing mode from the benzene ring. At present, this newly formed band cannot be explained. As the ring breathing mode of dCaL shifts to 960 cm^{-1} the interference of the newly formed band at 1000 cm^{-1} is avoided.

4.5.3 TERS spectra of dCaL

A 7 µM dCaL sample was dried on a cleaned glass slide used for TERS measurements. In the AFM image, dCaL molecules were found to aggregate (Fig. 47a). A random 300x300 nm^2 region was chosen and a 10x10 grid was set. The acquisition time was 2 s. From this experiment, 43 spectra with sufficient SNR were selected. The signal of the amide I band confirms that the measurements were performed on a peptide/protein sample.

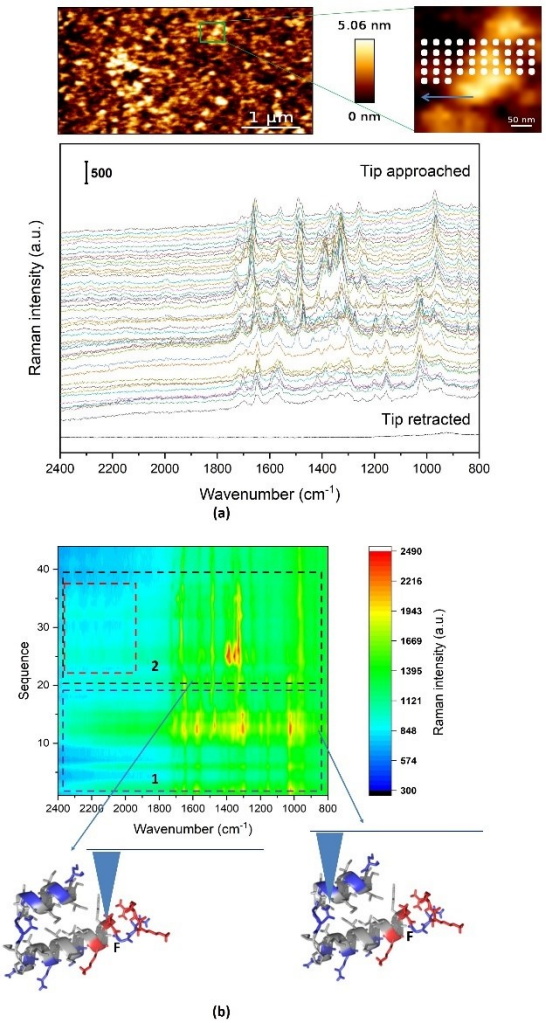

Wavenumber (cm^{-1})		Assignment
Group 1	Group 2	
-	833	Skeletal stretching?
843	-	
-	880	
950	-	?
-	965	Deuterated ring breathing
1027	-	?
-	1057	?
1096	-	C-C skeletal, C-O, C-N stretching
1156	-	
1195	-	
-	1259	Amide III
1270	-	
1299	-	?
1329	1329	CH, CH_2, CH_3 (Wagging, deformation, bending)
1363	1363	
1385	1385	
-	1415	
1480	1480	
1517/1571	1560	Amide II
1648	-	Amide I
-	1674	
1696-1710	1710-1730	C=O stretching
-	1921	?
-	1997	?
-	2144	?
-	2207	?
-	2283	C-D stretching
-	2330	?

(c)

Fig. 47 Selected TERS spectra of dCaL. (a) TERS spectra, (b) Contour image and speculation of spectral difference and (c) Assignments of spectra[132].

Although this is a clean peptide sample, the spectra are quite different, probably due to the random molecular orientations of dCaLs and the interaction with plasmonic Ag (Fig. 47a). As a nanoscale technique, TERS is sensitive enough to detect these differences and map their corresponding spectra, consequently such variations are typical for unordered compounds. According to the positions of bands and based on the SERS experiments in the previous section, these spectra can be divided into two groups (Fig. 47b), which can be further assigned (Fig. 47c). Two important features were found in these spectra. Firstly, concerning the amide I bands in these two groups: regarding the reasonable band shift, the amide I bands in group 1 indicate that the target is in an α helix structure while those in group 2 show that the conformation may be in another structure, which may be 3_{10} helices or even β turn[132-134]. These two structures normally exist at the N- and/or C- termini of the structure as an extension of α helix, which also match the emergence of deuterium signals located at the end of the peptide. This phenomenon marks the intramolecular conformation difference of CaL. Secondly, compared to group 1, group 2 provides stronger bands at 960 cm^{-1} and 2280 cm^{-1}, which could be assigned to deuterated ring breathing and C-D stretching. In Chapter 4.5.2, it was found that the deuterium-related bands are less affected by plasmonic particles. Therefore, these two bands are used as reference. It is believed that the differences between the two groups are because the tip in group 1 was measuring far away from phenylalanine, while the tip was closer to phenylalanine in group 2 (Fig. 47b). The C=O stretching is thought to originate from the counter molecule trifluoroacetic acid in the sample.

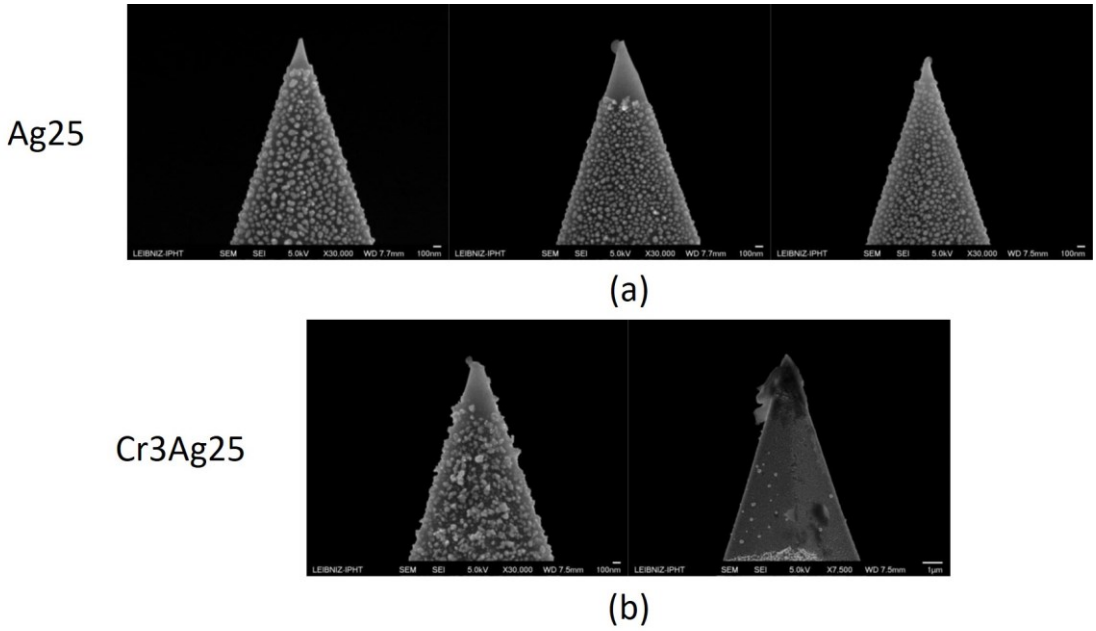

Fig. 48 SEM images of TERS tips- (a) Ag25 and (b) Cr3Ag25 tips after measurements of dCaL samples. All Ag particles at tip apexes were removed.

During the experiments, it was found that biosamples are rather sticky and will strongly interact with the Ag nanoparticles. Fig. 48 presents a few cases of tip destruction caused by samples. In Fig. 48a particles of Ag25 tips were totally removed by samples. Based the sharp border, it is supposed that these tips snapped into the samples due to the strong adhesions and the silver particles remained in the sample. This phenomenon was also observed in following Raman spectra where very strong and random spectra could be recorded regardless of the positions of the tips. Even though a Cr layer increases the adhesion of Ag particles to the tip, tip destruction could still be observed. In Fig. 48b, Cr3Ag25 tips show two cases of particle removal and tip contamination. The strong adhesion of biosamples is one of reasons for the low success rate in TERS measurements. Currently, an inert protection coating of the Ag particles is in test.

4.6 Investigations of dCaL-infected cells using TERS spectroscopy

4.6.1 SERS measurements on dCaL-infected cells

SERS measurements were conducted prior to the TERS measurements on dCaL-infected cells. SERS substrates were directly placed upside down onto dCaL-infected cell samples. Fig. 49 presents the SERS spectra of dCaL-infected cells. Surprisingly, only CH_2 bending at 1441 cm^{-1} and amide I band at 1659 cm^{-1} were observed. The deuterium signals from dCaL were not detected. According to our experiments in Chapter 4.3 using time-lapse AFM, it is hypothesized that dCaL will aggregate and reside on the surface of lipids. Thus, SERS spectroscopy should be able to detect dCaL aggregates on the surface. Based on the SERS spectrum (see Fig. 49) of cells, it is assumed that the protein signals were from microplicae. In order to confirm this assumption, TERS measurements were further conducted.

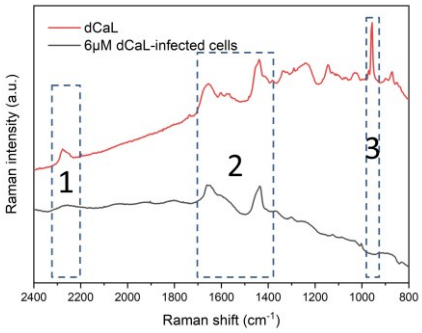

Fig. 49 SERS spectra of dCaL and dCaL-infected cells. Only C-H band and amide I band were found. There is no signal from dCaL which could be recognized.

4.6.2 TERS measurements on dCaL-infected cells

The dCaL-infected cell samples were washed and dried with Argon and then immediately used for TERS measurements. Fig. 50 shows a selected TERS measurement, where a 25x4 grid was set at the edge of a large pore on a cell. The acquisition time was 1 s and the laser power 850 µW.

Regarding the coverage of microplicae (and glycocalyx), the measurement was performed on the edge of the pore. It was hoped that more lipids and dCaLs would be exposed on the outside at this position than at other integral positions. In conventional Raman spectra lipids show characteristic bands at ~1080-1096 cm^{-1} of PO_2 and ~1750 cm^{-1} of ester C=O differing from protein characteristic bands at ~1650 cm^{-1} of amide I and ~1580/1520 cm^{-1} of amide II. These are the reference for distinguishing lipids and proteins. However, the orientation of lipids makes the PO_2 and C=O bonds buried in the bilayer structure, which are difficult to be detected. Additionally, band shifts may happen due to the environmental influence from other membrane components.

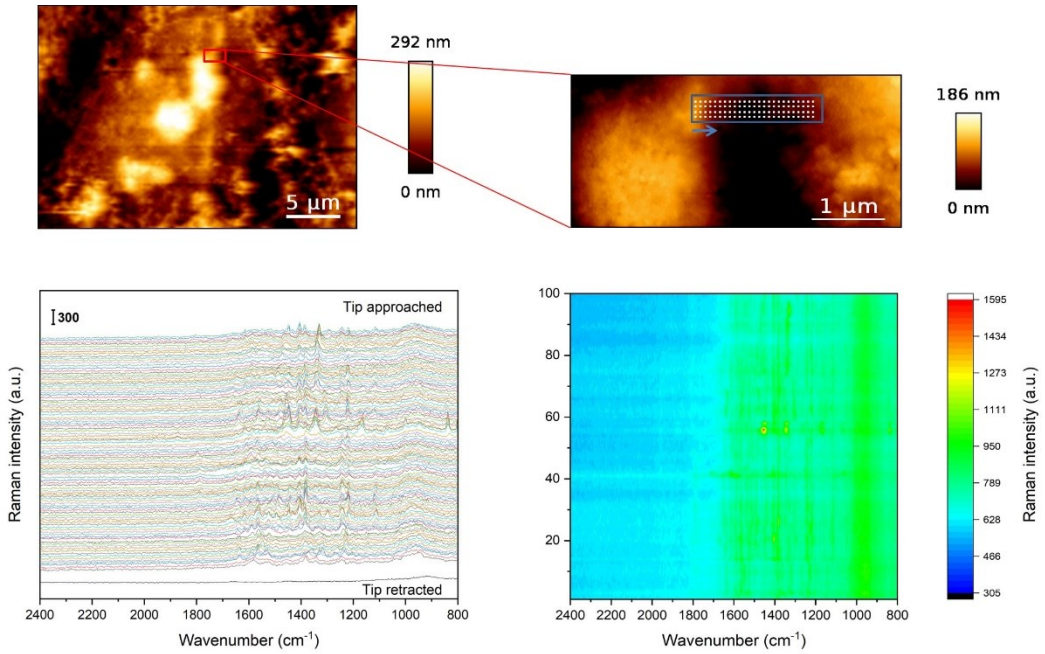

Fig. 50 Selected TERS spectra around a pore of a dried dCaL-infected cell.

Fig. 51 shows the assignment of the selected spectra. In these spectra, no bands could be assigned to lipids (region 2 and 4). In contrast, continuous amide I and amide II bands were observed. Moreover, no deuterium-related signal could be observed (region 1 and 5). In all measurements neither lipids nor dCaL were observed. It is reasonable that no characteristic lipid signals were detected due to the bilayer structure. However, the missing signal of dCaL in the measurements is unusual. In the

following a few explanations for this phenomenon will be given. First, the microplicae of cells may shield the signals from lipids. This protective protein layer on the cell makes it impossible for TERS tips to detect the distribution of dCaLs. Second, dCaLs may embed themselves into lipids, which are not exposed outside. In other words, if the side of deuterated Phenylalanine is not oriented towards the outer layer of lipids, it is impossible to find dCaLs. Finally, dCaLs may not choose a 'carpet mode' to cover the surface of lipids. Of the above-mentioned possibilities the first is the most likely. In order to confirm these assumptions, a new cell type without microplicae will be be used in the next stage.

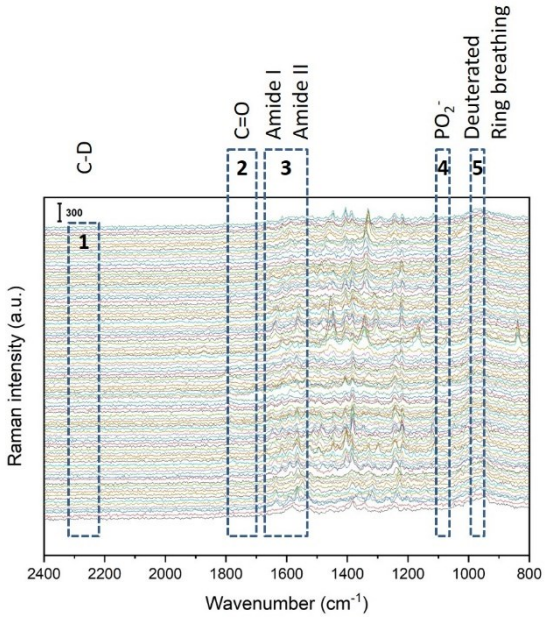

Fig. 51 The assignment of selected TERS spectra on a dCaL-infected cell. Neither deuterium signals (region 1 and 5) nor lipids signals (region 2 and 4) were detected.

4.7 Chapter summary

In this chapter, AFM and various Raman spectroscopies were introduced to study the CaL's unclear mode of action for the first time.

1. The mode of action of CaL was investigated using time-lapse AFM. Referring to experiments with Melittin, 3 different concentrations were selected and studied. Various phenomena were observed, which means that different concentrations of CaL interact with lipid molecules in different ways. Pore formations observed by Moyes *et al.* were confirmed in this expriment. Corresponding modes of action are proposed, whereof 'carpet mode' is expected to be the most likely mechanism inducing pores. However, the detailed mechanism of pore formation is still unclear.

2. To further investigate the proposed mechanisms, various Raman spectroscopies, including conventional Raman, SERS, and TERS spectroscopy were applied.

i. The first Raman measurements of CaL were conducted. The amide I band at 1662 cm^{-1} shows free CaL molecules have helical structures, which may mix with turns. A deuterium labelling strategy was used to improve the differentiation of dCaL from the background of cell membranes full of other peptides and proteins. The spectra of the mixture of dCaL and lipid vesicles show that dCaL will interact with lipids and will not completely destruct the lipid bilayer structure.

ii. The SERS spectrum of dCaL is very similar to its conventional Raman spectrum. In SERS measurements, no signals from dCaL were acquired from dCaL-infected cells.

iii. TERS measurements indicate different helical structures may exist on dCaL. on dCaLs-infected cells TERS spectra only show the existence of ordinary proteins. The signals of dCaLs could not be found on infected cells. Combined with SERS spectra, it is assumed that the microplicae of cells block the detection of dCaLs.

These presented experiments are believed to give a better understanding for researchers working on CaL-related investigations. In the next stage, the invasion of dCaL on a new type of cell without the microplicae will be explored. By localizing the distribution of dCaL on cells, the assumed modes of action of dCaL using AFM will be further clarified.

5. Investigations of SARS-CoV-2 using AFM and TERS spectroscopy

5.1 SARS-CoV-2

SARS-CoV-2 was first reported in the end of 2019[135]. By May 27th of 2021, around 169 million people were infected with SARS-CoV-2 and more than 3.5 million lives were taken by the virus. The upcoming winter in 2020 was deteriorating the situation. The record of daily reported cases in Germany from the Robert Koch Institute have reached 33,000, which indicates that the second wave is worse than the first wave in spring 2020 (see Fig. 52). A new, stricter lockdown policy had to be applied starting in the middle of December, since the soft lockdown policy from November did not help in controlling the situation. Even though the vaccinations were started from the end of December 2020, SARS-CoV-2 was rampant across the country in the first few months of 2021. Before vaccines show their effects and enough groups get immune, the valid methods are still keeping social distance and wearing face masks. Apparently, SARS-CoV-2 has dramatically changed people's daily life. The following chapter will have a closer look at the virus that has the world in its grip.

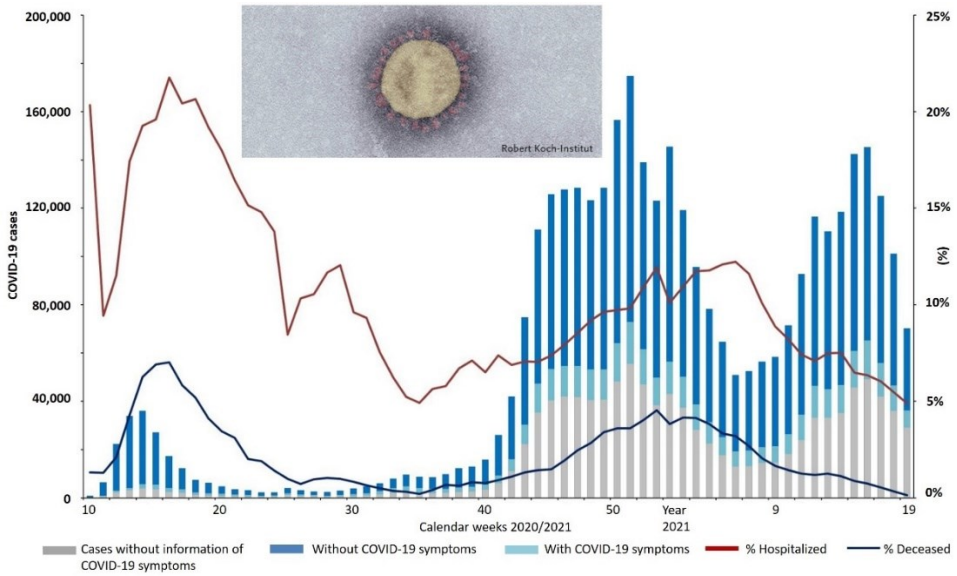

Fig. 52 COVID-19 cases with or without COVID-19-relevant symptoms and the proportion of deceased and hospitalised casesin Germany from Week10, 2020 to Week19, 2021. The inset is a TEM image of a SARS-CoV-2 virion. (Adapted from rki.de)

A virus is a special kind of organism, which can only replicate by infecting host cells[136]. Coronavirus, which got its name from its solar corona-like structural features in TEM images, is a species of ribonucleic acid (RNA) virus with 100-200 nm diameters of

spherical structures[137]. These 'corona-like' protuberances, called spike proteins, protrude from the envelope (see Fig. 53). The viral envelope protects viruses which consists of lipid membrane derived from host cells and some glycoproteins. Inside the envelope, is the viral capsid composed of nuclear proteins and RNA. This positive sense RNA expresses at least 29 proteins including the spike protein and nuclear protein[138].

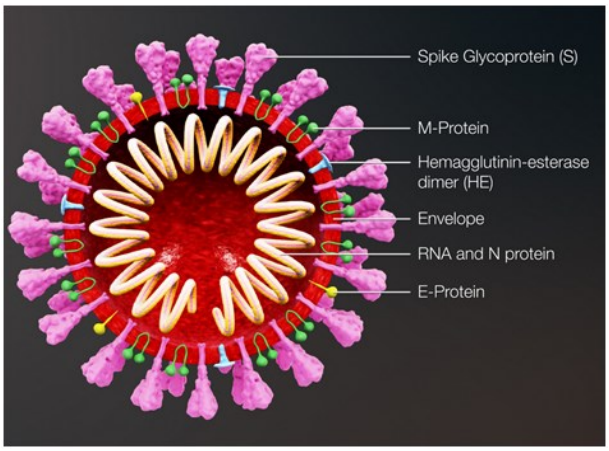

Fig. 53 A schematic diagram of coronavirus (adapted from Avijeet Ranjan, Scientificanimations.com)

Coronavirus was first recognized in the 1960s. Currently, there are 7 species in the coronavirus family, which can infect humans[139]. Some of them cause mild influenza symptoms while others are lethal (see Table 6). The coronaviruses with the highest mortality rate are SARS-CoV-1 (2002-2003), MERS (2012-today) and SARS-CoV-2 (2019-today) (see Table 7). Even though SARS-CoV-1 and MERS have higher death rates, the infection volumes are limited. Compared to SARS-CoV-1[140], SARS-CoV-2 has a stronger infectivity with a reproduction number (R_0) of 2-3[141], which means one SARS-CoV-2 patient can infect 2-3 other persons. In other words, without strict control, the infections will keep increasing and the virus will be transmitted everywhere.

Table 6 Seven known human coronaviruses

Type	Discovery year	Symptom extent
229E	1965	Common cold
OC43	1965	
HKU1	2004	
NL63	2004	
SARS-CoV-1	2002	Severe and lethal
MERS	2012	
SARS-CoV-2	2019	

The spike protein of SARS-CoV-2, which has a trimer structure mainly consisting of S1 and S2 subunits including their corresponding receptor-binding domains (RBDs), has

proven to be the key unit in virus-host cell interactions[142-144]. When a virion closes a host cell, an RBD on the spike protein in prefusion state will change its conformation from down to up and bind onto an angiotensin-converting enzyme 2 (ACE2) of human cell, following the cleavage of S1 subunit from S2 and then the conformation of S2 subunit changes into the postfusion state. Such an S2 structure will facilitate the fusion of viral and cell membrane and the following viral entry.[145-148] In this way, the spike protein mediates the entry of virial genetic material into the host cell. As a result, spike proteins become one of the main research objects for the development of vaccines and clinical therapies. The spike protein of SARS-CoV-2 is found to show a higher affinity to ACE2 than the one of SARS-CoV-1[24, 149]. Compared to SARS-CoV-1, the spike protein of SARS-CoV-2 has a more compact conformation and different residues strengthen the RBD-ACE2 interaction[149]. Above-mentioned experiments give a hint to why SARS-CoV-2 has a stronger contagiousness than SARS-CoV-1. Additionally, it was reported that the antibodies of SARS-CoV-1 cannot effectively bind with the spike protein of SARS-CoV-2[24].

Table 7 Overview of SARS-CoV-1, MERS, and SARS-CoV-2 (data from WHO.int)

	SARS-CoV-1	MERS	SARS-CoV-2
Period	2002-2003	2012-Jan.2020	2019-May.2021
Reported cases	8422	2519	>169 million
Reported deaths	916	866	>3.5 million
Death rate	11%	34%	2.1%
Distributions	29 countries	27 countries	Worldwide
Vaccine	No	No	Yes

The diagnosis of SARS-CoV-2 is a very important step. At the onset, the symptoms of SARS-CoV-2 patients are similar to a common cold; however, around 40% of infected persons are asymptomatic while being infectious[150, 151]. Thus, any misdiagnosis will put other healthy persons into risks. Nevertheless, time, cost, and accuracy of detection must be carefully balanced. For a detection technique, the accuracy can also be expressed by sensitivity and specificity. The sensitivity shows the proportion of true positives which indicates the rate of false negative while the specificity measures the proportion of true negatives which indicates the rate of false positive. Both the false negative and the false positive rates affect the accuracy[152]. At present, two main detections are used in diagnosis: detecting antibodies and RNA. The colloidal gold-based immunochromatographic assay is broadly used in the rapid detection of toxins, diseases, food science, *etc*.[153-155]. By detecting the antibody immunoglobulin M (IgM),

this assay will provide results within tens of minutes. The sensitivity and specificity of this method for SARS-CoV-2 is 71.1% and 96.2%, respectively[156]. However, it must be noted that IgM is secreted 3-5 days after the infection, which highly affects the detection sensitivity of antibody test. Another common detection method is reverse transcription polymerase chain reaction (RT-PCR), which detects the virus' RNA[157]. In contrast to the antibody detection method, a PCR test can be conducted at the onset of infection. In an RT-PCR test, RNA is first transcripted into a more stable complementary deoxyribonucleic acide (DNA). The target fragments are recognized by specific primers and then extended. By analyzing the fluorescence intensity of probes, the viral RNA can be recognized and defined. Normally, a test is finished in about 1-1.5 hours. Depending on the detection targets and the designation of primers, the sensitivity and specificity are 60%-98% and 95%-100%, respectively[158, 159]. Additionally, a multiplex analysis is possible for RT-PCR.

From the above-mentioned data, it was found that the sensitivity (i.e., the false negative rate) presents an issue for the detection of SARS-CoV-2. Even if all detections can reach an ideal sensitivity of 98%, there are still more than 3.4 million of misdiagnosed positive cases in the world (calculated from the data in Table 7). Additionally, the emergence of new variants makes the situation worse and may decrease the accuracy of current detections. Therefore, the rapid detection results are often combined with clinical symptoms and/or other complementary detections. For example, TEM is the most convincing technique to study the topography of this virus. However, it is unsuitable to use a TEM instrument for a rapid test. Regarding the accuracy and performance-to-value ratio of the detections, further knowledge is required, and other methods need to be explored in the study and detection of SARS-CoV-2. With its few special requirements for sample preparation and working environment AFM is a suitable method. In addition to topographical imaging, AFM can also measure the mechanic information of samples. After combining a Raman spectrometer and plasmonic nanoparticles, AFM becomes a TERS setup, which can further investigate the chemical compositions of samples at the nanoscale. In this chapter, AFM-TERS spectroscopy is for the first time used to investigate SARS-CoV-2.

5.2 Experiments

Sample preparation

The inactivated SARS-CoV-2 virus (Batch No.: vi5587) was ethically and legally obtained from a patient at Universitätsklinikum Jena (UKJ) and was further cultured in Vero76 cells (green monkey kidney cells) in the BSL3 lab of UKJ. Samples were purified

with 200 µm filters. The concentration of the virus was 10^8/mL ($TCID_{50}$). 400 µL 4% formaldehyde (PFA) were added to 100 µL virus solution and incubated 30 min at 37 °C to inactivate the virus. The mixture was then vortexed and centrifuged at 14,000 rpm for 10 min. The supernatant was removed and 500 µL PBS (or dH_2O) were added to wash the virus sample, which was then further centrifuged at 14,000 rpm for 10 min. After the removal of the supernatant, the virus sample was resuspended in 100 µL PBS (or dH_2O). The PFA inactivation method has been confirmed as valid and the sample was confirmed to be save for experiments in ordinary labs by UKJ. In each measurement, 1.5 µL virus solution were dried directly on a piranha solution-cleaned coverslip. The dried virus samples were then used in the following measurements.

AFM imaging and force measurements

AFM imaging was conducted with an intermittent (tapping) mode under ambient conditions. The AFM tip, Tap190 Al-G, which was used in AFM imaging, has a frequency at around 160 kHz with a spring constant at around 30 N/m. The images were acquired with 256x256 pixels.

Force measurements were conducted using the QI mode of the JPK Nanowizard Ultra Speed. The AFM tip NSC14 was used in the measurements and setpoints were placed from 0.8-10.4 nN. Approaching duration varied from 3.9 to 7.9 ms depending on the specific measurements. The pixels of images were 256x256 on virions and 512x512 on PFA. Adhesion and Young's modulus were extracted using JPKSPM Data Processing software. The smoothing method and width are Gaussian and 3.00, respectively. Hertz/Sneddon was the used model to extract mechanic information. The adhesion and Young's modulus data were further processed using Gwyddion. Fig. 54 shows the detailed steps. First, the values of background and virions/PFA were extracted separately by watershed masks. The total area was normalized to 1 following Eq.3. ρ and p are the normalized frequency and the Adhesion/Young's modulus at each position.

$$\int_{-\infty}^{\infty} \rho(p)dp = 1 \qquad \text{Eq. 3}$$

Second, the obtained histogram data were smoothed by a Savitzky-Golay filter or Adjacent-Averaging. Third, the smoothed data were further fitted by non-linear fitting (Gaussian model) to extract the peak value and the full width at half maximum (FWHM). Finally, the main fitting peaks of these values were presented in boxplots and other graphs.

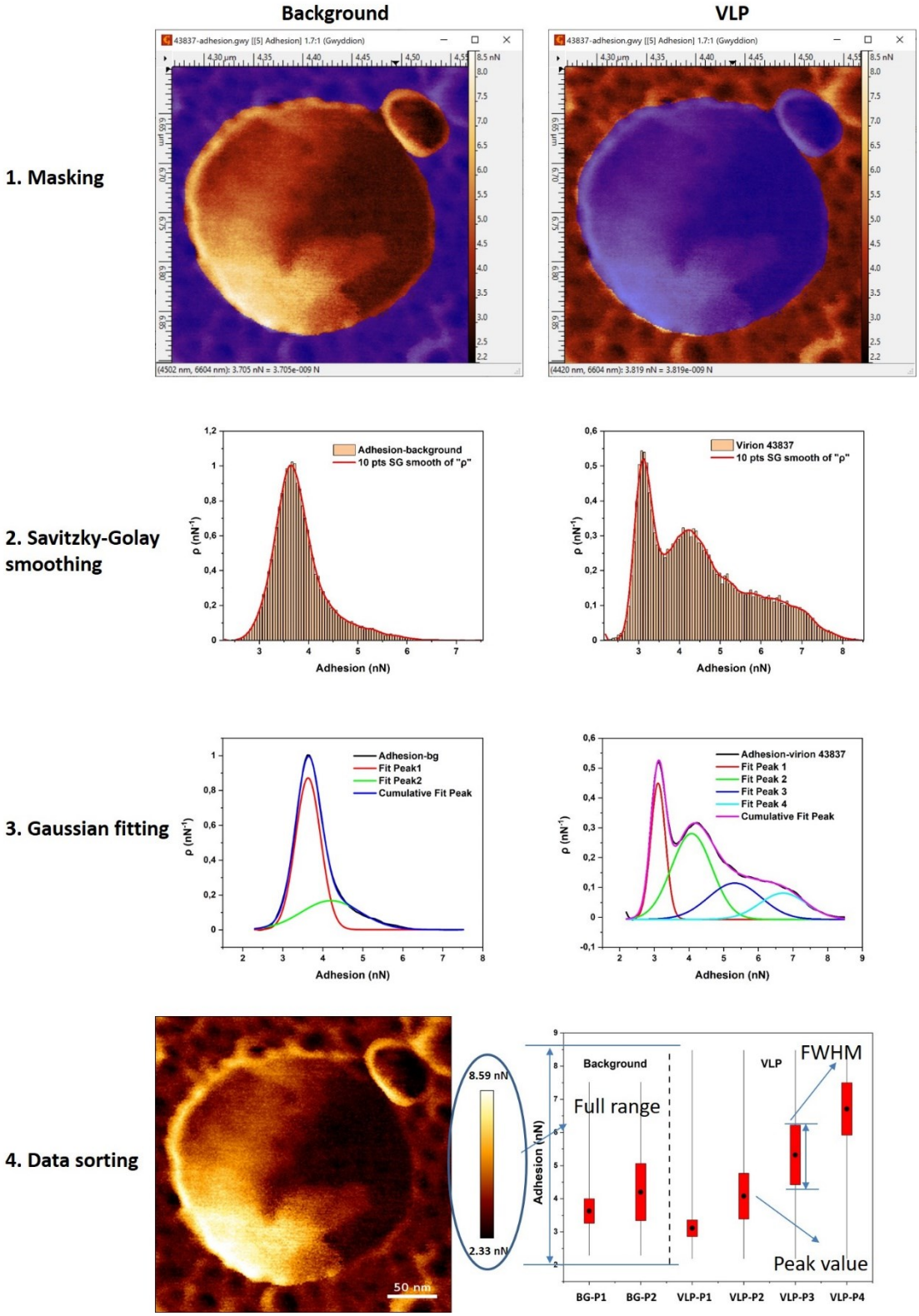

Fig. 54 Data processing of force measurements. 1. Masks were made on the target region to extract the force data; 2-3. The extracted data were treated by smoothing and Gaussian fitting using Origin; 4. The peak value and the force scale of each target were presented and compared in the candle chart. Here, VLP refers to virus-like particle.

Conventional Raman, SERS and TERS measurements

Our TERS setup is a combination of AFM and a Raman spectrometer, which can also be used for independent measurements of conventional Raman and SERS spectroscopy. An inverted microscope system is used as the working stage of the AFM head in which a 60x oil lens with a 1.45 NA (Nikon) was used. For this experiment, the light source is a 532 nm green laser. Depending on the specified experiments, the output power was set at around 100 µW-10 mW with an exposure time of 1-10 s and accumulations up to 300. Conventional Raman measurements were conducted on cleaned coverslips while SERS measurements were conducted on Cr3Ag6 SERS substrates. 25 nm Ag films were manufactured on Tap190 Al-G AFM tips which were then annealed. 8x8 or 10x10 grids were set to acquire signals from single targets, which were then confirmed as virions. The step sizes varied with the measured scales on each virion. Control Raman signals were acquired when tips were retracted from the sample surface. Spectra presented here were treated by OriginPro 2020b without baseline corrections.

5.3 Topographic and mechanic information on SARS-CoV-2

5.3.1 Topographies of SARS-CoV-2 virions

SARS-CoV-2 virions exhibit diameters around 80-120 nm in TEM images[23]. However, the high vacuum condition of TEM may compress the sizes of virions. Thus, the dimensions of natural virions are supposed be larger. Also, TEM cannot give height information on virions. Without regard to spatial resolution, AFM makes it easier to acquire topographic information during experiments.

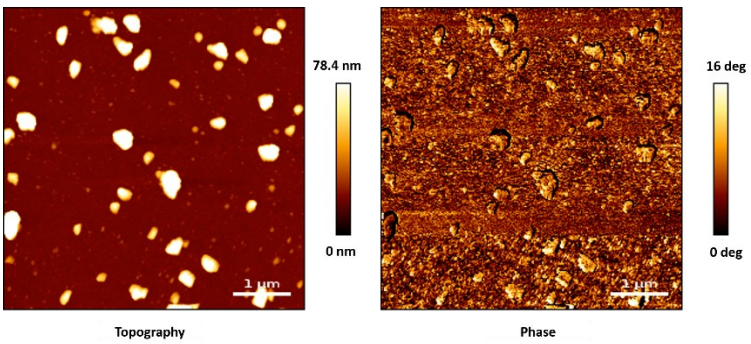

Fig. 55 AFM images of a SARS-CoV-2 virus sample in a scale of 5x5 µm^2 which were cultured in Vero76 cells.

Fig. 55 shows AFM images of a SARS-CoV-2 virus sample. At a random position with a

scale of ~5x5 µm^2, matters in various sizes up to 500 nm were found. Sometimes larger objects could also be observed. Even though the virus sample was purified, some components like fragments of cell debris and chemicals are unavoidable. Nevertheless, fluorescence-correlation experiments performed by my colleague Dr. Tanja Deckert-Gaudig confirm the existence of virions in these virus samples. Based on the TEM reference, above-mentioned contaminations in the viral sample following their sizes are divided into 3 groups: smaller than 50 nm, between 50-300 nm, and larger than 300 nm. Particles smaller than 50 nm refer mostly to the culture base while those larger than 300 nm could be cell residues or virus aggregates which are crosslinked by PFA. A loose screening criterion can make sure that most of the possible virions can be included. In this chapter, objects which meet the vrial screening criterion are conservatively defined as virus-like particles including virions and virus-like vesicles. Among these, virus-like vesicles are viral envelopes without capsids and viral genomes. From AFM topographical images, it is impossible to distinguish them. However, the antigen properties of these vesicles should not be ignored.

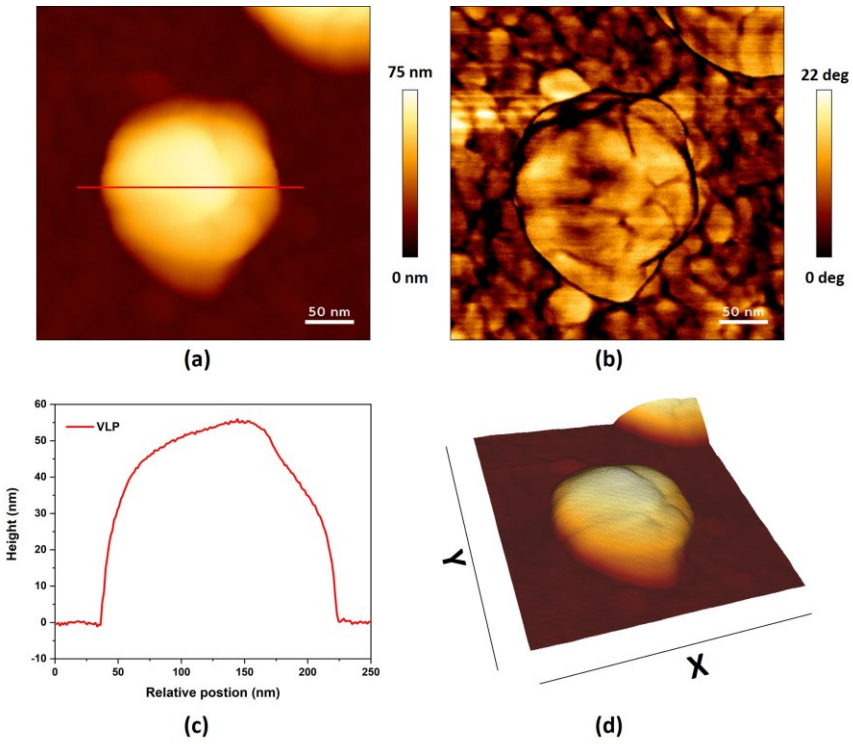

Fig. 56 AFM images of a virus-like particle. (a) Topography image; (b) Phase image; (c) A profile on the virus; (d) 3D image.

Fig. 56 shows the AFM images of a virus-like particle. This particle has a spherical shape with a diameter of 180 nm and a height of 55 nm (Fig. 56c). Compared to data from TEM images, this particle is larger but still in a reasonable size. Normally, Cryo-TEM is conducted under a high vacuum condition with a liquid nitrogen temperature (-196 °C/ 77 K) and virions may shrink under such extreme conditions. In contrast, AFM is

normally operated under ambient conditions and maintains the original structural features of virions. Additionally, more surface details can be obtained from the AFM phase image (Fig. 56b). Due to flattening and broadening effects on the substrate, the height of this virus-like particle is only 30 % of its dimension. Furthermore, the dehydration process of virions in ambient conditions is thought to be another factor causing the low height of the virus like particle.

Even though virions are expected to exist in nice spherical structures, the crosslinker PFA reshaped these virus-like particles. Often a particle was seen to be combined with some residues. Based on above-mentioned diameter and height, a few particles were screened. Fig. 57 shows some selected virus-like-particles.

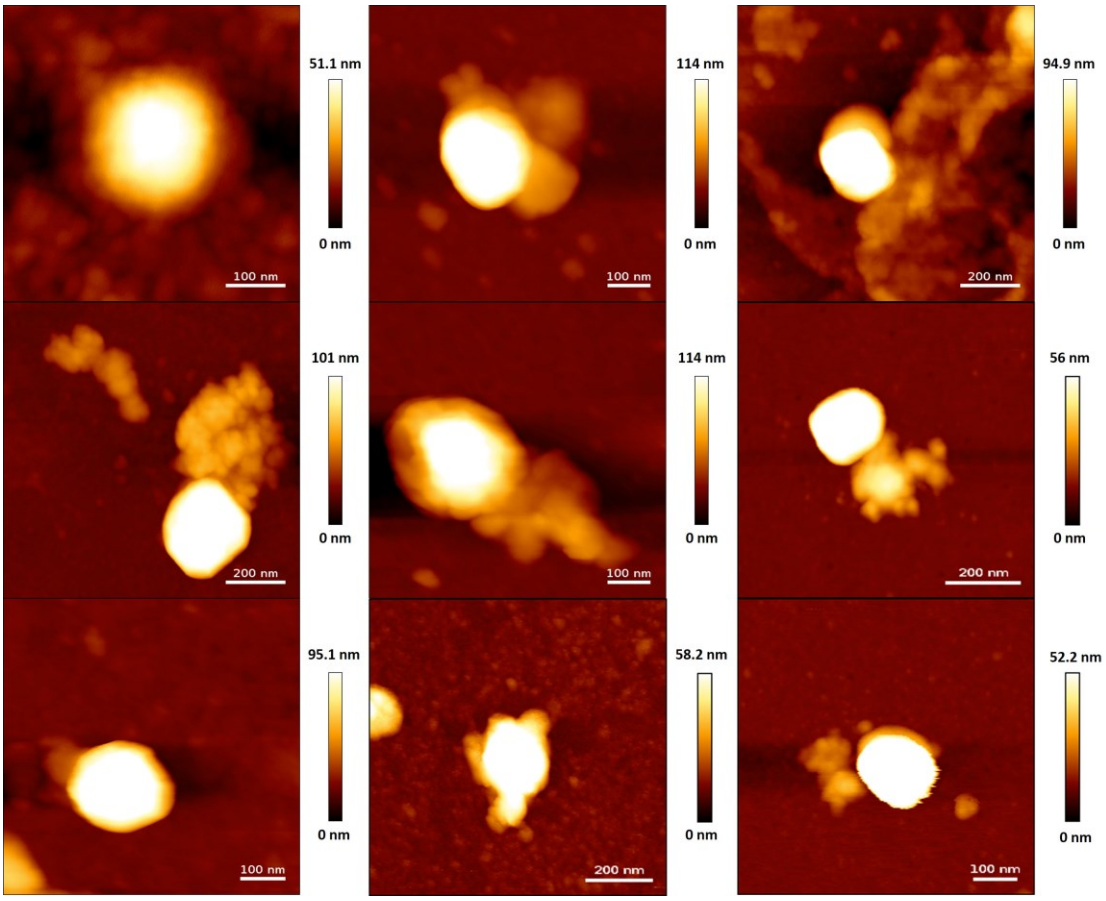

Fig. 57 AFM images of 9 selected virus-like particles in different sizes and topographies.

Limited by the dimension and the convolution effect of the AFM tips used, the lateral resolution is different from TEM experiments. For instance, it is nearly impossible to see spikes on the surface of targets using AFM. Therefore, it is difficult to distinguish virions from the complex sample full of cell debris and chemicals. However, in contrast to SEM/TEM the absolute height of the structures is determined with Ångström precison and is independent of the tip shape. Consequently, the height will be mainly used as an identification parameter. Apart from the fragments of cell debris in

micrometer dimensions, chemicals for cell culturing and virus inactivation may also affect the imaging. In Fig. 58 there are several tiny spherical targets with diameters around 20-30 nm which are expected to be BSA or PFA. To further improve the reliabilities of the screening criterion, some control measurements were conducted to investigate/confirm the topography of BSA and PFA.

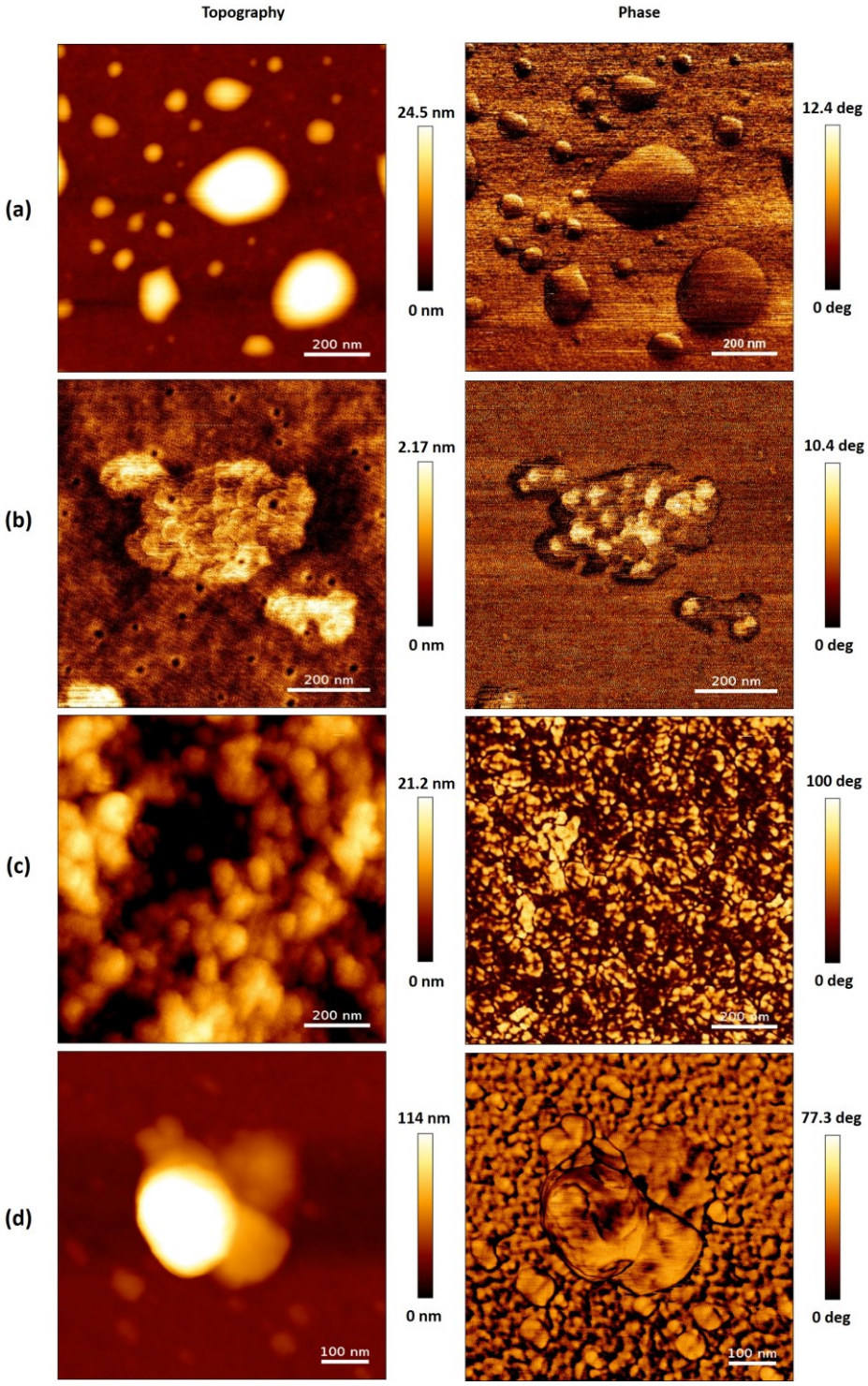

Fig. 58 AFM images of different materials. (a) Some PFAs show similar topographies and

dimensions to virus like particles; (b) Pure BSA samples have very low height which will not affect the AFM imaging; (c) PFA-BSA mixtures show well distributed golobular structures with the dimension of 20-30 nm, and (d) A virus-like particle which is combined by unknown materials.

Some spherical PFA aggregates similar to virus-like particles could be observed from a dried PFA (4%) sample (Fig. 58a). Those PFA aggregates with diameters comparable to virus-like particles have heights of around 30 nm, which is lower than the heights of virus-like particles. Even though most PFA aggregates are different from virus-like particles, the possibility of confusing them should be considered. The second possibility of confusion in the detection of virus-like particles is presented by minute spherical targets in the background. Pure BSA aggregates do not have spherical structures and their heights are only around 2 nm (Fig. 58b). However, after BSA and PFA were incubated together, some spherical structures (Fig. 58c) are observed which show similar dimensions to the background of the virus sample (Fig. 58d). It is supposed that the crosslink effect of PFA could strongly change the topography of small peptides. Based on this result, it is suggested that those spherical structures in the background are small peptide-PFA complexes, like PFA-BSA complexes.

Additionally, a cell medium sample without the virus was used as further control sample. In Fig. 59, many matters of different sizes could be found while none match the size of virus-like particles. This further supports our screening criterion indicating the large spherical objects in the virus sample should be virions or vesicles. Still at this stage we consider them as virus-like particles.

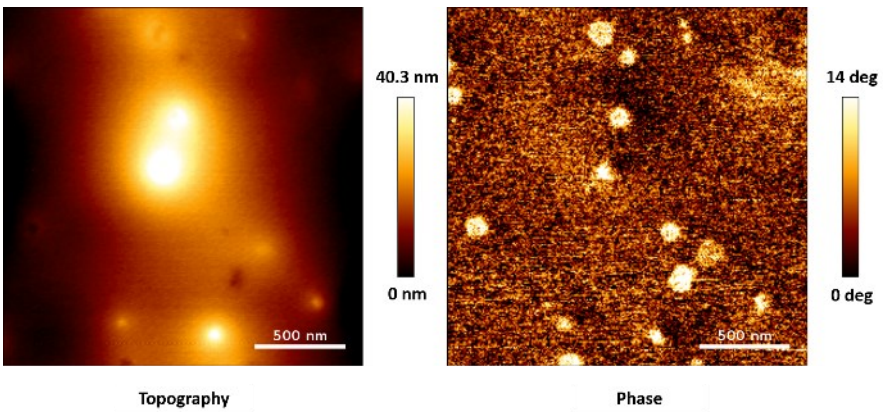

Fig. 59 AFM images of a cell medium sample. No objects look like virus-like particles. The light spots in phase images are from the defects of glass slides.

Based on a straightforward virus culturing protocol and a suitable screening strategy, it is supposed that AFM can recognize SARS-CoV-2 particles. Even though some impurities may affect the recognition, with a good cross verification of height and dimension, virus-like particles will not be missed in AFM measurements.

5.3.2 Mechanic information on SARS-CoV-2

Mechanobiology investigates the mechanic responses, and respective life processes, of biomaterials (ranging from nuclear acids, proteins, to organisms) to external forces[160]. Every group of biomaterial has various mechanic information[161-164]. Generally, adhesion, tension, friction, and torsion, etc. are studied in mechanobiology. Some mechanic information can also indicate structural differences of targets. Therefore, mechanic information can be used as a complementary support in analysing and distinguishing different materials.

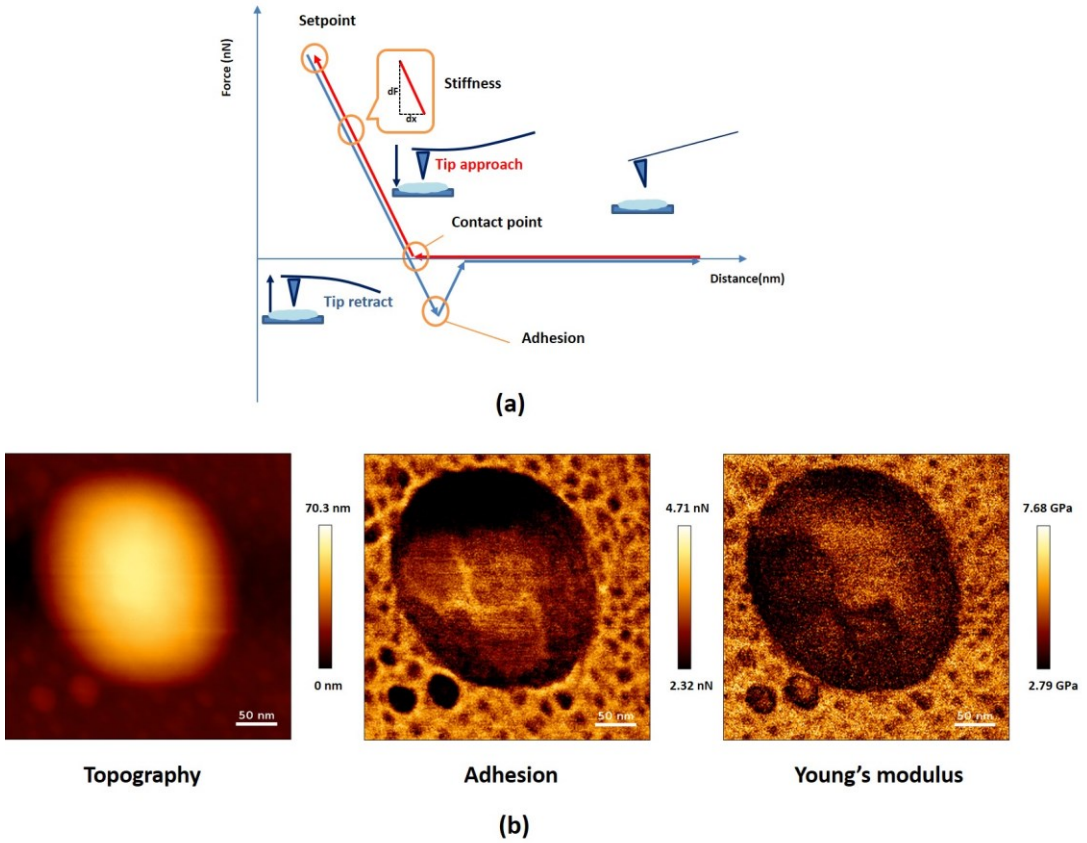

Fig. 60 (a) Force-distance curve of AFM and (b) Topography, adhesion, and Young's modulus map of a virus-like particle.

AFM is often used in mechanic research as it can acquire topographic and mechanic information simultaneously. During a force measurement, an AFM tip is pressed onto the surface of a sample and then retracted again. During this process, a force-distance curve reflecting the mechanical information of the sample is recorded (Fig. 60a). Usually, adhesion and Young's modulus in an AFM force measurement are extracted from the force-distance curve. Adhesion shows the stickiness of a sample, which is the lowest point on the retraction curve while Young's modulus reports the stiffness of the sample which is calculated from the slope of the approach curve. Every approach and retraction will give a set of adhesion and Young's modulus, which will form into the

corresponding force maps after a continuous force measurement (Fig. 60b). The viscoelasticity of a material is often unique. In the following experiment, the mechanic information of SARS-CoV-2 is explored in order to distinguish it from PFA as both have similar topographies.

5.3.2.1 Differentiation of SARS-CoV-2 and PFA

Even though virus-like particles and PFA have similar spherical topographies, their height difference is enough to distinguish them (Fig. 61). However, to exclude the possible misinterpretations and to show their mechanic difference, the mechanic information of a virus-like particle and PFA is compared.

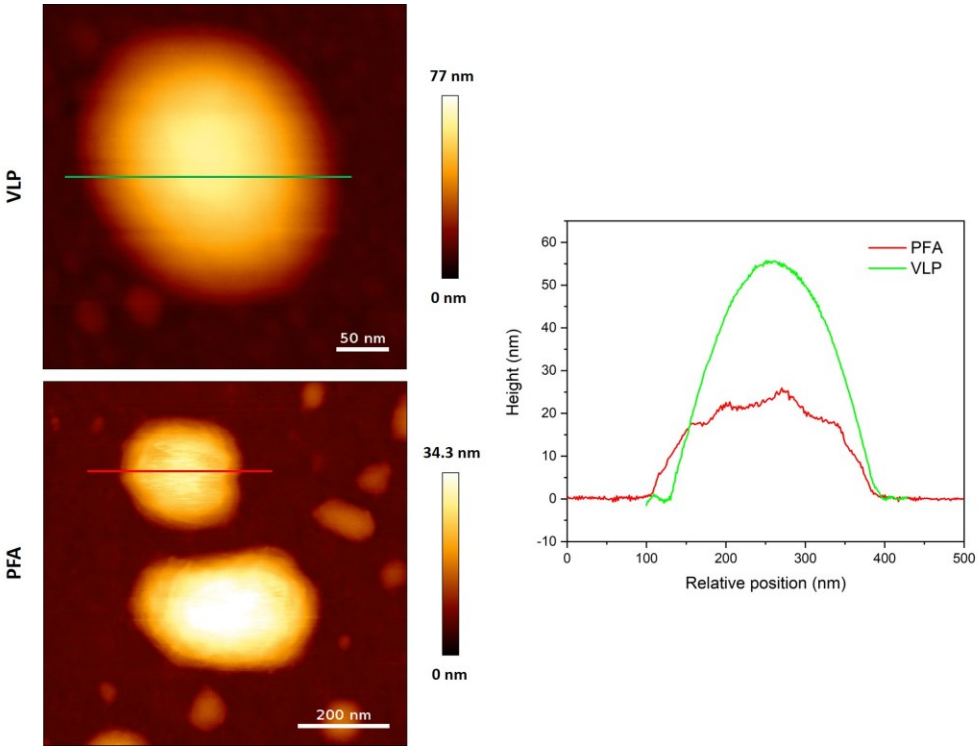

Fig. 61 Topography images of a virus-like particle and PFA aggregates and profiles at two specified positions. VLP refers to virus-like particle.

Adhesion and Young's modulus come from the force responses of the sample. Both chemical composition and molecular orientation will affect these parameters. Meanwhile, tip effect should be seriously concerned in force measurements. Tips with different force constants and shapes affect the values. Normally, different types of tips are incomparable in force measurements. In addition to the setpoint, it has also been proven that the loading rate (loading force per second, N/s) significantly influences the measurements[160]. Thus, the prerequisite condition for a quantitative comparison of force measurements is the same type of tip with the same setpoint and loading rate.

Fig. 62 shows the adhesion and Young's modulus map and their statistical distributions of a PFA sample. Fig. 62a depicts the adhesions of different targets. Large PFA aggregates show a value similar to the background while small PFA aggregates are stickier. Generally, the PFAs show very similar adhesion values. In contrast, the Young's moduli are obviously different (Fig. 62b). Large PFA aggregates are softer than the background and small aggregates.

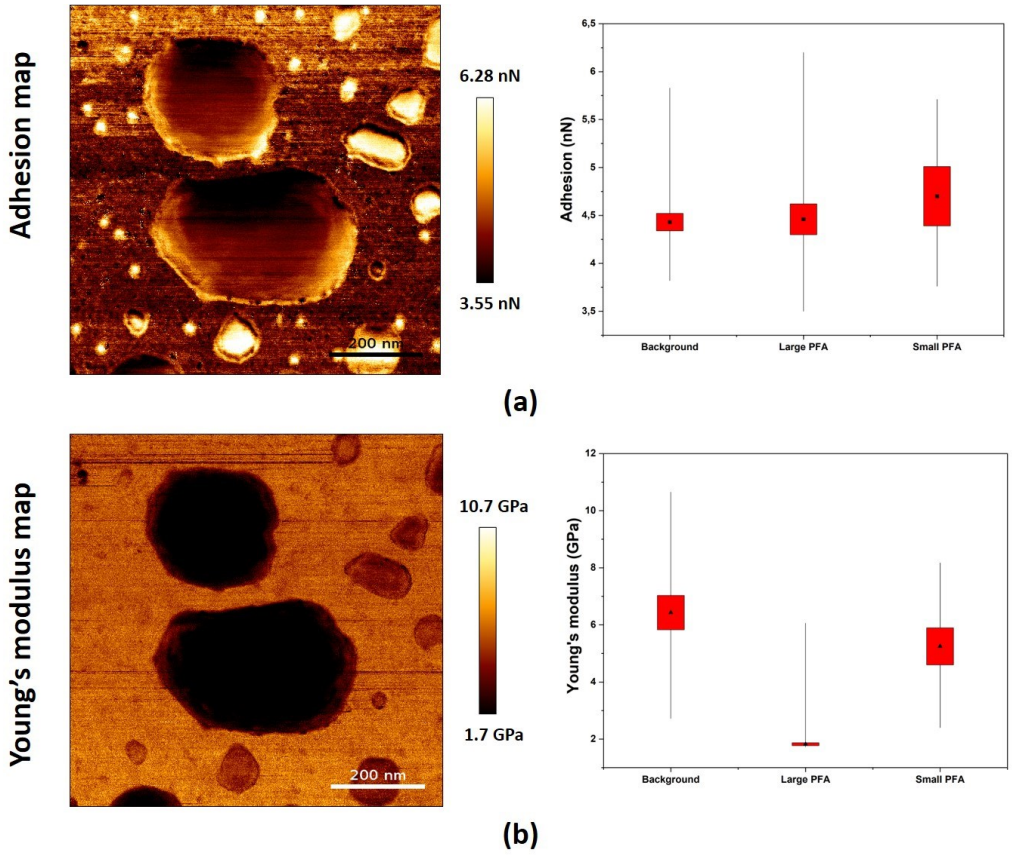

Fig. 62 Adhesion (a) and Young's modulus (b) maps of a PFA sample and their relative distributions

Already for PFA, commonly considered as a homogeneous sample, it is found that the adhesions vary with the dimensions of PFA aggregates, which means the adehesion is not just related to the chemical compositions. It is supposed that on a virus sample with complex compositions its adhesion distribution will be even more complex. Fig. 63 shows the adhesion and Young's modulus maps of a virus-like particle (VLP44766). The adhesion map of the background splits into two different groups, which shows the complex composition of this virus sample. However, the adhesion distribution shows that the surface components are quite similar and some regions of the virus-like particle are less sticky than its background. Different biomaterials vary in their adhesions. On cell membranes, commonly, proteins expose more polar bonds than lipids. Thus, it is hypothesized that, except of dimension issues, the lipid compositions

upon the virus-like particle in Fig. 63 may be the origin of less adhesion when it is compared to the background, which normally does not have lipids. In contrast, the Young's modulus distribution indicates that this virus-like particle is softer than its background.

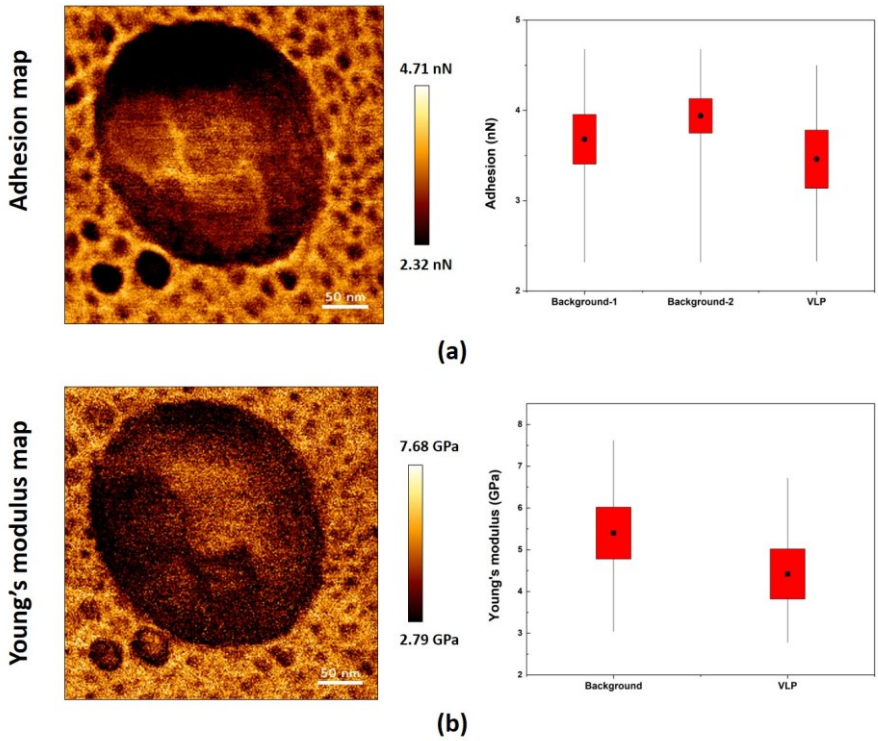

Fig. 63 Adhesion and Young's modulus maps of a virus-like particle and their relative distributions. This particle has smaller Young's modulus than the background while its adhesion closes to the background.

The two cases (Fig. 62 and Fig. 63) mentioned above were measured using the same tip (NSC14), setpoint (2 nN), and loading rate (0.5 µN/s). Thus, they can be directly compared (see Fig. 64). Even though only large PFA aggregates have similar dimensions like the virus-like particles, also small PFA aggregates are compared. The scale of adhesion and Young's moduli of these groups overlap each other. However, their main distribution regions provide a trend. It is found that this virus-like particle (Fig. 63) has a smaller adhesion and a higher Young's modulus when compared to large PFA aggregates (Fig. 64a). In contrast, smaller PFA aggregates have a higher Young's modulus than this virus-like particle. In other words, this virus-like particle is less sticky than the PFAs and has a medium stiffness. Furthermore, the distribution of Young's modulus as a function of relative adhesion at the same position was extracted which includes around 1000 sets of data in each group. Even though these targets overlap on the scales of their adhesions and Young's moduli, their adhesion-Young's modulus correlation shows their difference. Fig. 64b indicates that this virus-like particle can be distinguished from these PFAs.

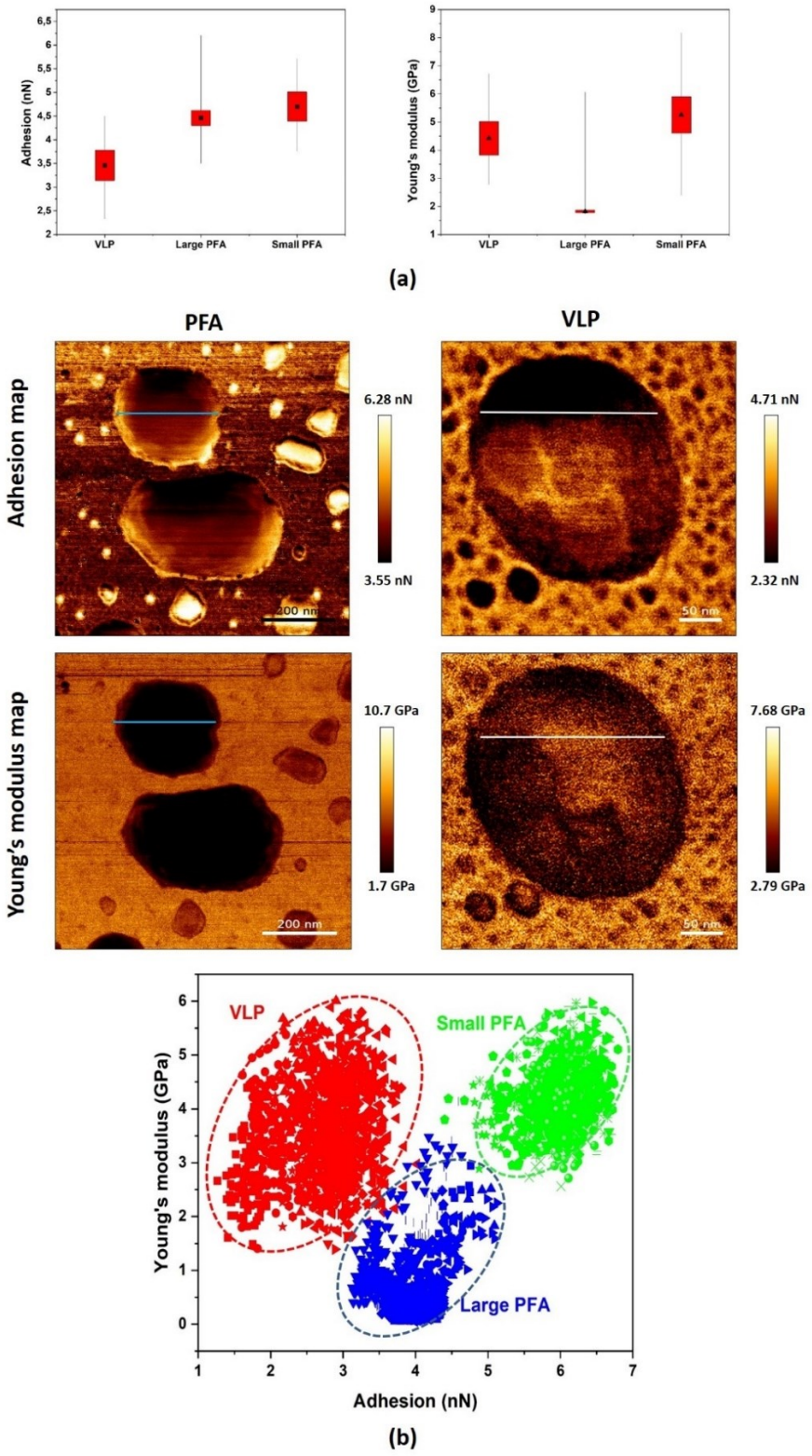

Fig. 64 (a) Comparison of a virus-like particle and different PFA aggregates and (b) The distribution of Young's (elastic) modulus as a function of adhesion of different targets. VLP referes to virus-like particle.

5.3.2.2 Differentiation of virions and virus-like vesicles

First of all, the reliability of measurements was analysed. 3 different setpoints — 0.8

nN, 2 nN, and 5 nN — on the same virus-like particle were conducted (Fig. 65). These force maps are very similar, which means 5 nN is still safe to do a reliable measurement on virus-like particles. Moreover, possible arbitrary or artificial errors could be excluded.

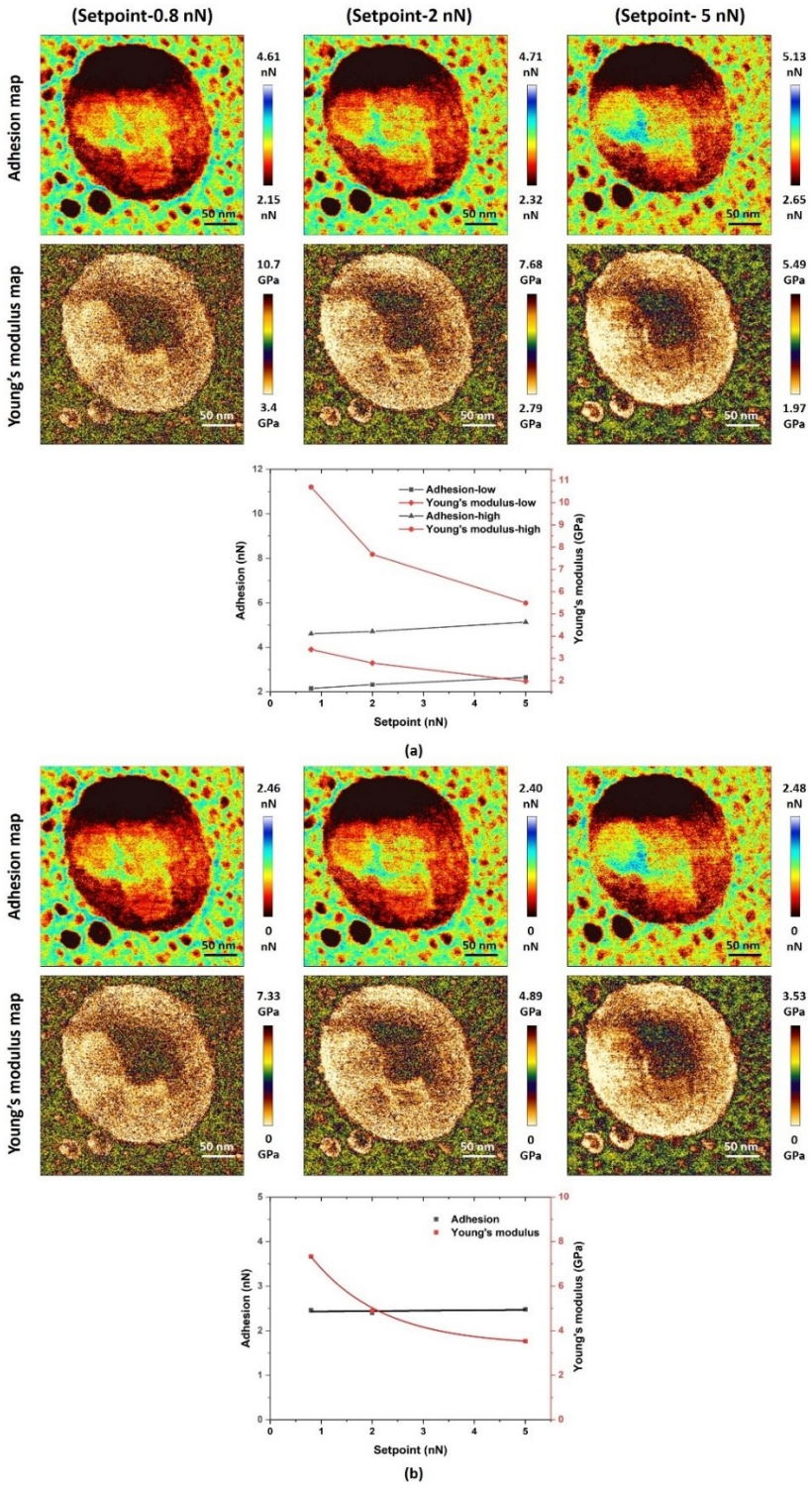

Fig. 65 Force measurements of the same virion with 3 different setpoints. (a) absolute scales of adhesion and Young's modulus maps; (b) relative scales of adhesion and Young's modulus maps and their comparison.

Fig. 65a confirms that different setpoints will change the values of adhesion and Young's modulus. Thus, a direct comparison among force measurements using different parameters is not possible. However, when the scales are converted to relative values, a scheme emerges. Fig. 65b shows that the absolute adhesions increased while the relative adhesion ranges of 3 measurements remain almost the same. A higher setpoint means a deeper indentation. During the indentation, more molecules will interact with the tip and the adhesion will increase. It is assumed that (i.) the adhesion could be linearly related to the tip and the virus-like particle within small scales in which the tip shape and the chemical compositions do not dramatically change; (ii.) the tip was working in a relatively homogeneous region. In other words, the indentation range is in the envelope because the capsid has a different composition.

In contrast to adhesion, increasing the setpoint decreased both the relative and absolute values of Young's modulus in the measurements. The Young's moduli of the measurements show an exponential variation, which means there are additional forces responding to different structures. Additionally, there is a core-like region in each Young's modulus map. The structure of a virion can be generally divided into two parts — envelope and capsid. The viral envelope originates from human cells, which are only 7-10 nm thick. For the 1-2 nm indentations, the influence of the capsid cannot be ignored. Therefore, it is assumed that the core-like region in a Young's modulus map is most likely caused by the capsid of the virion.

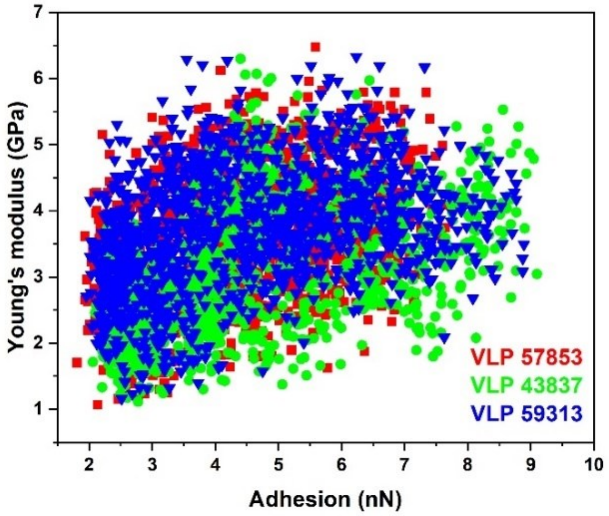

Fig. 66 Distributions of Young's moduli versus adhesions of 3 virus-like particles which show that the mechanical properties of these particles under the experimental setting were close to each other.

Based on the correlation between Young's modulus and adhesion, virus-like particles can be distinguished from PFA aggregates. However, it is difficult to identify the differences of these values among virus-like particles. The distributions in Fig. 66 show little difference among 3 virus-like particles, which were measured at a setpoint of 3.4 nN and the same loading rate. The high similarity of virions and vesicles in their structures and compositions results in the overlapping adhesion-Young's modulus distributions. Remarkably, compared to topography images, their corresponding adhesion and Young's modulus maps, provide a better image contrast (Fig. 67).

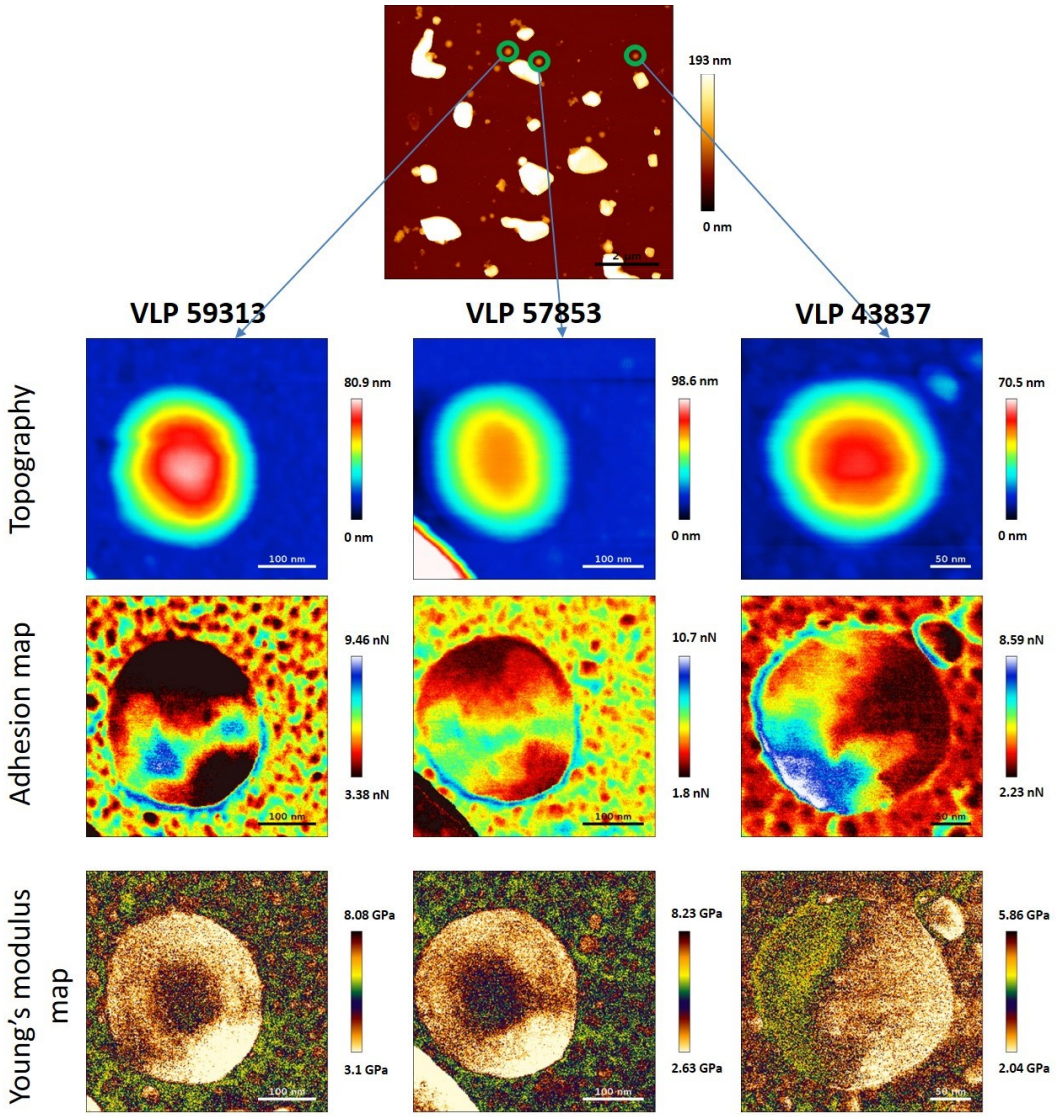

Fig. 67 Comparison of 3 virus-like particles concerning their topographies, adhesion, and Young's modulus maps. The topograhphy images and the adhesion maps of these 3 particles are similar while the Young's moudulus maps of VLP59313 and VLP57853 show core regions which are clear different to the one of VLP43837.

Conventional AFM images can only show the surface topography of a target while adhesion maps can show the interaction difference at each spot on the target and Young's modulus maps can even indicate their structural difference. Adhesion maps

are highly influenced by sample components. The viral sample used in this experiment is PFA-inactivated and may contain other peptides or compositions that have been crosslinked with PFA during the inactivation process. Thus, the adhesion maps shown in Fig. 67 look irregular. Normally, a more homogeneous distribution is expected from them. In contrast, a distinct characteristic in the Young's modulus map attracts attention. In the Young's modulus maps of VLP57853 and VLP59313, there are harder core-like regions similar to the Young's modulus map in Fig. 65 while VLP43837 does not have such a feature. Combined with above results, it can be assumed that VLP57853 and VLP59313 are virions, while VLP43837 should be a vesicle.

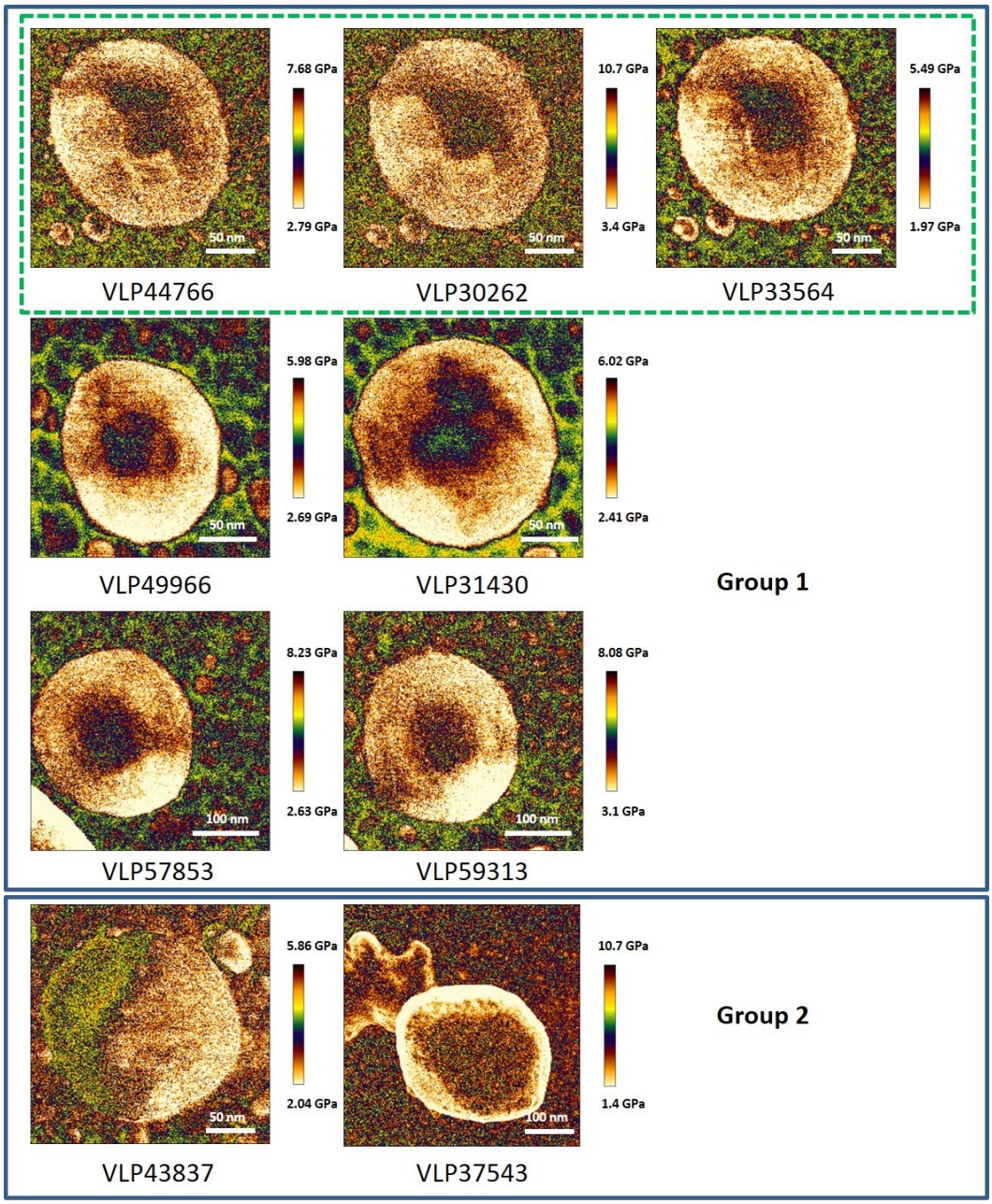

Fig. 68 Comparison of Young's modulus maps of different virus-like particles. The virus-like particles in group 2 are clear different to those in group 1 which do not have the core region.

Table 8 Ratios of hard core to soft part in Young's modulus maps of virus-like particles

Virus-like particles			Young's modulus (GPa)		Ratio (Y_{hard}:Y_{soft})	Average	Category
			Y_{hard}	Y_{soft}			
Group 1	1	VLP44766	5.08	4.38	1.16	1.15±0.02	Virion
		VLP30262 (same particle to 44766)	5.85	5.10	1.15		
		VLP33564 (same particle to 44766)	3.30	2.94	1.12		
	2	VLP31430	4.47	3.80	1.18		
	3	VLP49966	4.57	3.95	1.16		
	4	VLP57853	5.03	4.35	1.16		
	5	VLP59313	5.53	4.88	1.13		
Group 2	6	VLP37543	2.63	1.85	1.42	-	Vesicle
	7	VLP43837	4.08	3.22	1.27		

Of 7 different virus-like particles, measured under different parameters, there are 5 particles exhibiting this core feature (Fig. 68). In a further analysis, it was found that the ratios of hard to soft part of these virus-like particles are around 1.15 (Table 8). In contrast, the ratios of VLP43837 and VLP37543 are 1.27 and 1.42, respectively. Therefore, the first 5 particless are categorized as virions while the other two are more likely to be vesicles. In fact, this conclusion is supported by the fluorescence correlation works from my colleague Dr. Deckert-Gaudig. By labelling proteins and nucleic acids, virions and vesicles are easily recognized and distinguished. In post-measurements of these labelled particles, they actually show the same features and regulations of this experiment. Furthermore, such a ratio (Y_{hard}:Y_{soft}) is expected to be used as reference in the differentiation of various viruses. More experiments are currently in process.

Force measurements provide better contrasts than the conventional AFM imaging mode. Compositional and structural difference of samples could be indicated by their relative adhesion and Young's modulus maps. In adhesion-correlated Young's modulus distributions, PFA aggregates are easily distinguished from virus-like particles. Furthermore, virions and vesicles are distinguished based on their structural difference presented in Young's modulus maps.

5.4 Raman spectra of SARS-CoV-2

5.4.1 Conventional Raman and SERS measurements

To chemically investigate SARS-CoV-2, Raman spectroscopy, including conventional Raman, SERS, and TERS spectroscopy, was applied. Fig. 69a shows AFM-correlated conventional Raman spectra. A virus-like particle was recognized by AFM first (the inlet of Fig. 69a), then an AFM-correlated Raman spectrum of this virus-like particle was acquired under 1 mW laser. However, conventional Raman spectroscopy cannot detect the signal of a single virus-like particle due to the limit of low Raman cross-sections of the virus-like particle. Therefore, enhanced Raman spectroscopy was introduced to this experiment. Fig. 69b presents the SERS spectra of a viral sample (vi5587) acquired with 1 mW laser power. In the spectra, the characteristic bands of biomaterials like amide I and ring breathing modes from Tyrosine (Tyr)/ Phenylalanine (Phe) could be recognized. Lipid signals like PO_2 were not observed, which indirectly indicates that lipids were not in the vicinity of plasmons. According to the structure of SARS-CoV-2 (Fig. 53), spike proteins should primarily connect with Ag nanoparticles. Therefore, the SERS spectrum of the spike (S) protein was further investigated.

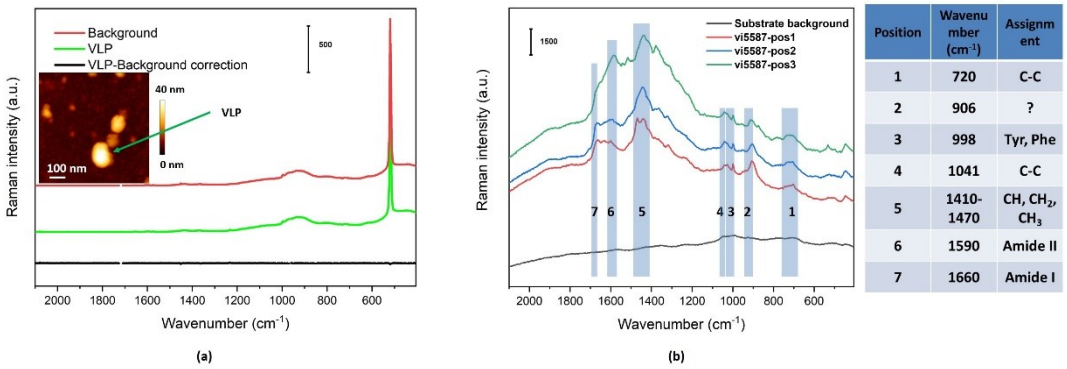

Position	Wavenumber (cm^{-1})	Assignment
1	720	C-C
2	906	?
3	998	Tyr, Phe
4	1041	C-C
5	1410-1470	CH, CH_2, CH_3
6	1590	Amide II
7	1660	Amide I

Fig. 69 (a) AFM-correlated conventional Raman spectra of a virus-like particle (VLP). Conventional Raman spectroscopy is difficult to acquire the structure information from a single VLP;(b) SERS spectra of a virus sample and band assignments on 7 labelled bands.

The S protein has a trimer structure, which is composed of 3 S1 and S2 subunits. According to TEM images, its size is estimated to be around 6-10 nm in width and 20-30 nm in length[165, 166], which cannot be precisely imaged by our Tap190 AFM tips. In Fig. 70, the SERS spectra of S protein and a virus sample were compared. The position of amide I band of S protein indicate that an α helix dominates the structure. Very few Phe or Tyr are exposed outside of the structure. The spectrum of the S protein fits onto the one of the vi5587 sample. However, the spectrum of vi5587 is a convoluted spectrum coming from the signals of surface compositions. It is difficult to deduce the

origins of these signals on the virus-like particle, which could originate from S proteins or other compounds.

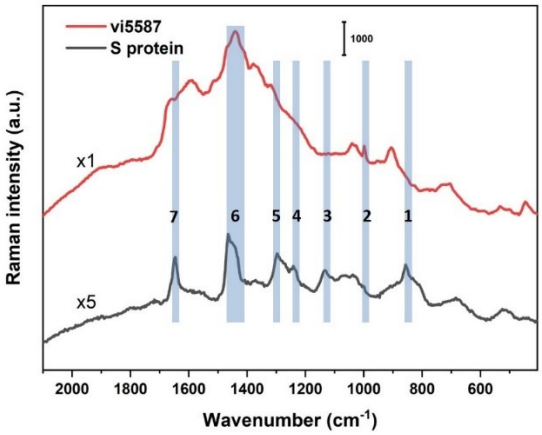

Position	Wavenumber (cm^{-1})	Assignment
1	858	?
2	998	Tyr, Phe
3	1132	C-C stretching
4	1238	Amide III
5	1297	
6	1461	CH_2 bending
7	1648	Amide I

Fig. 70 SERS spectra of S protein and virus sample vi5587. 7 bands of S protein are assigned and compared to the spectrum of vi5587.

In the follwing experiment, it is found that PFA appears to cause a conformational change on peptides/proteins by the crosslinks of PFAs and NH_2 groups of peptides/proteins. Fig. 71 shows the SERS spectra variation of bovine serum albumin (BSA) before and after the treatment with PFA. The amide I band of BSA disappeared after the PFA treatment. Additionally, the relative intensity of the ring breathing mode at around 1000 cm^{-1} showed an evident decrease. This phenomenon suggests that the Raman spectrum of an inactivated virus sample may be different from one without PFA treatment.

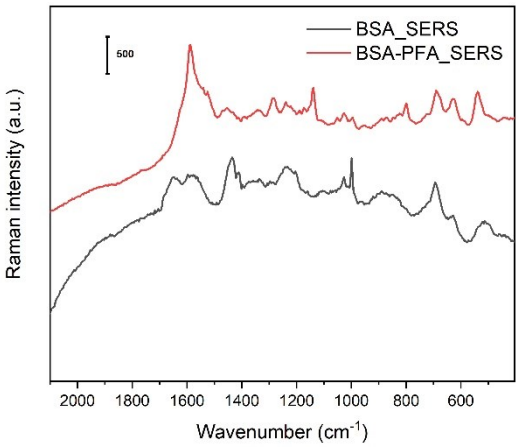

Fig. 71 SERS spectra of BSA and BSA-PFA complex. The spectrum of BSA changed after the treatment of PFA, which indicates that PFA may change the structure of peptides/proteins.

Besides the influence of PFA, it is also difficult to assign the origins of these signals from such a complex viral sample in conventional Raman and SERS spectra. First, there

are cell residues from culturing the virus. Second, there are other membrane proteins, apart from the spike protein, on the envelope of virions. To further study the surface composition of SARS-CoV-2, TERS measurements are preferable.

5.4.2 TERS measurements on SARS-CoV-2

In contrast to SERS spectroscopy, TERS spectroscopy provides an even higher resolution at the nanoscale. Signal acquisitions could be limited to the target virus-like particles. In this way, the influence from contaminants and cell residues could be avoided to a great extent. Based on above-mentioned experiments, TERS measurements were conducted on the most-likely virus-like particles. Fig. 72 shows an example of the TERS measurements. A 10x10 grid at the scale of 150x150 nm^2 was set to acquire signals from a virus-like particle (VLP04303, the red square in Fig. 72a). A control experiment was conducted to acquire signals from a blank position. No real signals were acquired in the control experiment confirming these measurements were successful and reliable.

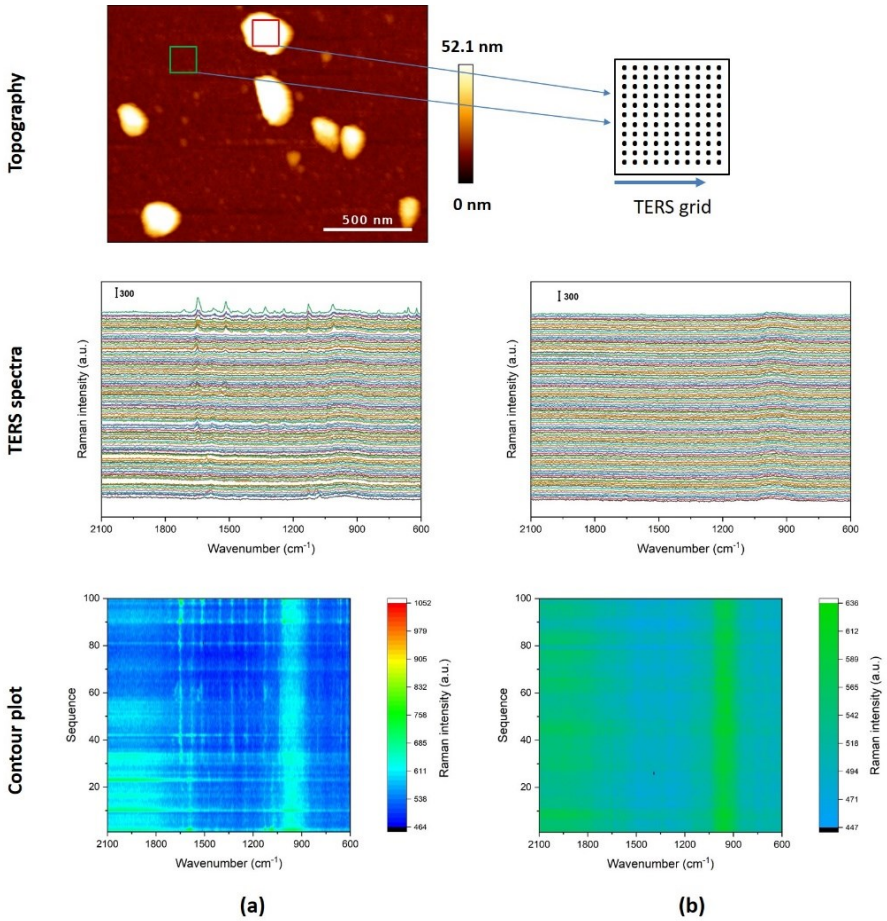

Fig. 72 AFM topography and TERS spectra on (a) and off (b) VLP04303. A 10x10 grid was set to acuquire spectra from VLP04303 and the background. The spectra of VLP04303 show clear difference to the mica background.

Referring to the Raman experiments on CaL and lipids in Chapter 4 and other references[167-170], the TERS spectra of VLP04303 are further assigned (see the table of Fig. 73). The band at 1650 cm^{-1} is normally assigned to the amide I band of peptides/proteins. Furthermore, the two bands at 1516/1573 cm^{-1} and 1241/1286 cm^{-1} are usually assigned to amide II and amide III bands, respectively. Thus, the existence of proteins is confirmed. Bands at 1712cm^{-1} and 1075 cm^{-1} could be assigned to C=O stretching of esters and PO_2 stretching coming from lipids. Combining the AFM image and the TERS spectra, this target is almost certainly a virus-like particle.

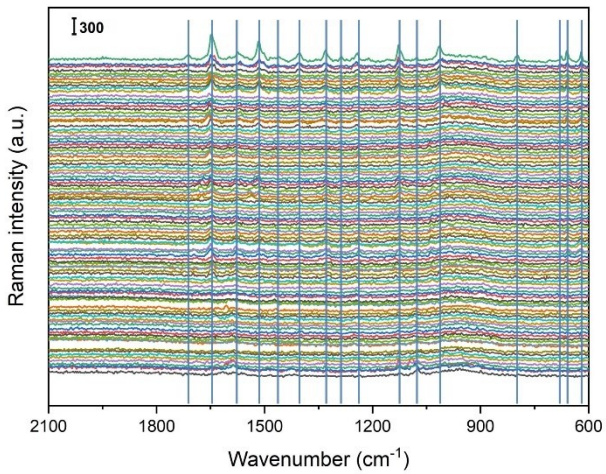

Wavenumber (cm^{-1})	Assignment	Remark
619	?	
659	C-S stretching	Cys?
676		
797	?	
1015	Ring bending (Tyr, Phe)	Protein
1075	PO_2 stretching	Lipid
1128	C-C or C-N stretching	
1241	Amide III	Protein
1286		
1330	CH, CH_2, CH_3 (Wagging, deformation, bending)	
1403		
1460		
1516	Amide II	Protein
1573		
1650	Amide I	Protein
1712	Ester C=O stretching	Lipid

Fig. 73 Assignments of TERS spectra of VLP04303. The PO_2 and C=O stretching confirm the existence of lipid membrane while the amide bands refer to proteins.

In fact, it has been proven that TERS spectroscopy can distinguish different viruses in previous experiments conducted by our group[171]. However, it still presents a challenge to apply it onto such a complex bio-sample. First, the surface of virus-like particls is sticky, which means that during measurements many sticky compositions were dislodged/caught by the tips or the Ag nanoparticles were held/seized by the targets. These signals indirectly reflect the surface compositions of virus-like particles.

Fig. 74 presents a measurement on a virus-like particle VLP04307 using the same tip and parameters as the one in Fig. 73; the measurement indicates “sample-fishing”. From the spectra, a temporarily fishing-dropping process of the same material is observed. The step size was 15 nm between each spectrum. In contrast, the size of the S protein is around 20 nm. Thus, the second fishing after the first drop could not be from the same material. This means that the surface of this virus-like particle is rich in this material. From the repeated spectra, it is assumed that these materials are in a similar orientation. According to the assignment, peptide/protein bands like Fig. 73

were assigned. It is noted that lipid signals were absent in this case. A sole C=O stretching band cannot be convincibly assigned to lipids. Surprisingly, these bands are very similar to those in Fig. 73.

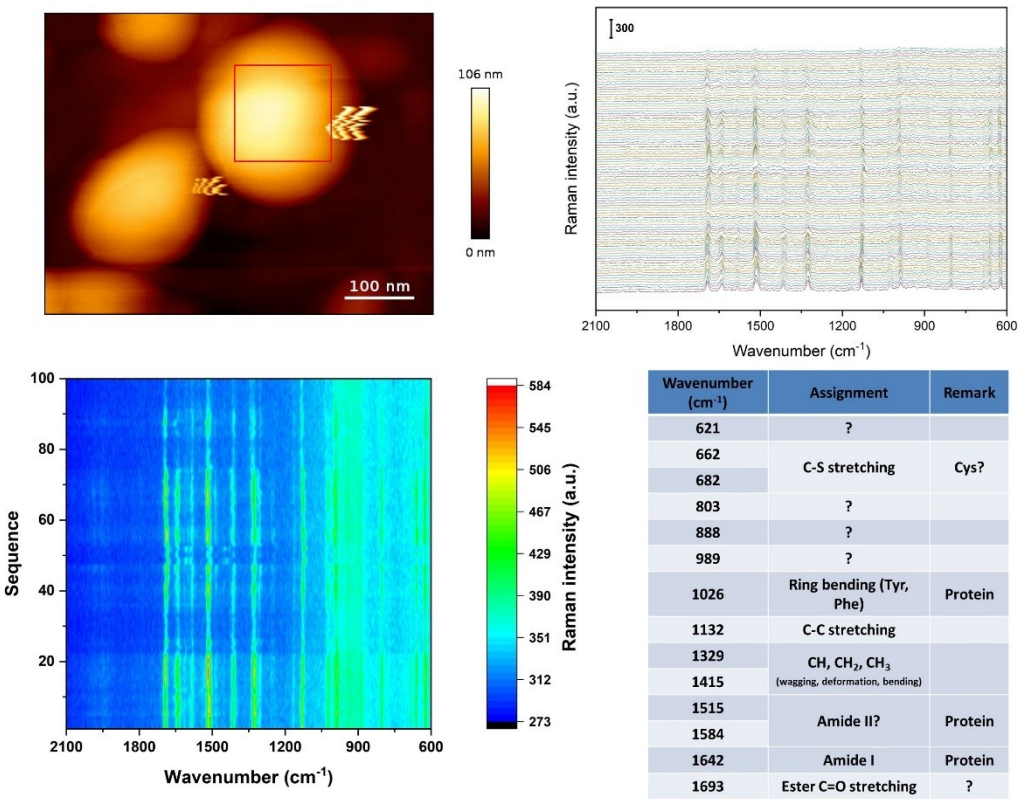

Wavenumber (cm^{-1})	Assignment	Remark
621	?	
662	C-S stretching	Cys?
682		
803	?	
888	?	
989	?	
1026	Ring bending (Tyr, Phe)	Protein
1132	C-C stretching	
1329	CH, CH_2, CH_3 (wagging, deformation, bending)	
1415		
1515	Amide II?	Protein
1584		
1642	Amide I	Protein
1693	Ester C=O stretching	?

Fig. 74 TERS spectra and their assignments of a virus-like particle. The highly repeated TERS spectra indicate this is a fished sample while they still show the signals of proteins.

In a follow-up experiment using the same tip, a peptide/protein was found to stick to the tip permanently, which also shows similar TERS spectra to previous measurements. The average (out of 100) TERS spectra of these 3 virus-like particles are presented in Fig. 75. Amide bands and C-S stretching (may be from cysteine) are assigned. The lipid signal of PO_2 stretching is only present in the spectra from VLP04303 while it is absent in the fishing spectra of VLP04307 and VLP04308. Therefore, it is confirmed that some unknown peptide or protein on the virus-like particles was fished by tips from the surface of virus-like particles. The slight difference between the TERS spectra of VLP04307 (temporary fishing) and VLP04308 (permanent fishing) reflects the variation of molecular orientation on TERS spectra. Additionally, even though material was fished, these spectra indicate the reproducibility of these tips and that measurements were reliable. Still, currently it is difficult to determine whether the origin of these signals comes from the S protein, membrane protein, or culturing contaminants.
Besides, the surface of virus-like particles is extremely complex, being full of sugars, proteins, and lipids. Various proteins were detected in our TERS measurements.

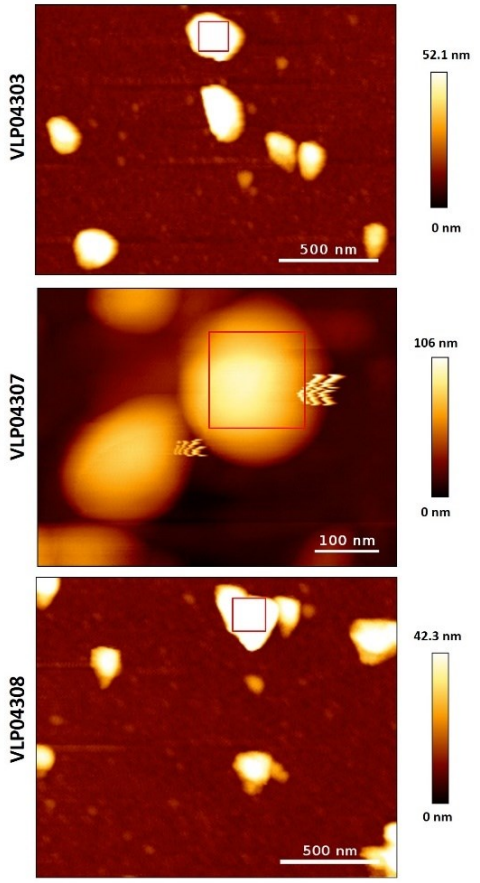

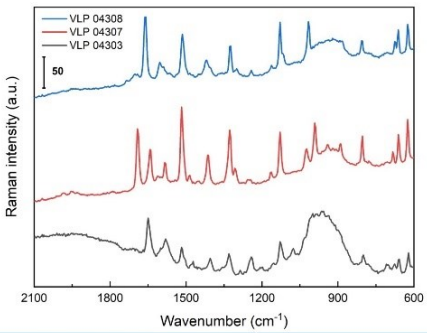

Wavenumber (cm^{-1})			Assignment
VLP04303	VLP04307	VLP04308	
619	621	627	?
659	662	663	C-S stretching
676	682	676	
797	803	809	?
-	888	-	?
-	989	-	?
1015	1026	1017	Ring bending (Tyr, Phe)
1075	-	-	PO_2^- stretching
1128	1132	1132	C-C stretching
1241	-	-	Amide III?
1286	-	-	CH, CH_2, CH_3 (Wagging, deformation, bending)
1330	1329	1326	
1403	1415	1415	
1460	-	-	
1516	1515	1516	Amide II
1573	1584	1587	
-	-	1605	?
1650	1642	1662	Amide I
-	1693	1692	Ester C=O stretching
1712	-	1710	

Fig. 75 Topography images and TERS spectra of 3 different virus-like particles. The similarity of these spectra indicates that these TERS measurements were reliable.

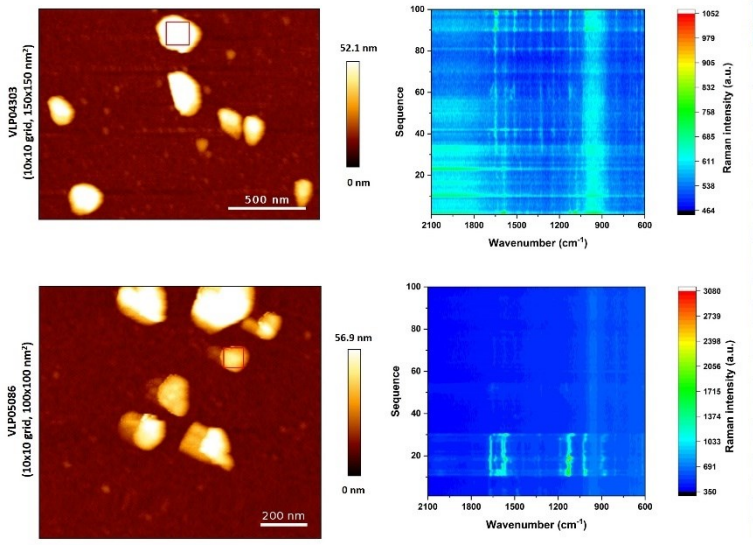

Wavenumber (cm^{-1})		Assignment
VLP04303	VLP05086	
619	623	?
659	-	C-S stretching
676	-	
797	800	?
-	901	?
1015	1023	Ring bending (Tyr, Phe)
1075	-	PO_2^- stretching
1128	1126	C-C or C-N stretching
-	1189	?
1241		Amide III
1286		
1330	1330	CH, CH_2, CH_3 (Wagging, deformation, bending)
1403		
	1441	
1460	-	
	1486	
1516	-	Amide II?
	1530	
	1565	
1573	1585	
-	1613	Amide I
-	1633	
1650	-	
-	1667	
1712	-	Ester C=O stretching

Fig. 76 Comparison of 2 different virus-like particles from 2 different tips. Lipid signals were detected in VLP04303 while they could not be detected in VLP05086. Both spectra indicate the existence of peptides/proteins on the surfaces of these particles.

Fig. 76 shows the comparison of two different measurements. The material detected in VLP05086 is defined as some peptide/protein, which clearly differs from the one detected in VLP04303. The signal absence may be caused by the tip's loss of Ag nanoparticles. In the next stage, more TERS measurements will be conducted to analyze and find the dominant proteins on the surface of virus-like particles. The characteristic Raman spectra of compositions of SARS-CoV-2 are expected to be recognized. For a comparison, a better-known engineered and inactive HIV-1 will be introduced in following experiments[172].

5.5 Chapter summary

SARS-CoV-2 is widely distributed around the world with its powerful transmission capability. The tremendous volume of infected patients exposes the drawback of current detection techniques among which the false negative rate may reach up to 30% (highly affected by the quality of detection products), thus, increasing the uncontrollability of the situation. Thus, the development of supplementary methods is meaningful not only at this very moment but also for the future. This thesis has explored an AFM-TERS correlation method for the detection of SARS-CoV-2.

With its excellent spatial resolution and flexible application conditions, AFM presents itself as a candidate for virus detection, as it can simultaneously realize topographic imaging and mechanic investigations. First, it has been confirmed that it is possible to distinguish virus-like particles from a complex background with an AFM setup. Second, virus-like particles can be distinguished from resembling objects like PFA using mechanic measurements. Finally, the mechanic investigations show that AFM can distinguish virions from vesicles.

To compensate the shortage of AFM in composition analysis, Raman spectroscopy was introduced to investigate the virus' surface composition. Being limited by the low Raman cross-section of biomaterials, conventional Raman is unable to acquire signals from a trace amount sample. TERS spectroscopy, however, can study targets at the nanoscale, which confirmed the existence of proteins upon these virus-like particles and verified the validity of the screening criterion in AFM experiments.

This experiment confirms that the AFM-TERS method is promising in providing substantial information and to improve the accuracy of viral detection. In a next step, more TERS measurements will be conducted on the investigations of S proteins, aiming at realizing a direct recognization of SARS-CoV-2 and to perfect this AFM-TERS method in the investigations of SARS-CoV-2.

6. Summary

The emergence of super-resolution techniques pushes detection capabilities towards the nanoscopic scale. These techniques have been widely applied in fields like food sciences, forensics, and life sciences, and contributes to the improvement of our daily life. AFM, as a non-labeling technique, has its advantages in the research of topographical imaging, and nanomechanics. By combining the method with plasmonics and a Raman spectrometer, AFM-TERS spectroscopy, overcomes the low Raman cross-section of biomaterials and the optical diffraction limit, and realize the simultaneous acquisition of topographic and chemical information at the nanoscale. In this thesis, AFM and AFM-TERS spectroscopy were applied for the investigations of biomaterials — CaL and SARS-CoV-2. According to our knowledge experiments on them have been conducted for the first time.

With respect to plasmon/particle induced band shifts, SERS spectroscopy was introduced as a bridge between conventional Raman and TERS spectroscopy. During the research, some drawbacks were found on glass-supported silver SERS substrates. First, an extra Cr coating on the PVD-manufactured SERS substrates has been confirmed to improve the resistance of substrates to salt solutions. Second, photocatalysis, originating from Ag and Ag_2O, is proposed to be one of reasons of sample degradation in SERS measurements. In Chapter 3, for the first time, iodide has been found to suppress sample degradation. This method also further improves the reliability and reproducibility of SERS measurements. For the time being, it is assumed that free iodide dominates the suppression process.

The fungal family *Candida* is responsible for a large number of deaths worldwide every year. However, the pathogenicity is still not well understood, hindering the progress of clinical therapies and drug developments. To investigate the behavior of CaL, the first recognized fugal peptide from *Candida albicans*, is expected to change the current dilemma caused by *Candida*. In chapter 4, the first experiments investigating the mode of action of CaL using AFM and Raman spectroscopy were presented. In the experiment using AFM, CaL is suggested to choose a complex mode of action to cause pore formation on lipid membranes. The first conventional Raman/SERS spectrum of CaL confirmed that CaL has a stable helical structure before and after the interaction with lipids. Moreover, TERS spectroscopy revealed that CaL may have multiple helical structures. Due to blocking by the protein-rich protective layer on the cell membrane,

TERS tips were unable to access the surface of the lipid membrane and thus localize the distribution of CaL upon cell membranes. A new method to overcome this issue will be following.

In contrast to *Candida*-related issues, a more urgent issue catches our attention: the high false negative rates of current rapid detection techniques of SARS-CoV-2. To overcome this issue, supplementary or alternative methods have to be developed. The combination of AFM and TERS spectroscopy is expected to be a promising method with their high spatial resolution, sensitivity, and specificity. In Chapter 5, combined with the topography and nanomechanics of SARS-CoV-2, it was proposed that AFM can distinguish virions from other materials like PFA and even virus-like vesicles. TERS spectroscopy confirmed the existence of proteins and lipids on the surface of virus-like particles based on the AFM experiments. More investigations are also in progress here. In conclusion, this method is believed to contribute to the detection and research on SARS-CoV-2.

In this thesis, the first stage of the study of these biomaterials using AFM-TERS correlation study has been successfully achieved. However, these are still early days and further experiments are suggested for the next stage. First, a suitable protection material for TERS tips needs to be investigated to allow reproducible TERS measurements in liquid. In this way, a more in-depth analysis of the behavior of CaL under physiological conditions can be performed using TERS spectroscopy. Although AFM-TERS shows its impressive capabilities in the study of SARS-CoV-2, it is still far away from a real clinical application. The nanomechanics of SARS-CoV-2 needs to be further investigated to construct a complete mechanic model. Nevertheless, it is quite realistic that there will soon be an advanced AFM-TERS method that can help with the detection of various viruses and other pathogens.

Zusammenfassung

Das Aufkommen von “super-resolution” Methoden verschiebt die Möglichkeiten der Detektion in den Nanometerbereich. Diese hochauflösenden Verfahren finden breite Anwendung in Bereichen der Lebensmittelwissenschaften und tragen so zur Verbesserung unseres täglichen Lebens bei. Als Marker-freie Methode hat AFM seine Vorzüge bei der Erforschung der topographischen Bildgebung und der Nanomechanik. Durch die Kombination der Methode mit der Plasmonik und einem Raman-Spektrometer, der AFM-TERS-Spektroskopie, wird der geringe Raman-Streuquerschnitt von Biomaterialien und die optische Beugungsgrenze überwunden. Gleichzeitig wird die Erfassung von topographischen und chemischen Informationen auf der Nanoskala realisiert. In der vorliegenden Arbeit wurden AFM- und AFM-TERS-Spektroskopie für die Untersuchung von Biomaterialien - CaL und SARS-CoV-2 - eingesetzt. Nach unserem Kenntnisstand wurden Experimente an diesen Materialien zum ersten Mal durchgeführt.

Im Hinblick auf plasmonen-/partikelinduzierte Bandenverschiebungen wurde die SERS-Spektroskopie als Brückenschlag zwischen konventioneller Raman- und TERS-Spektroskopie eingeführt. Während der Untersuchungen wurden einige Nachteile bei der Anwendung von silberbasierten SERS-Substraten auf Glasoberfläche festgestellt. Zum einen konnte gezeigt werden, dass eine zusätzliche Cr-Beschichtung auf den PVD-gefertigten SERS-Substraten die Beständigkeit der Substrate gegenüber Salzlösungen verbessert. Zum anderen wurde die Photokatalyse, die von Ag und Ag2O ausgeht, als einer der Gründe für die Degradation der Proben bei SERS-Messungen postuliert. In Kapitel 3 wurde zum ersten Mal festgestellt, dass Iodid diese Probendegradation unterdrückt. Darüber hinaus verbessert diese Methode die Genauigkeit und Reproduzierbarkeit von SERS-Messungen. Vorerst wird davon ausgegangen, dass freies Iodid die Hauptrolle beim der Unterdrückungsprozess übernimmt.

Die Pilzfamilie Candida ist jedes Jahr weltweit für eine große Anzahl von Todesfällen verantwortlich. Dennoch ist der Infektionsmechanismus nicht ausreichend verstanden, was den Fortschritt von klinischen Therapien und die Entwicklung von Medikamenten beeinträchtigt. Die Untersuchung des Wirkmechanismus von CaL, dem ersten erkannten fugalen Peptid aus Candida albicans, soll dies verändern. In Kapitel 4 wurden die ersten Experimente zur Untersuchung der Wirkungsweise von CaL mittels AFM und Raman-Spektroskopie vorgestellt. Im Experiment mit AFM wird angenommen, dass CaL einen komplexen Wirkmechanismus nutzt, um eine

Porenbildung auf Lipidmembranen zu induzieren. Das erste konventionelle Raman/SERS-Spektrum von CaL bestätigte, dass CaL vor und nach der Wechselwirkung mit Lipiden eine stabile helikale Struktur aufweist. Darüber hinaus zeigte die TERS-Spektroskopie, dass CaL mehrere helikale Strukturen aufweisen kann. Die TERS-Spitzen konnten die Oberfläche der Zellmembran aufgrund der proteinreichen Schutzschicht der Membran nicht zu erreichen. Somit konnte die Verteilung von CaL auf der Zellmembran nicht lokalisiert werden. Eine neue Methode zur Überwindung dieser Herausforderung wird folgen.

Neben den Herausforderung die Candida darstellt erregt ein weitaus dringlicherer Punkt unsere Aufmerksamkeit: die hohen Falsch-Negativ-Raten der derzeitigen schnellen Nachweisverfahren für SARS-CoV-2. Um diese Herausforderung zu bewältigen, müssen ergänzende oder alternative Methoden entwickelt werden. Die Kombination von AFM- und TERS-Spektroskopie stellt aufgrund ihrer hohen räumlichen Auflösung, Sensitivität und Spezifität eine vielversprechende Methode dar. In Kapitel 5 wurde in Verbindung mit der Topographie und Nanomechanik von SARS-CoV-2 gezeigt, dass mit Hilfe von AFM Virionen von anderen Materialien wie PFA und sogar virusähnlichen Vesikeln unterschieden werden können. Die TERS-Spektroskopie bestätigte auf Basis der AFM-Experimente die Existenz von Proteinen und Lipiden auf der Oberfläche der virusähnlichen Partikel. Auch hier sind weitere Untersuchungen im Gange. Zusammenfassend lässt sich sagen, dass diese Methode einen Beitrag zur Erkennung und Erforschung von SARS-CoV-2 leisten kann.

In dieser Dissertation wurden erste Schritte zur Untersuchung der oben genannten Biomaterialien mittels einer Korrelation von AFM und TERS erfolgreich durchgeführt. Es handelt sich jedoch noch um Anfänge, sodass weitere Experimente vorgeschlagen werden. Als nächstes muss ein geeignetes Material zum Schutz der TERS-Spitzen untersucht werden, um reproduzierbare TERS-Messungen in Flüssigkeit zu ermöglichen. Auf diese Weise kann eine genauere Analyse des Wirkmechanismus von CaL unter physiologischen Bedingungen mittels TERS-Spektroskopie durchgeführt werden. Obwohl AFM-TERS bei der Untersuchung von SARS-CoV-2 seine beeindruckenden Fähigkeiten zeigt, ist die Methode noch weit entfernt von einer klinischen Anwendung. Die Nanomechanik von SARS-CoV-2 muss zunächst weiter untersucht werden, um ein vollständiges mechanisches Modell zu konstruieren. Nichtsdestotrotz ist es durchaus realistisch, dass es bald eine fortschrittliche AFM-TERS-Methode geben wird, die bei der Erkennung verschiedener Viren und anderer Krankheitserreger helfen kann.

References

1. Abbe E., *Beiträge zur Theorie des Mikroskops und der mikroskopischen Wahrnehmung.* Archiv für mikroskopische Anatomie, 1873. **9**: p. 413-468.
2. Synge E.H., *XXXVIII.A suggested method for extending microscopic resolution into the ultra-microscopic region.* The London, Edinburgh, and Dublin Philosophical Magazine and Journal of Science, 1928. **6**(35): p. 356-362.
3. Pohl D.W., Denk W., and Lanz M., *Optical stethoscopy: Image recording with resolution λ/20.* Applied Physics Letters, 1984. **44**(7): p. 651-653.
4. Novotny L., *The History of Near-field Optics*, *Progress in Optics*. 2007. **50**: p. 137-183.
5. Johnson T., et al., *Highly Reproducible Near-Field Optical imaging with sub20 nm resolution based on template stripped gold pyramids.* ACS Nano, 2012. **6**: p. 9168-9174.
6. Wang Z., et al., *Optical virtual imaging at 50 nm lateral resolution with a white-light nanoscope.* Nat Commun, 2011. **2**: p. 218.
7. Hosaka N. and Saiki T., *10 nm Spatial Resolution Fluorescence Imaging of Single Molecules by Near-Field Scanning Optical Microscopy Using a Tiny Aperture Probe.* Optical Review, 2006. **13**: p. 262-265.
8. De Wilde Y., et al., *Review of NSOM Microscopy for Materials*, *AIP Conference Proceedings*. 2007. **931**: p. 43-52.
9. Fujihira M., et al., *Scanning near-field optical microscopy of fluorescent polystyrene spheres with a combined SNOM and AFM.* Ultramicroscopy, 1995. **61**: p. 271-277.
10. Nakajima K., et al., *Development of a Hybrid Scanning Near-field Optical-Tunneling Microscope (SNOM-STM) System.* Jpn. J. Appl. Phys., 1999. **38**: p. 3949-3953.
11. Olmon R.L., et al., *Near-field imaging of optical antenna modes in the mid-infrared.* Optical Express, 2008. **16**: p. 20295-20305.
12. Novotny L. and van Hulst N., *Antennas for light.* Nature Photonics, 2011. **5**: p. 83-90.
13. Lin H.-Y., et al., *Direct near-field optical imaging of plasmonic resonances in metal nanoparticle pairs.* Optical Express, 2010. **18**: p. 165-172.
14. Stöckle R.M., et al., *Nanoscale chemical analysis by tip-enhanced Raman spectroscopy.* Chemical Physics Letters, 2000. **318**: p. 131-136.
15. Höppener C. and Novotny L., *Antenna-based optical imaging of single ca2+ transmembrane proteins in liquids.* Nano Letters, 2008. **8**: p. 642-646.
16. Meyer R., Yao X., and Deckert V., *Latest instrumental development and bioanalytical applications in TERS.* Trends in Analytical Chemistry, 2018. **102**: p. 250-258.
17. Lakowicz J.R., *Principles Of Fluorescence Spectroscopy*. 2006: Springer, Boston, MA.
18. St Croix C.M., Shand S.H., and Watkins S.C., *Confocal microscopy: comparisons, applications, and problems.* Biotechniques, 2005. **39**(6 Suppl): p. S2-5.
19. Huang B., Bates M., and Zhuang X., *Super-resolution fluorescence microscopy.* Annu Rev Biochem, 2009. **78**: p. 993-1016.
20. Vicidomini G., Bianchini P., and Diaspro A., *STED super-resolved microscopy.* Nat Methods, 2018. **15**(3): p. 173-182.
21. Gottfert F., et al., *Coaligned dual-channel STED nanoscopy and molecular diffusion analysis at 20 nm resolution.* Biophys J, 2013. **105**(1): p. L01-03.

22. Takayanagi K., et al., *Electron microscopy at a sub-50 pm resolution.* J Electron Microsc (Tokyo), 2011. **60** (Suppl 1): p. S239-244.
23. Liu C., et al., *The Architecture of Inactivated SARS-CoV-2 with Postfusion Spikes Revealed by Cryo-EM and Cryo-ET.* Structure, 2020. **28**: p. 1218-1224.
24. Wrapp D., et al., *Cryo-EM structure of the 2019-nCoV spike in the prefusion conformation.* Science, 2020. **367**: p. 1260-1263.
25. Binnig G. and Rohrer H., *Scanning tunnelling microscopy.* Surface Science, 1983. **126**: p. 236-244.
26. Binnig G., Quate C.F., and Gerber C., *Atomic force microscope.* Phys Rev Lett, 1986. **56**(9): p. 930-933.
27. Raman C.V. and K.S. Krishnan, *A new type of secondary radiation.* Nature, 1928. **121**: p. 501-502.
28. Aroca R., *Surface enhanced vibrational spectroscopy*. 2006: Wiley. 251.
29. Fleischmann M., Hendra P.J., and McQuillan A.J., *Raman spectra of pyridine adsorbed at a silver electrode.* Chemical Physics Letters, 1974. **26**: p. 163-166.
30. Jeanmaire D. L. and Van Duyne R.P., *Surface raman spectroelectrochemistry Part I. Heterocyclic, aromatic, and aliphatic amines adsorbed on the anodized silver electrode.* J. Electroanal. Chem., 1977. **84**: p. 1-20.
31. Takayama O., A.A. Bogdanov, and A.V. Lavrinenko, *Photonic surface waves on metamaterial interfaces.* J Phys Condens Matter, 2017. **29**(46): p. 463001.
32. Tang Y., Zeng X., and Liang J., *Surface Plasmon Resonance: An Introduction to a Surface Spectroscopy Technique.* J. Chem. Educ., 2010. **87**: p. 742-746.
33. Sui M., et al., *Strongly confined localized surface plasmon resonance (LSPR) bands of Pt, AgPt, AgAuPt nanoparticles.* Sci Rep, 2019. **9**(1): p. 16582.
34. Sepúlveda B., et al., *LSPR-based nanobiosensors.* Nano Today, 2009. **4**(3): p. 244-251.
35. Bansal A., Sekhon J.S., and Verma S.S., *Scattering Efficiency and LSPR Tunability of Bimetallic Ag, Au, and Cu Nanoparticles.* Plasmonics, 2013. **9**(1): p. 143-150.
36. Le Ru E.C., et al., *Surface Enhanced Raman Scattering Enhancement Factors: A Comprehensive Study.* J. Phys. Chem. C, 2007. **111**: p. 13794-13803.
37. Ding S.-Y., et al., *Nanostructure-based plasmon enhanced Raman spectroscopy for surface analysis of materials.* Nature Reviews Materials, 2016. **1**: p. 1-16.
38. Langer J., et al., *Present and Future of Surface-Enhanced Raman Scattering.* ACS Nano, 2020. **14**(1): p. 28-117.
39. Amendola V., et al., *Surface plasmon resonance in gold nanoparticles: a review.* J Phys Condens Matter, 2017. **29**(20): p. 203002.
40. Mogensen K.B. and Kneipp K., *Size-Dependent Shifts of Plasmon Resonance in Silver Nanoparticle Films Using Controlled Dissolution: Monitoring the Onset of Surface Screening Effects.* The Journal of Physical Chemistry C, 2014. **118**(48): p. 28075-28083.
41. Schira R. and Rabilloud F., *Localized Surface Plasmon Resonance in Free Silver Nanoclusters Agn,n= 20–147.* The Journal of Physical Chemistry C, 2019. **123**(10): p. 6205-6212.
42. Brown R.J.C. and Milton M.J.T., *Nanostructures and nanostructured substrates for surface-enhanced Raman scattering (SERS).* Journal of Raman Spectroscopy, 2008. **39**(10): p. 1313-1326.
43. Novikov S.M., et al., *Highly Stable Monocrystalline Silver Clusters for Plasmonic Applications.*

Langmuir, 2017. **33**(24): p. 6062-6070.
44. Herzog J.B., Knight M.W., and Natelson D., *Thermoplasmonics: quantifying plasmonic heating in single nanowires.* Nano Lett, 2014. **14**(2): p. 499-503.
45. Zeng Z.C., et al., *Photothermal Microscopy of Coupled Nanostructures and the Impact of Nanoscale Heating in Surface Enhanced Raman Spectroscopy.* J Phys Chem C Nanomater Interfaces, 2017. **121**(21): p. 11623-11631.
46. Pilot R., et al., *A Review on Surface-Enhanced Raman Scattering.* Biosensors (Basel), 2019. **9**(2): p. 57.
47. Wang F., et al., *Selectivity/Specificity Improvement Strategies in Surface-Enhanced Raman Spectroscopy Analysis.* Sensors (Basel), 2017. **17**(11): p. 2689.
48. Blum C., et al., *Understanding tip-enhanced Raman spectra of biological molecules: a combined Raman, SERS and TERS study.* Journal of Raman Spectroscopy, 2012. **43**(12): p. 1895-1904.
49. Anderson M.S., *Locally enhanced Raman spectroscopy with an atomic force microscope.* Applied Physics Letters, 2000. **76**(21): p. 3130-3132.
50. Hayazawa N., et al., *Metallized tip amplification of near-field Raman scattering.* Optics Communications, 2000. **183**: p. 333-336.
51. Latorre F., et al., *Spatial resolution of tip-enhanced Raman spectroscopy – DFT assessment of the chemical effect.* Nanoscale, 2016. **8**: p. 10229-10239.
52. Trautmann S., et al., *A classical description of subnanometer resolution by atomic features in metallic structures.* Nanoscale, 2017. **9**: p. 391-401.
53. Trautmann S., et al., *Plasmon response evaluation based on image derived arbitrary nanostructures.* Nanoscale, 2018. **10**: p. 9830-9839.
54. Deckert-Gaudig T., et al., *Tip-enhanced Raman spectroscopy – from early developments to recent advances.* Chem. Soc. Rev., 2017. **46**: p. 4077-4110.
55. Zhang R., et al., *Chemical mapping of a single molecule by plasmon-enhanced Raman scattering.* Nature, 2013. **498**: p. 82-86.
56. Bailo E. and Deckert V., *Tip-Enhanced Raman Spectroscopy of Single RNA Strands Towards a Novel Direct-Sequencing Method.* Angew. Chem. Int. Ed., 2008. **47**: p. 1658-1661.
57. He Z., et al., *Tip-Enhanced Raman Imaging of Single-Stranded DNA with Single Base Resolution.* J Am Chem Soc, 2019. **141**(2): p. 753-757.
58. Li J.F., et al., *Shell-isolated nanoparticle-enhanced Raman spectroscopy.* Nature, 2010. **464**(7287): p. 392-5.
59. Huang Y.-P., *Shell-Isolated Tip-Enhanced Raman and Fluorescence Spectroscopy.* Angew. Chem. Int. Ed., 2018. **57**: p. 6.
60. Kazemi-Zanjani N., Vedraine S., and Lagugne-Labarthet F., *Localized enhancement of electric field in tip-enhanced Raman spectroscopy using radially and linearly polarized light.* Opt Express, 2013. **21**(21): p. 25271-25276.
61. Langelüddecke L., Singh P., and Deckert V., *Exploring the Nanoscale-Fifteen Years of Tip-Enhanced Raman Spectroscopy* Applied Spectroscopy, 2015. **69**: p. 1357-1371.
62. Gao L., et al., *Atomic Force Microscopy Based Tip-Enhanced Raman Spectroscopy in Biology.* Int J Mol Sci, 2018. **19**(4).
63. Lipiec E., et al., *Preparation of Well Defined DNA Samples for Reproducible Nanospectroscopic Measurements.* Small, 2016. **12**: p. 4821-4829.
64. Kurouski D., et al., *Amide I vibrational mode suppression in surface (SERS) and tip (TERS)*

enhanced Raman spectra of protein specimens. Analyst, 2013. **138**: p. 1665-1674.

65. Blum C., et al., *Missing Amide I Mode in Gap-Mode Tip-Enhanced Raman Spectra of Proteins.* J Phys Chem C, 2012. **116**: p. 23061-23066.
66. Kumar N., et al. *Nanoscale chemical imaging of solid–liquid interface using TERS.* Nanoscale, 2018. **10**: p. 1815-1824.
67. Richard-Lacoix M., et al., *Mastering high resolution tip-enhanced Raman spectroscopy: towards a shift of perception.* Chem. Soc. Rev., 2017. **46**: p. 3922-3944.
68. Panneerselvam R., et al., *Surface-enhanced Raman spectroscopy: bottlenecks and future directions.* Chem Commun (Camb), 2017. **54**(1): p. 10-25.
69. Witkowska E., et al., *Sources of variability in SERS spectra of bacteria: comprehensive analysis of interactions between selected bacteria and plasmonic nanostructures.* Anal Bioanal Chem, 2019. **411**(10): p. 2001-2017.
70. Alvarez-Puebla R.A., dos Santos D.S.Jr., and Aroca R.F., *SERS detection of environmental pollutants in humic acid-gold nanoparticle composite materials.* Analyst, 2007. **132**(12): p. 1210-1214.
71. Wei H., Abtahi S.M.H., and Vikesland P.J., *Plasmonic colorimetric and SERS sensors for environmental analysis.* Environmental Science: Nano, 2015. **2**(2): p. 120-135.
72. Li Y., et al., *A simple enzyme-free SERS sensor for the rapid and sensitive detection of hydrogen peroxide in food.* Analyst, 2020. **145**(2): p. 607-612.
73. Muehlethaler C., Leona M., and Lombardi J.R., *Review of Surface Enhanced Raman Scattering Applications in Forensic Science.* Anal Chem, 2016. **88**(1): p. 152-69.
74. Ju J., et al., *Sustained and Cost Effective Silver Substrate for Surface Enhanced Raman Spectroscopy Based Biosensing.* Sci Rep, 2017. **7**(1): p. 6917.
75. Zong C., et al., *Surface-Enhanced Raman Spectroscopy for Bioanalysis- Reliability and Challenges.* Chemical Reviews, 2018. **118**: p. 4946-4980.
76. Cyrankiewicz M., Wybranowski T., and Kruszewski S., *Study of SERS efficiency of metallic colloidal systems.* Journal of Physics: Conference Series, 2007. **79**: p.012013.
77. Siiman O., et al., *Surface-enhanced Raman scattering by citrate on colloidal silver.* The Journal of Physical Chemistry, 1983. **87**(6): p. 1014-1023.
78. Zheng Y., et al., *Surface-Enhanced Raman Scattering (SERS) Substrate Based on Large-Area Well-Defined Gold Nanoparticle Arrays with High SERS Uniformity and Stability.* ChemPlusChem, 2014. **79**(11): p. 1622-1630.
79. Yuan J., et al., *Ordered gold nanoparticle arrays on glass and their characterization.* J Colloid Interface Sci, 2013. **410**: p. 1-10.
80. Nečas D. and Klapetek P., *Gwyddion: an open-source software for SPM data analysis.* Open Physics, 2012. **10**(1): p. 181-188.
81. Repoux M., *Comparison of Background Removal Methods for XPS.* Surface and interface analysis, 1992. **18**: p. 567-570.
82. Stoll S. and Schweiger A., *EasySpin, a comprehensive software package for spectral simulation and analysis in EPR.* J Magn Reson, 2006. **178**(1): p. 42-55.
83. Guilbaud-Massereau V., Celerier A., and Machet J., *Study and improvement of the adhesion of chromium thin films deposited by magnetron sputtering.* Thin Solid Films, 1995. **258**: p. 185-193.
84. Hoogvliet J.C. and van Bennekom W.P., *Gold thin-film electrodes an EQCM study of the influence*

of chromium and titanium adhesion layers on the response. Electrochimica Acta, 2001. **47**: p. 599-611.

85. Gellé A. and Moores A., *Plasmonic nanoparticles: Photocatalysts with a bright future.* Current Opinion in Green and Sustainable Chemistry, 2019. **15**: p. 60-66.
86. Gellé A., et al., *Applications of Plasmon-Enhanced Nanocatalysis to Organic Transformations.* Chem Rev, 2020. **120**(2): p. 986-1041.
87. Fascian C., et al., *High-Temperature Organic Reactions at Room Temperature Using Plasmon Excitation- Decomposition of Dicumyl Peroxide.* Organic Letters, 2011. **13**: p. 204-207.
88. Poklar N. and Vesnaver G., *Thermal Denaturation of Proteins Studied by UV spectroscopy.* J. Chem. Educ., 2000. **77**: p. 380-382.
89. Sharkey D.J., et al., *Antibodies as Thermolabile Switches High Temperature Triggering for the Polymerase Chain Reaction.* Nature Biotechnology, 1994. **12**: p. 506-509.
90. Cheng L., et al., *Functional nanomaterials for phototherapies of cancer.* Chem Rev, 2014. **114**(21): p. 10869-939.
91. Linic S., et al., *Photochemical transformations on plasmonic metal nanoparticles.* Nat Mater, 2015. **14**(6): p. 567-76.
92. Long R., et al., *Coupling Solar Energy into Reactions: Materials Design for Surface Plasmon-Mediated Catalysis.* Small, 2015. **11**(32): p. 3873-89.
93. Xu H., et al., *The formation of visible light-driven Ag/Ag2O photocatalyst with excellent property of photocatalytic activity and photocorrosion inhibition.* J Colloid Interface Sci, 2018. **516**: p. 511-521.
94. Xu Y. and Schoonen M.A.A., *The absolute energy positions of conduction and valence bands of selected semiconducting minerals.* American mineralogist, 2000. **85**: p. 543-556.
95. Wang X., et al., *Ag2O as a new visible-light photocatalyst: self-stability and high photocatalytic activity.* Chemistry, 2011. **17**(28): p. 7777-7780.
96. Nosaka Y. and Nosaka A.Y., *Generation and Detection of Reactive Oxygen Species in Photocatalysis.* Chem Rev, 2017. **117**(17): p. 11302-11336.
97. Weil J.A., *A review of electron spin spectroscopy and its application to the study of paramagnetic defects in crystalline quartz.* Physics and Chemistry of Minerals volume, 1984. **10**: p. 149-165.
98. Zhao H., et al., *Synthesis and biochemical applications of a solid cyclic nitrone spin trap a relatively superior trap for detecting superoxide anions and glutathiyl radicals.* Free Radical Biology & Medicine, 2001. **31**: p. 599-606.
99. Schneider J.T., et al., *Use of scavenger agents in heterogeneous photocatalysis: truths, half-truths, and misinterpretations.* Phys Chem Chem Phys, 2020. **22**(27): p. 15723-15733.
100. Zhang L., et al., *Magnetically separable AgI–BiOI/CoFe2O4 hybrid composites for Hg0 removal: characterization, activity and mechanism.* RSC Advances, 2017. **7**(50): p. 31448-31456.
101. Küpper F.C., et al., *Iodide accumulation provides kelp with an inorganic antioxidant impacting atmospheric chemistry.* PNAS, 2008. **105**: p. 6954-6958.
102. Akel S., et al., *Ag/Ag2O as a Co-Catalyst in TiO2 Photocatalysis: Effect of the Co-Catalyst/Photocatalyst Mass Ratio.* Catalysts, 2018. **8**(12): p. 647.
103. Armstrong D.A., et al., *Standard electrode potentials involving radicals in aqueous solution: inorganic radicals.* BioInorganic Reaction Mechanisms, 2015. **87**(11-12): p. 1139-1150.
104. Tabata M., et al., *Modified Ta3N5 powder as a photocatalyst for O2 evolution in a two-step*

water splitting system with an iodate/iodide shuttle redox mediator under visible light. Langmuir, 2010. **26**(12): p. 9161-5.

105. Wei J., et al., *Controlled in situ fabrication of Ag2O/AgO thin films by a dry chemical route at room temperature for hybrid solar cells.* Dalton Trans, 2014. **43**(29): p. 11333-11338.
106. Xu L.J., et al., *Label-free detection of native proteins by surface-enhanced Raman spectroscopy using iodide-modified nanoparticles.* Anal Chem, 2014. **86**: p. 2238-2245.
107. Brown G.D., Denning D.W., and Levitz S.M., *Tackling human fungal infections.* Science, 2012. **336**(6082): p. 647.
108. Noble S.M., Gianetti B.A., and Witchley J.N., *Candida albicans cell-type switching and functional plasticity in the mammalian host.* Nat Rev Microbiol, 2017. **15**(2): p. 96-108.
109. Brown G.D., et al., *Hidden Killers- Human Fungal Infections.* Science Translational Medicine 2012. **4**: p. 1-9.
110. Moyes D., et al., *Candidalysin is a fungal peptide toxin critical for mucosal infection.* Nautre, 2016. **532**: p. 64-68.
111. Naglik J.R., et al., *Candida albicans-epithelial interactions and induction of mucosal innate immunity.* Current opinion in Microbiology, 2018. **40**: p. 104-112.
112. Naglik J.R., Gaffen S.L., and Hube B., *Candidalysin: discovery and function in Candida albicans infections.* Curr Opin Microbiol, 2019. **52**: p. 100-109.
113. Kasper L., et al., *The fungal peptide toxin Candidalysin activates the NLRP3 inflammasome and causes cytolysis in mononuclear phagocytes.* Nat Commun, 2018. **9**(1): p. 4260.
114. Vance J.E., *Phospholipid synthesis and transport in mammalian cells.* Traffic, 2015. **16**(1): p. 1-18.
115. Sato H. and Feix J.B., *Peptide-membrane interactions and mechanisms of membrane destruction by amphipathic alpha-helical antimicrobial peptides.* Biochim Biophys Acta, 2006. **1758**(9): p. 1245-56.
116. Jean-François F., et al., *Pore formation induced by an antimicrobial peptide: electrostatic effects.* Biophysical Journal, 2008. **95**(12):p.5748-5756.
117. Terwilligert T.C. and Eisenberg D., *The structure of melittin.II. Interpretation of the structure.* The Journal of Biological Chemistry, 1982. **257**: p. 6016-6022.
118. Bodescu M.A., Rosenkoetter F. and Fritz J, *Time lapse AFM on vesicle formation from mixed lipid bilayers induced by the membrane–active peptide melittin.* Soft Matter, 2017. **13**: p.6845-6851.
119. Kumar P., Kizhakkedathu J.N., and Straus S.K., *Antimicrobial Peptides: Diversity, Mechanism of Action and Strategies to Improve the Activity and Biocompatibility In Vivo.* Biomolecules, 2018. **8**(1): p. 1-24.
120. Choi H., Rangarajan N., and Weisshaar J.C., *Lights, Camera, Action! Antimicrobial Peptide Mechanisms Imaged in Space and Time.* Trends Microbiol, 2016. **24**(2): p. 111-122.
121. Asikainen P., et al., *Microplicae--Specialized Surface Structure of Epithelial Cells of Wet-Surfaced Oral Mucosa.* Ultrastruct Pathol, 2015. **39**(5): p. 299-305.
122. Sokolov I., Dokukin M.E., and Guz N.V., *Method for quantitative measurements of the elastic modulus of biological cells in AFM indentation experiments.* Methods, 2013. **60**(2): p. 202-13.
123. Sokolov I., et al., *Detection of surface brush on biological cells in vitro with atomic force microscopy.* Applied Physics Letters, 2007. **91**(2): p. 023902.
124. Andrews P.M., *Microplicae: characteristic ridge-like folds of the plasmalemma.* J Cell Biol., 1976.

68: p. 420-429.

125. Gipson I.K., et al., *Comparison of the transmembrane mucins MUC1 and MUC16 in epithelial barrier function.* PLoS One, 2014. **9**(6): p. e100393.
126. Palla-Papavlu A., et al., *Liposome micropatterning based on laser-induced forward transfer.* Applied Physics A, 2010. **102**(3): p. 651-659.
127. Cernescu A., et al., *Label-Free Infrared Spectroscopy and Imaging of Single Phospholipid Bilayers with Nanoscale Resolution.* Anal Chem, 2018. **90**(17): p. 10179-10186.
128. van Manen H.-J., Lenferink A., and Otto C., *Noninvasive imaging of protein metabolic labeling in single human cells using stable isotopes and raman microscopy.* Anal Chem, 2008. **80**: p. 9576-9582.
129. Beattie J.R., et al., *Raman spectral variation for human fingernails of postmenopausal women is dependent on fracture risk and osteoporosis status.* Journal of Raman Spectroscopy, 2017. **48**(6): p. 813-821.
130. Perez-Guaita D., et al., *Multimodal vibrational imaging of cells.* Vibrational Spectroscopy, 2017. **91**: p. 46-58.
131. Litvinov R.I., et al., *The alpha-helix to beta-sheet transition in stretched and compressed hydrated fibrin clots.* Biophys J, 2012. **103**(5): p. 1020-7.
132. Jacob C.R., Luber S., and Reiher M., *Analysis of Secondary Structure Effects on the IR and Raman Spectra of Polypeptides in terms of localized vibrations.* J. Phys. Chem. B, 2009. **113**: p. 6558-6573.
133. Vieira-Pires R.S. and Morais-Cabral J.H., *3(10) helices in channels and other membrane proteins.* J Gen Physiol, 2010. **136**(6): p. 585-92.
134. Topol I.A., et al., *Alpha and 3_{10}-Helix Interconversion: A quantum-chemical study on polyalanine systems in the gas phase and in aqueous solvent.* J. Am. Chem. Soc., 2001. **123**: p. 6054-6060.
135. Li Q., et al., *Early Transmission Dynamics in Wuhan, China, of Novel Coronavirus-Infected Pneumonia.* N Engl J Med, 2020. **382**(13): p. 1199-1207.
136. V'Kovski P., et al., *Coronavirus biology and replication: implications for SARS-CoV-2.* Nat Rev Microbiol, 2020.**19**: p. 155-170.
137. Fehr A.R. and Perlman S., *Coronaviruses: An Overview of Their Replication and Pathogenesis*, in *Coronaviruses*. 2015, Springer. p. 1-23.
138. Kim D., et al., *The Architecture of SARS-CoV-2 Transcriptome.* Cell, 2020. **181**(4): p. 914-921 e10.
139. Cui J., Li F., and Shi Z.L., *Origin and evolution of pathogenic coronaviruses.* Nat Rev Microbiol, 2019. **17**(3): p. 181-192.
140. Chowell G., et al., *Model Parameters and Outbreak Control for SARS.* Emerging Infectious Diseases, 2004. **10**: p. 1258-1263.
141. Liu Y., et al., *The reproductive number of COVID-19 is higher compared to SARS coronavirus.* J Travel Med, 2020. **27**(2): p. 1-4.
142. Xiong X., et al., *A thermostable, closed SARS-CoV-2 spike protein trimer.* Nat Struct Mol Biol, 2020. **27**(10): p. 934-941.
143. McCallum M., et al., *Structure-guided covalent stabilization of coronavirus spike glycoprotein trimers in the closed conformation.* Nat Struct Mol Biol, 2020. **27**(10): p. 942-949.
144. Huo J., et al., *Neutralizing nanobodies bind SARS-CoV-2 spike RBD and block interaction with ACE2.* Nat Struct Mol Biol, 2020. **27**(9): p. 846-854.
145. Cai Y., et al., *Distinct conformational states of SARS-CoV-2 spike protein.* Science, 2020. **369**: p.

1586-1592.

146. Benton D.J., et al., *Receptor binding and priming of the spike protein of SARS-CoV-2 for membrane fusion.* Nature, 2020. **588**(7837): p. 327-330.

147. Li F., et al., *Structure of SARS Coronavirus Spike Receptor-Binding Domain Complexed with Receptor.* Science, 2005. **309**: p. 1864-1867.

148. Song W., et al., *Cryo-EM structure of the SARS coronavirus spike glycoprotein in complex with its host cell receptor ACE2.* PLoS Pathog, 2018. **14**(8): p. e1007236.

149. Shang J., et al., *Structural basis of receptor recognition by SARS-CoV-2.* Nature, 2020. **581**(7807): p. 221-224.

150. Oran D.P. and Topol E.J., *Prevalence of Asymptomatic SARS-CoV-2 Infection.* Annals of Internal Medicine, 2020. **173**(5): p. 362-367.

151. Long Q.X., et al., *Clinical and immunological assessment of asymptomatic SARS-CoV-2 infections.* Nat Med, 2020. **26**(8): p. 1200-1204.

152. Woloshin S., Patel N., and Kesselheim A.S., *False Negative Tests for SARS-CoV-2 Infection — Challenges and Implications.* N Engl J Med, 2020. **383**: p. 1-3.

153. Ding C., et al., *Development of colloidal gold-based immunochromatographic strip test using two monoclonal antibodies for detection of Vibrio parahaemolyticus.* Journal of Food Safety, 2018. **38**(4): p. 1-7.

154. Shyu R.-H., et al., *Colloidal gold-based immunochromatographic assay for detection of ricin.* Toxicon, 2002. **40**: p. 255-258.

155. Yu X., et al., *Development of Colloidal Gold-Based Immunochromatographic Assay for Rapid Detection of Goose Parvovirus.* Front Microbiol, 2018. **9**: p. 953.

156. Shen B., et al., *Clinical evaluation of a rapid colloidal gold immunochromatography assay for SARS-Cov-2 IgM-IgG.* Am J Transl Res, 2020. **10**: p. 1348-1354.

157. Bustin S.A. and Nolan T., *RT-qPCR Testing of SARS-CoV-2: A Primer.* Int J Mol Sci, 2020. **21**(8): p. 3004.

158. Alcoba-Florez J., et al., *Sensitivity of different RT-qPCR solutions for SARS-CoV-2 detection.* Int J Infect Dis, 2020. **99**: p. 190-192.

159. Bisoffi Z., et al., *Sensitivity, Specificity and Predictive Values of Molecular and Serological Tests for COVID-19: A Longitudinal Study in Emergency Room.* Diagnostics (Basel), 2020. **10**(9): p. 669.

160. Krieg M., et al., *Atomic force microscopy-based mechanobiology.* Nature Reviews Physics, 2018. **1**(1): p. 41-57.

161. Marchetti M., Wuite G., and Roos W.H., *Atomic force microscopy observation and characterization of single virions and virus-like particles by nano-indentation.* Curr Opin Virol, 2016. **18**: p. 82-8.

162. O'Callaghan R., et al., *Stiffness and heterogeneity of the pulmonary endothelial glycocalyx measured by atomic force microscopy.* Am J Physiol Lung Cell Mol Physiol, 2011. **301**(3): p. L353-60.

163. Morris C.E. and Homann U., *Cell surface area regulation and membrane tension.* J Membr Biol, 2001. **179**(2): p. 79-102.

164. Janmey P.A. and Weitz D.A., *Dealing with mechanics: mechanisms of force transduction in cells.* Trends Biochem Sci, 2004. **29**(7): p. 364-70.

165. Ke Z., et al., *Structures and distributions of SARS-CoV-2 spike proteins on intact virions.* Nature, 2020. **588**(7838): p. 498-502.

166. Yao H., et al., *Molecular Architecture of the SARS-CoV-2 Virus.* Cell, 2020. **183**(3): p. 730-738 e13.
167. Rygula A., et al., *Raman spectroscopy of proteins: a review.* Journal of Raman Spectroscopy, 2013. **44**(8): p. 1061-1076.
168. Wood B.R., et al., *Tip-enhanced Raman scattering (TERS) from hemozoin crystals within a sectioned erythrocyte.* Nano Lett, 2011. **11**(5): p. 1868-73.
169. Kurouski D., et al., *Structure and composition of insulin fibril surfaces probed by TERS.* J Am Chem Soc, 2012. **134**(32): p. 13323-9.
170. Deckert-Gaudig T., et al., *Nanoscale distinction of membrane patches--a TERS study of Halobacterium salinarum.* J Biophotonics, 2012. **5**(7): p. 582-91.
171. Deckert V., et al., *Laser spectroscopic technique for direct identification of a single virus I: FASTER CARS.* Proc Natl Acad Sci USA, 2020. **117**(45): p. 27820-27824.
172. Carravilla P., et al., *Molecular recognition of the native HIV-1 MPER revealed by STED microscopy of single virions.* Nat Commun, 2019. **10**(1): p. 78.

Acknowledgements

Looking back on these years, I can easily recount every moment that is so vivid in my mind. From the time I opened the email by Prof. Deckert, my life has been closely linked to this place and Raman spectroscopy. I sincerely thank all people who helped me during these years.

First of all, I would like to express my sincere thanks to Prof. Dr. Volker Deckert, who gave me the opportunity to learn about such a fascinating interdisciplinary field and the wonderful TERS method. Without his patient and extensive supervision of my research, I would not have been able to bring my PhD thesis to what it is now. He invested countless hours in discussions with me and got me to think scientifically and in-depth. He encouraged me to attend various national and international conferences and with his help and these experiences, I laid a solid foundation and quickly grew to a new level in my scientific research.

Sincere thanks also go to my colleagues' time and help at the Institute of Physical Chemistry (IPC), Jena University and at Leibniz Institute of Photonic Technology (IPHT). Many thanks to Dr. Ludovic Roussille who taught me how to use AFM and TERS and gave me valuable assistance. We had many discussions during my project. He has sophisticated skills in AFM and he is the one who directly lead me into this field. I would also like to thank Dr. Marie Richard-Lacroix, who is an excellent researcher in physical chemistry. She helped me a lot with preparing the lipids and explaining the thermal dynamics in my project. At the same time, I would like to thank Dr. Christiane Höppener, who selflessly and magnificently supported me in my research. I will never forget that she postponed her own urgent work and performed many SEM measurements for me. She also gave me plenty of help on the discussion of my experiments. Another important person I would like to thank here is Dr. Tanja Deckert-Gaudig. She gave me a great amount of support with every single thing. She is one of the best researchers in the field of TERS. Every question on TERS was clarified by her in seconds. Besides her scientific advice, she also baked many delicious cookies and cakes that kept me motivated during the many measurements. Speaking of TERS and SERS, I also have to thank Dr. Henrik Schneidewind. He invested a lot of his time to prepare hundreds of SERS substrates and TERS tips of the best quality. Without his efforts, no SERS and TERS experiments could have been realized in my project.

The same thanks go to my colleague Dr. Steffan Trautmann who gave me the first introduction to AFM. His excellent simulation works gave me a new understanding of the principle of enhanced Raman spectroscopy. A big thanks also goes to my colleague Dr. Robert Meyer. He gave me numerous advice on papers, experiments, and life in general. We worked together to complete my first paper here. His confidence and guidance are also important qualities I want to aquire. He has found a well balance between his study and social work (the chairman of DoKDoK conference 2018). Kourosh Razaei has an extensive knowledge on theories and simulations. We had many nice discussions during my research. I also want to thank Erwan Darussalam, Yogendra Yadav, and Sinju Thomas who really bring a breath of fresh air into our group, also they make our group even more international.

In addition, I want to thank my second supervisor Prof. Dr. Hube Bernhard, who helped me a lot with the research in microbiology. My research partners Dr. Selene Mogavero and Ms. Annika Koenig helped me with the biological parts in my research. They cultured dozens of cell samples for this work. As an interdisciplinary project, my thesis required collaboration with researchers from different disciplines. We are from different institutes and work in different fields. Nevertheless, we actually performed a chemical reaction in this project. I am deeply aware that good collaboration between different disciplines can be the icing on the cake for a work.

Furthermore, I want to give my thanks to those researchers who helped me with my experiments in different areas — Dr. Axel Buchholz and Prof. Dr. Winfried Plass for ESR measurements, Dr. Zian Tang and Prof. Dr. Andrey Turchanin for XPS measurements, Dr. Marco Diegel and Dr. Jan Dellith for XRD measurements and Dr. Stephanie Höppener for TEM measurements.

Finally, I would like to thank my daughter, my wife, and my family. Without their understanding, I would not have had the chance to open the door to the amazing nano world.

There are also many other people and friends who encouraged me at different moments during my research and my life.

Thank you very much!

Publications and Conference Presentations

PUBLICATIONS

1. Robert Meyer, **Xiaobin Yao,** and Volker Deckert. Latest instrumental developments and bioanalytical applications in tip-enhanced Raman spectroscopy. *Trends in Analytical Chemistry*, **2018,** 102:250-258

PRESENTATIONS (Talks)

1. **Xiaobin Yao**, Marie Richard-Lacroix, and Volker Deckert. Investigation of lipid membrane alterations mediated by Candidalysin using time-lapse AFM. **9th AFM BioMed Conference**, 2019, Münster, Germany (Talk)
2. **Xiaobin Yao**. The investigation of the behavior of Candidalysin on lipid membrane using tip-enhanced Raman spectroscopy and atomic force microscopy. **7th DoKDoK**, 2018, Friedrichroda, Germany (Talk)
3. **Xiaobin Yao**, Selene Mogavero, Hube Bernhard, Volker Deckert, et al. The effect of Candidalysin on lipid membranes investigated by tip-enhanced Raman scattering and atomic force microscopy. **Life meets light**, 2018, Jena, Germany (Talk)
4. **Xiaobin Yao**, Ludovic Roussille, Marie Richard-Lacroix, and Volker Deckert. Investigation of the interaction between a pathogen peptide and lipid membranes. **Dornburg Seminar**, 2018, Dornburg, Germany (Talk)

PRESENTATIONS (Posters)

1. **Xiaobin Yao**, Marie Richard-Lacroix, Volker Deckert, et al. Dynamics of lipid membrane alterations mediated by Candidalysin. **Dornburg Seminar**, 2019, Dornburg, Germany (poster)
2. **Xiaobin Yao**, Ludovic Roussille, Volker Deckert, *et al*. The effect of Candidalysin on lipid membranes investigated by tip-enhanced Raman spectroscopy and atomic force microscopy. **26th International Conference of Raman Spectroscopy (ICORS)**, 2018, Jeju, South Korea (Poster)
3. **Xiaobin Yao,** Tanja Deckert Gaudig, and Volker Deckert. Single base distinction of nucleic acids using tip-enhanced Raman scattering. **DNA Nanotechnology**, 2018, Jena, Germany (Poster)
4. **Xiaobin Yao,** Tanja Deckert-Gaudig, Ludovic Roussille and Volker Deckert.

Beyond optical diffraction limitation: Tip-enhanced Raman spectroscopy. **30th Annual conference of Chinese-German Chemical Association (CGCA)**, 2018, Berlin, Germany (Poster)

5. **Xiaobin Yao**, Ludovic Roussille, Annika König, Selene Mogavero, Bernhard Hube, and Volker Deckert. Detection of Candidalysin using tip enhanced Raman spectroscopy. **Life meets light**, 2017, Jena, Germany (Poster)
6. **Xiaobin Yao,** Ludovic Roussile, et al. Detection of Candidalysin on artificial membranes using AFM and TERS. **6th DoKDoK,** 2017, Suhl, Germany (Poster)

Selbständigkeitserklärung

Ich erkläre, dass ich die vorliegende Arbeit selbständig und unter Verwendung der angegebenen Hilfsmittel, persönlichen Mitteilungen und Quellen angefertigt habe.

_____ _____

Ort, Datum Unterschrift der Verfasserin/des Verfassers